Article

Immune responses in checkpoint myocarditis across heart, blood and tumour

https://doi.org/10.1038/s41586-024-08105-5

Received: 20 April 2023

Accepted: 24 September 2024

Published online: 6 November 2024

Check for updates

Steven M. Blum[1,2,3,4,5,17], Daniel A. Zlotoff[1,3,4,5,6,17], Neal P. Smith[1,3,5,17], Isabela J. Kernin[1,3,5,17], Swetha Ramesh[1,3,5,17], Leyre Zubiri[1,2,3,5], Joshua Caplin[6], Nandini Samanta[1,3,5], Sidney Martin[1,3,5], Mike Wang[2], Alice Tirard[1,3,5], Yuhui Song[5], Katherine H. Xu[5], Jaimie Barth[7], Pritha Sen[1,3,4,5,8,9,10], Kamil Slowikowski[1,3,4,5], Jessica Tantivit[1,3,5], Kasidet Manakongtreecheep[1,3,5], Benjamin Y. Arnold[1,3,5], Mazen Nasrallah[1,3,4,5,11], Christopher J. Pinto[2,12], Daniel McLoughlin[2,12], Monica Jackson[2,12], PuiYee Chan[2,12], Aleigha Lawless[5,13], William A. Michaud[5,13], Tatyana Sharova[5,13], Linda T. Nieman[4,5], Justin F. Gainor[2,4], Catherine J. Wu[3,4,8,10], Dejan Juric[2,3,4], Mari Mino-Kenudson[4,7], Giacomo Oliveira[3,4,8], Ryan J. Sullivan[2,4], Genevieve M. Boland[3,4,5,13], James R. Stone[4,7], Molly F. Thomas[1,3,4,5,14,15,16,18], Tomas G. Neilan[4,6,18], Kerry L. Reynolds[2,4,18] & Alexandra-Chloé Villani[1,3,4,5,18] ✉

Immune checkpoint inhibitors are widely used anticancer therapies[1] that can cause morbid and potentially fatal immune-related adverse events such as immune-related myocarditis (irMyocarditis)[2–5]. The pathogenesis of irMyocarditis and its relationship to antitumour immunity remain poorly understood. Here we sought to define immune responses in heart, tumour and blood in patients with irMyocarditis by leveraging single-cell RNA sequencing coupled with T cell receptor (TCR) sequencing, microscopy and proteomics analyses of samples from 28 patients with irMyocarditis and 41 unaffected individuals. Analyses of 84,576 cardiac cells by single-cell RNA sequencing combined with multiplexed microscopy demonstrated increased frequencies and co-localization of cytotoxic T cells, conventional dendritic cells and inflammatory fibroblasts in irMyocarditis heart tissue. Analyses of 366,066 blood cells revealed decreased frequencies of plasmacytoid dendritic cells, conventional dendritic cells and B lineage cells but an increased frequency of other mononuclear phagocytes in irMyocarditis. Fifty-two heart-expanded TCR clones from eight patients did not recognize the putative cardiac autoantigens α-myosin, troponin I or troponin T. Additionally, TCRs enriched in heart tissue were largely nonoverlapping with those enriched in paired tumour tissue. The presence of heart-expanded TCRs in a cycling blood CD8 T cell population was associated with fatal irMyocarditis case status. Collectively, these findings highlight crucial biology driving irMyocarditis and identify putative biomarkers.

Immune checkpoint inhibitors (ICIs) improve cancer outcomes for a wide range of tumour types[1] but can cause potentially dangerous immune-related adverse events (irAEs)[2]. irMyocarditis occurs in 0.3–1.7% of ICI recipients[3–6] and carries a mortality rate of 20–50%, the highest of any irAE and approximately 10-fold higher than myocarditis from other causes[7–9].

The molecular underpinnings of irMyocarditis remain poorly understood. However, irMyocarditis is characterized by an infiltration of both $CD4^+$ and $CD8^+$ T cells and inflammatory macrophages[4,5,10–13]. The finding of shared T cell clones from paired myocardium and tumour of a patient with irMyocarditis indicated the possibility of a common antigen that drives T cell responses in these tissues[10]. Bulk RNA sequencing analysis of irMyocarditis heart tissue demonstrated upregulation of many interferon-stimulated genes (ISGs)[14], which implicates a potential pathway that contributes to pathogenesis. Furthermore, increased circulating $CD8^+$ T cell populations expressing high levels

[1]Center for Immunology and Inflammatory Diseases, Department of Medicine, Massachusetts General Hospital, Boston, MA, USA. [2]Mass General Cancer Center, Boston, MA, USA. [3]Broad Institute of Massachusetts Institute of Technology and Harvard, Cambridge, MA, USA. [4]Harvard Medical School, Boston, MA, USA. [5]Krantz Family Center for Cancer Research, Department of Medicine, Massachusetts General Hospital, Boston, MA, USA. [6]Cardio-Oncology Program, Division of Cardiology, Department of Medicine, Massachusetts General Hospital, Boston, MA, USA. [7]Department of Pathology, Massachusetts General Hospital, Boston, MA, USA. [8]Department of Medical Oncology, Dana-Farber Cancer Institute, Boston, MA, USA. [9]Transplant, Oncology and Immunocompromised Host Program, Division of Infectious Diseases, Brigham and Women's Hospital, Boston, MA, USA. [10]Department of Medicine, Brigham and Women's Hospital, Boston, MA, USA. [11]Division of Rheumatology, North Shore Physicians Group, Department of Medicine, Mass General Brigham Healthcare Center, Lynn, MA, USA. [12]Clinical Research Center, Massachusetts General Hospital, Boston, MA, USA. [13]Department of Surgery, Massachusetts General Hospital, Boston, MA, USA. [14]Division of Gastroenterology, Department of Medicine, Massachusetts General Hospital, Boston, MA, USA. [15]Present address: Division of Gastroenterology, Department of Medicine, Oregon Health and Sciences University, Portland, OR, USA. [16]Present address: Department of Cell, Developmental, and Cancer Biology, Oregon Health and Sciences University, Portland, OR, USA. [17]These authors contributed equally: Steven M. Blum, Daniel A. Zlotoff, Neal P. Smith, Isabela J. Kernin, Swetha Ramesh. [18]These authors jointly supervised this work: Molly F. Thomas, Tomas G. Neilan, Kerry L. Reynolds, Alexandra-Chloé Villani. ✉e-mail: avillani@mgh.harvard.edu

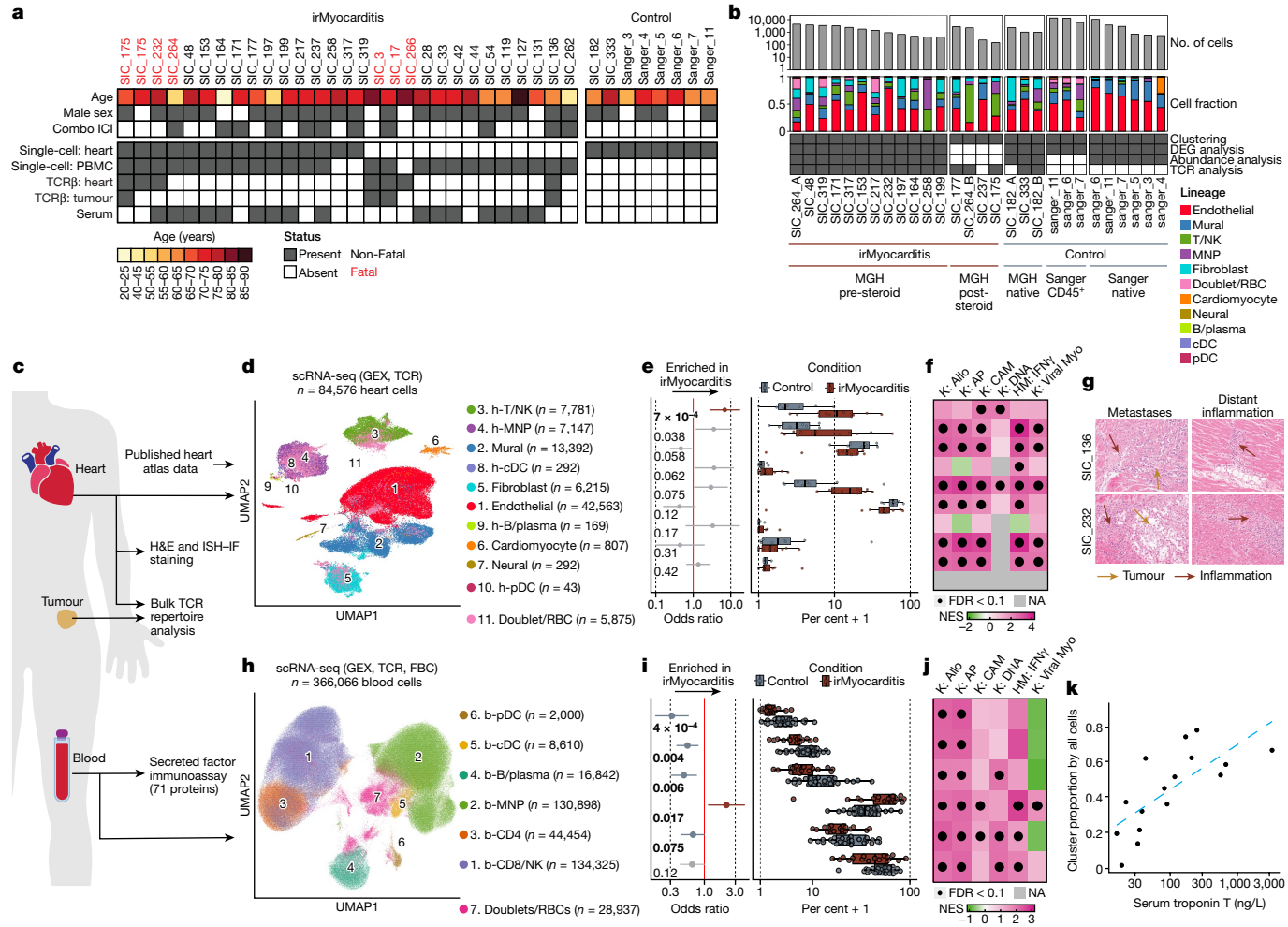

Fig. 1 | Enrichment of multiple intracardiac and blood cell populations in irMyocarditis. a, Summary of the patient samples. Control blood and serum are not shown (Supplementary Table 1). **b**, Top, bar plots indicate the number of cells from each heart sample. Middle, cell lineage composition from each sample. Bottom, sample contribution to different analyses. A and B at the end of patient sample numbers distinguish samples from donors with two myocardial samples. **c**, Summary of sample utilization. **d**,**h**, Uniform manifold approximation and projection (UMAP) embedding displaying indicated cell populations from heart tissue (**d**) and PBMC (**h**) scRNA-seq datasets. **e**,**i**, Abundance analysis comparing intramyocardial cell population frequencies from pre-steroid irMyocarditis heart samples ($n = 12$) versus control samples ($n = 8$) (**e**), and pre-steroid irMyocarditis PBMC samples ($n = 17$) versus ICI-treated control samples ($n = 28$) (**i**). Left, dots represent logistic regression odds ratios. Error bars represent 95% confidence intervals. Unadjusted P values are shown (likelihood ratio test). Bold font and coloured bars indicate FDR < 0.1. Right, box plots show the median (line) and interquartile range (IQR), with whiskers no more than 1.5× the IQR. Each dot represents one patient. **f**,**j**, Select GSEA results for cardiac cell (**f**) and PBMC (**j**) populations, colour-coded by normalized enrichment score (NES) of the gene set in irMyocarditis cases versus control samples. **g**, H&E-stained images (×200 magnification) of cardiac tissues obtained from two patients at autopsy showing intracardiac metastases (left) and inflammation remote from metastatic foci (right). **k**, Circulating frequency of MNPs (y axis) versus serum troponin T (x axis) from pre-steroid irMyocarditis PBMC samples ($n = 16$). $P = 0.002$, FDR < 0.1, linear regression. Allo, allograft rejection; AP, antigen presentation; CAM, cell adhesion molecule; DNA, DNA synthesis; FBC, feature bar code; GEX, gene expression; HM, Hallmark; IFNγ, IFNγ signalling; K, Kyoto Encyclopedia of Genes and Genomes; NA, not applicable; RBC, red blood cell; Viral Myo, viral myocarditis.

of cytotoxic genes and inflammatory chemokines have been associated with irMyocarditis[15]. Studies using *Pdcd1*$^{-/-}$*Ctla4*$^{+/-}$ mice, a genetic model of irMyocarditis, demonstrated that CD8$^+$ T cells are necessary to induce myocarditis, and a fraction of these T cells recognize the cardiac protein α-myosin[16,17]. T cell clones specific for α-myosin occur in the blood of healthy individuals and the blood and hearts of patients with irMyocarditis[16], but their contribution to clinical pathogenesis remains undefined. In this study, we used heart, blood and tumour samples from patients with irMyocarditis to investigate the cellular and transcriptional mediators that underlie irMyocarditis pathogenesis.

Study design and sample collection

Heart, blood and tumour specimens were collected from patients with cancer and irMyocarditis at Massachusetts General Hospital and from ICI-treated individuals without irMyocarditis (Fig. 1a–c, Supplementary Table 1 and Methods). Heart tissue for single-cell RNA sequencing (scRNA-seq) was collected during endomyocardial biopsy procedures on patients with suspected irMyocarditis ($n = 15$: 13 irMyocarditis, 2 unaffected) or during early post-mortem autopsies ($n = 4$: 3 irMyocarditis, 1 unaffected) (Fig. 1a,b and Supplementary Tables 1 and 2). Twelve irMyocarditis samples were collected before the initiation of corticosteroid treatment (pre-steroid). Patients with irMyocarditis in the scRNA-seq group had a median age of 72 years, were 80% male and represented 8 primary tumour types. All had received a PD-1 or PD-L1 inhibitor, of which 7 (47%) were treated with dual PD-1 and CTLA4 inhibitors. Matched heart, tumour and tumour-adjacent normal tissues were collected when possible from irMyocarditis autopsy cases ($n = 7$) and from ICI-treated non-irMyocarditis autopsy cases ($n = 3$) for immunohistochemistry, multiplexed microscopy and bulk T cell

receptor (TCR) β-chain sequencing (TCRβ-seq) experiments (Fig. 1a,c and Supplementary Table 1).

Peripheral blood mononuclear cells (PBMCs) were collected from 30 ICI-treated patients with cancer without irAEs (control group) and 25 patients with irMyocarditis (13 with paired heart scRNA-seq data) (Fig. 1a,c and Supplementary Tables 1, 3 and 4). Control samples and irMyocarditis samples were collected at similar times after ICI initiation (control, median of 56 days, range of 14–497 days; irMyocarditis, median of 62 days, range of 17–252 days). For the irMyocarditis group, data were generated from 55 PBMC specimens across the following time points: before ICI treatment (pre-ICI; $n = 7$); after ICI initiation but before irMyocarditis onset (on-ICI; $n = 4$); before corticosteroid treatment (pre-steroid; $n = 17$); and after corticosteroid treatment and in some cases other immunosuppressive medications (post-steroid; $n = 27$). Pre-steroid serum was available for 16 irMyocarditis cases and 10 non-irMyocarditis cases (Supplementary Table 1).

Heart cell populations and gene programs

scRNA-seq analysis of the heart samples produced transcriptomes from 33,145 single cells. These data were combined with publicly available control heart scRNA-seq data from donors without cancer and not receiving ICI therapy[18] ($n = 6$; 51,431 cells) (Fig. 1c) to create an integrated heart dataset of 84,576 single cells. Throughout the text, immune cell subsets found in heart tissue and blood are denoted by subset names that begin with h- for heart and b- for blood. Subsets are named according to their lineage and distinguishing marker genes. Low-resolution clustering of this heart data produced ten cell lineages: T and natural killer (NK) cells (h-T/NK); conventional dendritic cells (h-cDCs); plasmacytoid dendritic cells (h-pDCs); other mononuclear phagocytes (h-MNPs); B cells and plasmablasts (h-B/plasma); endothelial cells; mural cells; fibroblasts; cardiomyocytes; and neural cells (Fig. 1d, Extended Data Fig. 1a and Supplementary Tables 5 and 6). Samples from our dataset and the public heart atlas[18] contributed to each lineage (Extended Data Fig. 1b). The cellular composition of the heart was broadly consistent across different tumour histologies (Extended Data Fig. 1c).

Cell subset abundance and gene expression analyses compared pre-steroid irMyocarditis heart samples ($n = 12$) to a control group comprising samples from ICI-treated donors without irMyocarditis ($n = 2$) and heart atlas samples ($n = 6$)[18] (Fig. 1b). h-T/NK cells were significantly enriched in irMyocarditis samples (false discovery rate (FDR) = 0.007) (Fig. 1e and Supplementary Table 7), and trends towards increased h-MNPs, h-cDCs and fibroblasts were observed. Gene set enrichment analysis (GSEA) performed at the cell lineage level showed significant upregulation (FDR < 0.1) of programs associated with DNA replication and cell adhesion in both the h-T/NK and fibroblast populations (Fig. 1f and Supplementary Table 8). Gene sets associated with antigen processing, allograft rejection, cell adhesion, viral myocarditis and interferon responses were upregulated in multiple non-immune cell subsets and h-MNPs. These results implicate both immune and non-immune cells in the pathophysiology of irMyocarditis.

Intracardiac metastases in irMyocarditis

Two patients with irMyocarditis and one patient without irMyocarditis (SIC_182; melanoma) had evidence of viable tumour in the myocardium at autopsy. Inflammation was seen both associated with and remote from tumour deposits in both irMyocarditis cases by haematoxylin and eosin (H&E) staining. In detail, SIC_136 (melanoma) had a solitary cardiac lesion, whereas SIC_232 (renal cell carcinoma) had diffuse tumour deposits (Fig. 1g). A third patient with irMyocarditis (SIC_171; melanoma) had received previous targeted (non-ICI) therapy and had evidence of melanin-laden cardiac macrophages following endomyocardial biopsy, which indicated previous intracardiac melanoma (data not shown). Notably, viable tumour cells were not detected in the scRNA-seq data. To assess whether samples with intracardiac metastases affected our findings, we repeated the cell population abundance and gene expression analyses after excluding the scRNA-seq data from patients with evidence of cardiac metastases (patients SIC_171, SIC_232 and SIC_182). The results were highly concordant with those of the full cohort (Extended Data Fig. 1d,e and Supplementary Tables 7, 9 and 10).

Circulating protein analysis

To assess changes in circulating proteins in irMyocarditis, we compared serum concentrations of 71 proteins in pre-steroid irMyocarditis samples ($n = 16$) and in ICI-treated control samples ($n = 10$). Levels of the T cell-activating proteins IL-12p40 (FDR = 0.076), IL-15 (FDR = 0.076) and IL-27 (FDR = 0.076) were increased, as was CXCL13 (FDR = 0.076), which has been associated with irAEs and antitumour responses after ICI therapy[19,20] (Extended Data Fig 1f,g and Supplementary Table 11). Trends towards increased CXCL9, CXCL10, IFNγ, IL-2, IL-18 and TNF levels were observed. Exclusion of a donor with evidence of previous cardiac metastases (SIC_171) did not substantially affect the results when comparing irMyocarditis and control samples (Extended Data Fig. 1h and Supplementary Table 11).

Blood cell populations and gene programs

Cellular indexing of transcriptomes and epitopes sequencing (CITE-seq) was combined with TCR-seq to profile PBMCs from patients with irMyocarditis ($n = 25$) and ICI-treated patients without irMyocarditis ($n = 30$) (Supplementary Tables 1 and 12). Overall, 366,066 cells passed quality control filters, and unsupervised clustering using only transcriptional data identified all expected blood immune cell lineages (Fig. 1h, Extended Data Fig. 1i and Supplementary Tables 6 and 13). To assess the impact of corticosteroid treatment on cell populations, pre-steroid samples ($n = 17$) were compared with post-steroid samples ($n = 19$). B-pDCs (FDR = 1×10^{-4}), *FCGR3A*^{hi}*CDKN1C*^{hi} b-MNPs (FDR = 0.002) and *CD1C*^{hi}*CLEC10A*^{hi} b-DC2s (FDR = 0.018) were less abundant in post-steroid samples (Extended Data Fig. 1j and Supplementary Table 7). Differential gene expression (DGE) analyses and GSEA across blood cell lineages demonstrated marked transcriptional changes, with 4,613 significantly differentially expressed genes (DEGs) and increased immune cell activation in pre-steroid samples (Extended Data Fig. 1k,l and Supplementary Tables 8 and 9). Fewer genes (312 significant DEGs across all lineages) and distinct gene sets correlated with time on steroids (Extended Data Fig. 1m–o). For example, MNP expression of gene sets associated with adipogenesis, cholesterol homeostasis and glycolysis were inversely associated with time on steroids, suggesting that steroids alter MNP metabolism[21] (Supplementary Table 8). Collectively, these data support the use of solely pre-steroid samples to define cell subset abundance and gene expression changes associated with irMyocarditis onset.

Demultiplexing pooled PBMC scRNA-seq data enabled the use of 28 out of 30 control samples for comparisons with pre-steroid irMyocarditis PBMC samples ($n = 17$). b-pDCs (FDR = 0.002), b-cDCs (FDR = 0.012), b-B/plasma cells (FDR = 0.012) and b-CD4 T cells (FDR = 0.090) were all less frequent in irMyocarditis, whereas b-MNPs were more frequent (FDR = 0.026) (Fig. 1i and Supplementary Table 7). Across blood lineages, GSEA showed enrichment of gene sets associated with interferon responses, allograft rejection, antigen presentation, cell adhesion and viral myocarditis in irMyocarditis samples, a result broadly mirroring the heart tissue findings (Fig. 1f,j and Supplementary Table 8). b-MNP frequency in blood correlated directly with serum troponin T (FDR = 0.008), a widely used clinical biomarker of myocardial injury that is associated with poor outcomes in irMyocarditis[22] (Fig. 1k and Supplementary Table 14).

Subclustering of b-CD8 T/NK cell (n = 12 subsets; 135,712 cells), b-CD4 T cell (n = 7; 45,022 cells), myeloid cell (comprising b-MNPs, b-cDCs and b-pDCs; n = 12; 149,101 cells) and b-B/plasma (n = 6; 21,171 cells) lineages were performed to investigate abundance changes of each subpopulation in irMyocarditis samples relative to control samples (Extended Data Fig. 2a–l). No B cell or T cell subsets were more abundant in irMyocarditis, but significant decreases were observed in the circulating frequency of five b-CD8 T/NK cell subsets, three b-CD4 T cell subsets and five b-B/plasma cell subsets (Extended Data Fig. 2c,f,i,l and Supplementary Table 7). The frequency of two b-MNP subsets were increased in irMyocarditis: cluster 5 (*FCGR3A*^{hi}*C1QB*^{hi} b-MNPs; FDR = 0.082) and cluster 7 (*CD14*^{hi}*IFI44L*^{hi} b-MNPs; FDR = 0.047). Marked changes were noted in the b-cDC populations, whereby cluster 8 (*CD14*^{hi}*CLEC10A*^{hi} b-DC3s) was more abundant (FDR = 0.014). By contrast, cluster 11 (*CLEC9A*^{hi}*IDO1*^{hi} b-DC1s; FDR = 4.0×10^{-5}) and cluster 6 (*CD1C*^{hi}*CLEC10A*^{hi} b-DC2s; FDR = 2.6×10^{-4}) were less abundant. None of these cell subsets had a circulating frequency associated with troponin T (Supplementary Table 14).

DGE analysis and GSEA performed on these lineages and subsets showed that T cells, particularly b-CD8 T cell subsets, had increased expression of genes related to antigen recognition and activation (*PDCD1*, *TNFRSF9*, *IFNG* and *TNF*) and decreased expression of transcription factors involved in cell stemness (*TCF7*) and blood recirculation (*KLF2*) (Extended Data Fig. 2m,n and Supplementary Tables 8 and 9). The subsets *CD14*^{hi}*CSF3R*^{hi} b-MNPs and *CD14*^{hi}*DUSP6*^{hi} b-MNPs showed increased expression of *CXCL10*, which has been implicated in irMyocarditis pathogenesis[12], and *IL27*, the protein product of which is increased in the serum of patients with irMyocarditis (Extended Data Fig. 1f,g). GSEA also showed associations with pathways related to interferon responses, allograft rejection, viral myocarditis, cell adhesion and antigen presentation, as well as a broad decrease in TGFβ signalling.

To provide orthogonal validation of our scRNA-seq findings of blood subset abundance, we analysed CITE-seq surface protein data, which is analogous to highly multiplexed flow cytometry[23]. Sequential gates were used to define B cells, CD8 T cells, CD4 T cells, NK cells, pDCs, DC2s and MNPs, and these assignments closely approximated those from the RNA-based clustering (Extended Data Fig. 3a–c). Abundance analyses of pre-steroid irMyocarditis samples (n = 17) and ICI-treated control samples (n = 28) mirrored our scRNA-seq findings. That is, pDCs (FDR = 0.003), CD8 T cells (FDR = 0.030), CD4 T cells (FDR = 0.041), NK cells (FDR = 0.041), cDC2s (FDR = 0.041) and B cells (FDR = 0.041) were all less abundant in blood samples from patients with irMyocarditis, whereas MNPs were more abundant (FDR = 0.003) (Extended Data Fig. 3d and Supplementary Table 15). When CD8 T cell and NK cell populations were combined (CD8 T/NK) to mirror our scRNA-seq-defined lineages, this population was also less abundant in irMyocarditis (FDR = 0.027). Collectively, these results identify new peripheral biomarkers of irMyocarditis onset.

Intracardiac T cell phenotypes

We next subclustered the 9,134 intracardiac h-T/NK cells and defined six distinct subsets: four h-CD8T (clusters 2, 4, 5 and 6), one h-CD4T (cluster 3), and one h-NK cell subset (cluster 1) (Fig. 2a, Extended Data Fig. 4a,b and Supplementary Tables 5 and 6). All h-CD8 T cell subsets broadly expressed markers of cytotoxicity (*GZMK* and *CCL5*) and cell adhesion (*ITGB7*). Cluster 2 (*CD27*^{hi}*LAG3*^{hi} h-CD8 T cells) and cluster 6 (cycling h-CD8 T cells) expressed a range of activation and exhaustion markers (*CTLA4*, *PDCD1* and *TOX*), as well as the chemokine receptor *CXCR3*. Cluster 4 (*CCL5*^{hi}*NKG7*^{hi} h-CD8 T cells) also included a small group of cycling cells with reduced expression of the exhaustion markers *LAG3* and *TOX*. Finally, cluster 5 (*KLRG1*^{hi}*CX3CR1*^{hi} h-CD8 T cells) expressed markers of short-lived effector cells (*KLRG1* and *CX3CR1*)[24]. No clear helper T cell populations could be defined within the h-CD4 T cells using canonical markers (Extended Data Fig. 4c). Therefore, these cells were retained as a single cluster for downstream analyses.

CCL5^{hi}*NKG7*^{hi} h-CD8 T cells (FDR = 0.002) and h-CD4 T cells (FDR = 0.073) were more abundant in irMyocarditis tissue, whereas cycling h-CD8 T cells and *CD27*^{hi}*LAG3*^{hi} h-CD8 T cells displayed trends towards greater abundance (Fig. 2b, Extended Data Fig. 4d,e and Supplementary Table 7). Cycling h-CD8 T cell abundance correlated with serum troponin T (FDR = 0.091), although this association was driven by few donors (Extended Data Fig. 4f and Supplementary Table 14). None of the five other clinical measures of cardiac function or inflammation evaluated were similarly correlated with the abundance of any cell subset enriched in irMyocarditis (Supplementary Table 14).

DGE analysis was conducted for the intracardiac T cell lineage (all T cells) and for each of the defined subsets. Significant upregulation of antigen presentation (*CD74*), immunoreceptor signalling (*LCP2* and *TOX*) and ISGs (*GBP5* and *IFITM1*) were seen across multiple subsets (Extended Data Fig. 4g,h and Supplementary Table 9). Other gene expression changes were cell-subset-specific. That is, cluster 6 (cycling h-CD8 T cells) showed upregulation of multiple immune checkpoints (*CTLA4* and *LAG3*), whereas cluster 2 (*CD27*^{hi}*LAG3*^{hi} h-CD8 T cells) upregulated *ITGA4*, which encodes a therapeutically targetable adhesion molecule[25]. GSEA similarly highlighted enrichment of gene sets involved in cell adhesion, allograft rejection, IFNγ response, TCR signalling and DNA replication at the lineage or subset level. Notably, viral myocarditis gene sets were not upregulated.

To help identify genes associated with irMyocarditis pathogenesis, we performed gene expression modelling by serum troponin T. The gene expression changes most associated with troponin T were within the h-T/NK lineage (Extended Data Fig. 4i and Supplementary Table 9). Positively correlated genes included those associated with cell cycle (*MKI67* and *TOP2A*), antigen presentation (*HLA-DRA* and *HLA-DRB1*) and activation and exhaustion (*LAG3*) (Fig. 2c). Genes inversely correlated with troponin T included the receptors *CX3CR1* and *S1PR5*. GSEA indicated that pathways associated with cell cycle and mTORC1 signalling were positively correlated with serum troponin T, whereas TNF signalling was inversely correlated (Fig. 2d).

T cell clones in heart, tumour and blood

We sought to assess the impact of immunosuppression on the irMyocarditis heart TCR repertoire using a pre-steroid biopsy specimen (SIC_264_A) and a second specimen obtained at autopsy seven days later (SIC_264_B) from the same patient after the administration of methylprednisolone and abatacept (Fig. 1b). The top 13 most expanded TCR clones were found at both time points (Extended Data Fig. 4j,k). Notably, pre-steroid-expanded clones predominantly mapped to CD8 T cells expressing cycling markers (for example, *STMN1*), whereas post-steroid-expanded TCRβ clones mainly mapped to a subset of *CD27*^{hi}*LAG3*^{hi} h-CD8 T cells, which lack markers of cell division (Extended Data Fig. 4a,b). Hence, immunosuppression seemed to alter the transcriptional profile of cardiac T cells but not the predominant TCR clones. Therefore, tissue samples collected both before and after steroid exposure were included in our subsequent TCR analyses.

Next, TCRβ-seq was used to explore the relationship between T cell clones in irMyocarditis heart tissue and paired tumour samples (Fig. 3a). irMyocarditis autopsy cases without diffuse myocardial metastases (n = 6) were classified as active (n = 2; SIC_17 and SIC_264), borderline (n = 1; SIC_136) or healing myocarditis (n = 3; SIC_3, SIC_175 and SIC_266). irMyocarditis tissue samples produced more TCRβ sequences per total nucleated cells than control samples (P = 0.002) (Extended Data Fig. 5a). The two active irMyocarditis cases had the lowest diversity (as measured by Hill's diversity index across all diversity orders), and each had a single TCRβ sequence comprising >40% of their repertoire (Extended Data Fig. 5b–d). Additionally, the TCRβ repertoire was more polyclonal in patients with irMyocarditis and with cardiac metastases

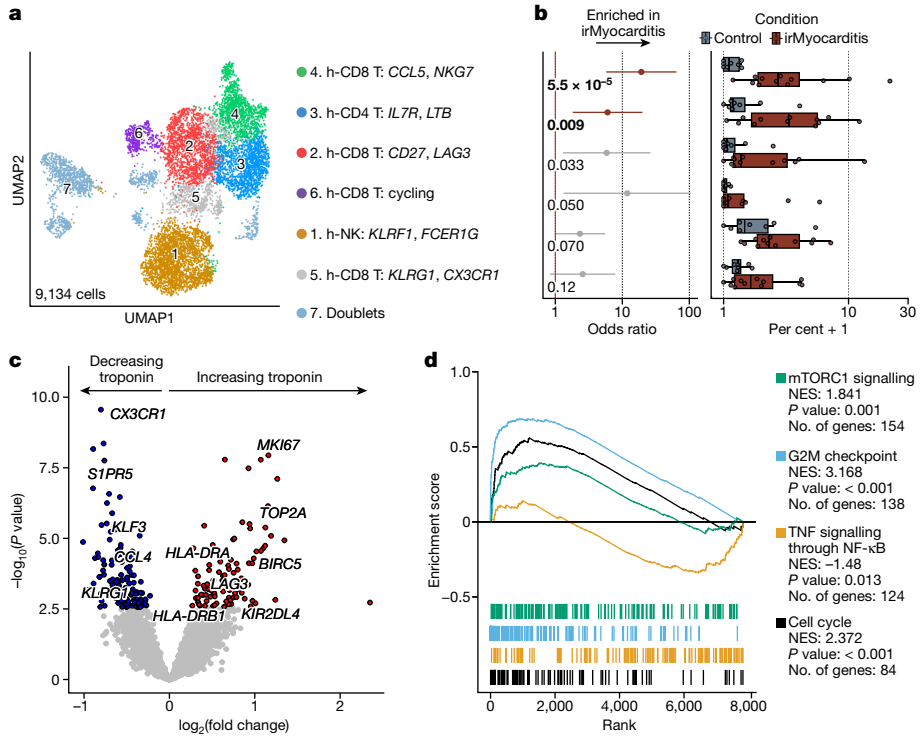

Fig. 2 | Cardiac T cell phenotypes in irMyocarditis. a, UMAP embedding displaying seven subsets produced from 9,134 T/NK cells in the heart tissue scRNA-seq dataset. **b**, Abundance analysis comparing intramyocardial frequencies of cell populations from pre-steroid irMyocarditis heart samples ($n = 12$) versus control samples ($n = 8$). Left, dots represent logistic regression odds ratios. Error bars represent 95% confidence intervals. Unadjusted two-sided *P* values for likelihood ratio test are shown. Bold font and coloured bars indicate FDR < 0.1. Right, box plots show the median (line) and IQR, with whiskers no more than 1.5× the IQR. Each dot represents one patient. **c**, Volcano plot of T/NK lineage genes modelled by serum troponin T. Select genes are highlighted. Coloured points represent FDR < 0.1 (two-sided Wald test). **d**, Select pathways from GSEA of T/NK cell DEGs modelled by serum troponin T (adjusted empirical *P* value).

(SIC_136 and SIC_232) than in patients with active irMyocarditis and no cardiac metastases (Extended Data Fig. 5e).

TCRβ repertoires from irMyocarditis hearts were then compared with those from autologous tumours in patients with available normal control tissue adjacent to tumours ($n = 4$). The inclusion of such control tissue was intended to account for bystander T cells[26] and resident T cell populations in tumour-infiltrated parenchyma[27]. TCRβ clones enriched in heart relative to control tissue were recovered from all patients with irMyocarditis (1–9 clones per donor; $n = 19$ total), whereas clones enriched in tumour tissue relative to control were found in three of these patients (0–17 clones per donor; $n = 28$ total) (Fig. 3b,c, Extended Data Fig. 5f,g and Supplementary Table 16). Across all patients with irMyocarditis, five clones were enriched in both heart and tumour. However, in each patient, the most enriched heart clone was not enriched in tumour. Grouping of lymphocyte interactions by paratope hotspot (GLIPH) analysis showed that most expanded TCRβ clones were not part of any similarity group, but the expanded motifs ($n = 14$) tended to be distinctly enriched in either irMyocarditis or tumour (Extended Data Fig. 5h–j). Although shared epitope specificity among the repertoires of heart and tumour cannot be entirely excluded, these results suggest that enriched TCRβ clones and motifs in each tissue are largely distinct.

We next examined whether TCR clones enriched in irMyocarditis heart tissue can also be detected among circulating CD4 T cells and CD8 T cells. Across all patients, significant TCRβ sequence sharing was found between the heart and five blood CD8 T cell subsets but no CD4 T cell subsets (Extended Data Fig. 6a,b). On a per-patient basis, there was significantly more TCRβ sharing between expanded cardiac T cells and the cycling b-CD8 subset (CD8/NK cluster 10) in fatal compared with non-fatal irMyocarditis (FDR = 0.090) (Fig. 3d, Extended Data Fig. 6c,d and Supplementary Table 17). Cycling b-CD8 cells expressed *CXCR3*, cycling genes (*MKI67* and *STMN1*) and CD45RO surface protein, which indicated that these are antigen-exposed and dividing cells (Fig. 3e). Cycling b-CD8 cells also showed increased expression of *PDCD1*, *TNFRSF9* and *TNF* in irMyocarditis samples compared with control samples (Extended Data Fig. 2n), which suggested that these cells have increased activation and cytotoxicity. By contrast, the *CCL5*^{hi}*GNLY*^{hi} b-CD8 subset (CD8/NK cluster 3) had greater TCRβ sharing between heart and blood in samples from non-fatal irMyocarditis than samples from fatal irMyocarditis (FDR = 0.090). In a fatal irMyocarditis case (SIC_264), heart CD8 T cells sharing TCRβ sequences with blood T cells were found in heart clusters expressing *CXCR3*, which can support cardiac recruitment of T cells[28], but not *CX3CR1* (Extended Data Fig. 6e,f), the expression of which in cardiac T cells was inversely correlated with serum troponin T levels (Fig. 2c). Collectively, these data suggest that sharing of TCRβ between the heart and cycling b-CD8 cells may serve as a biomarker of disease severity.

TCR autoantigen screening

We then investigated whether heart-expanded TCRs are specific for the previously described cardiac autoantigens α-myosin[16], troponin I and troponin T[29–31]. We assayed 52 heart-expanded TCRs identified from eight patients with irMyocarditis. A TCR recognizing a peptide from the α-myosin protein (RINATLETK) served as a positive control[16], and TCRs from unrelated individuals were negative controls (Fig. 3f and Supplementary Table 18). The positive-control TCR recognized RINATLETK as a purified peptide and as part of a peptide pool (α-myosin pool 4), whereas none of the expanded TCRs derived from irMyocarditis donors in our study demonstrated recognition of any of the screened peptides (Fig. 3g and Extended Data Fig. 6g,h). These results suggest

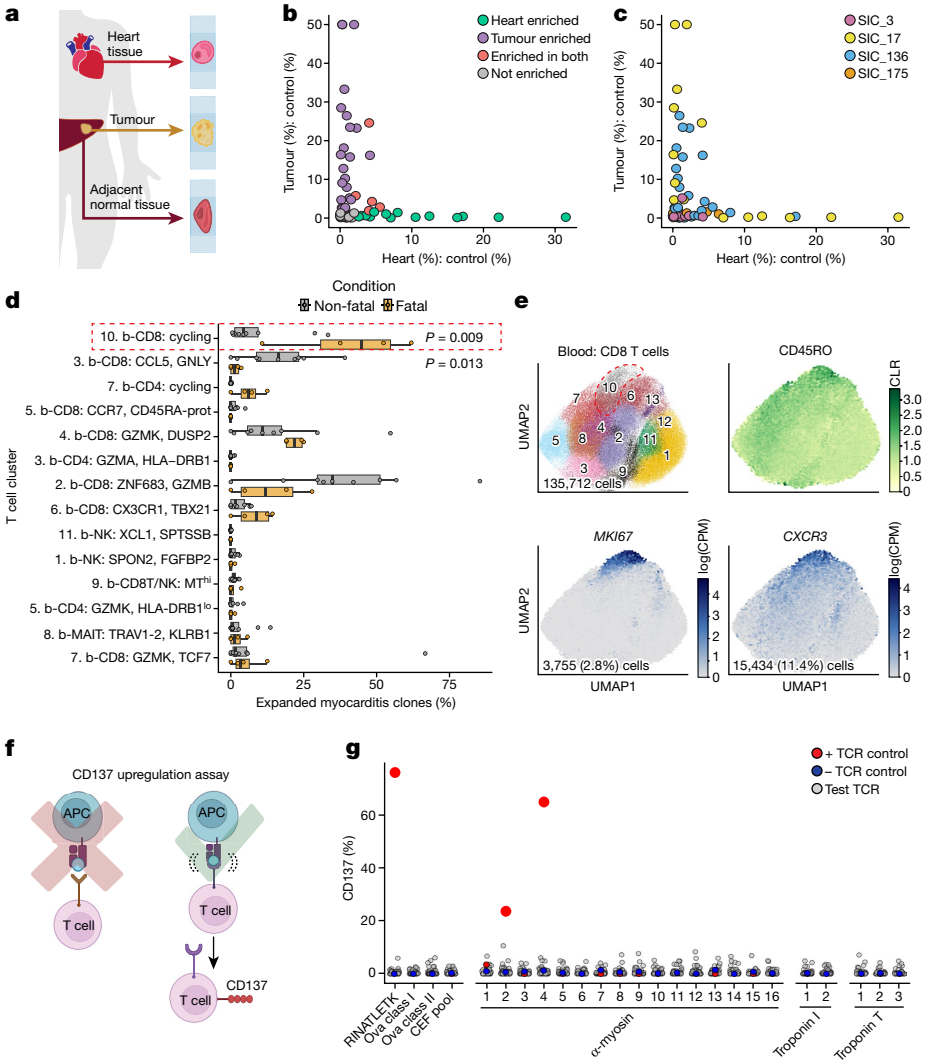

Fig. 3 | TCRs enriched in irMyocarditis are largely distinct from those in tumour, distinguish fatal cases and do not recognize putative cardiac autoantigens. a, Schematic of bulk TCRβ-seq showing macroscopic dissection of paired irMyocarditis, tumour and tumour-adjacent normal parenchyma (control tissue). **b**,**c**, Each TCRβ clone enriched in heart or tumour relative to control samples (FDR < 0.05, two-sided Fisher's exact test) is plotted according to its proportion (among all TCRβ clones in the respective tissue) in heart (*x* axis) and tumour tissue (*y* axis), normalized by its proportion in control tissue. Individual clones are coloured by tissue(s) of enrichment (**b**) and donor (**c**). **d**, The percentage of all TCRβ clones shared between heart and blood cells found within each blood cell subset was calculated on a per-donor basis and stratified by fatal ($n = 4$) and non-fatal ($n = 9$) cases. Box plots display the median (line) and IQR, with whiskers no more than 1.5× the IQR. Each dot represents one patient. The cycling b-CD8 cell subset is highlighted. *P* values from two-sided *t*-tests of subsets meeting a FDR < 0.1 are shown. **e**, UMAP embedding displaying CD8 T/NK cell blood subsets with (top row, left) cycling b-CD8 (cluster 10) circled, and (top row, right and bottom row) feature plots indicating RNA transcript expression (log(CPM)) or protein expression (CLR) across CD8 T/NK cells. **f**, Schematic illustrating the antigen screening assay. **g**, The background-subtracted percentage of TCR-transduced (mTRBC$^+$) T cells expressing CD137 after exposure to the indicated peptide pools (*x* axis). mTRBC$^+$CD8$^+$ or mTRBC$^+$CD8$^-$ results are reported (Extended Data Fig. 6a). Red dots represent a positive-control TCR that recognizes the RINATLETK peptide[16]; blue dots represent control TCRs from unrelated patients; grey dots represent 52 heart-expanded TCRs. APC, antigen presenting cell; CD45RA-prot, CD45RA protein; CEF, cytomegalovirus, Epstein–Barr virus, and influenza virus; MT, mitochondrial transcript; Ova, ovalbumin. Scheme in **f** was created using BioRender (https://biorender.com).

that the most expanded intracardiac T cell clones in our irMyocarditis group do not recognize α-myosin, troponin I or troponin T.

Intracardiac cDCs, pDCs and MNPs

We then subclustered the 9,824 MNP and dendritic cells, which produced five distinct MNP subsets, cDCs and pDCs (Fig. 4a, Extended Data Fig. 7a,b and Supplementary Tables 5 and 6). Cluster 2 (*LYVE1*^{hi} *C1QA*^{hi} h-MNPs) resembled cardiac-resident macrophages[32,33]. Cluster 3 (*FCGR3A*^{hi}*LILRB2*^{hi} h-MNPs) and cluster 4 (*S100A12*^{hi}*VCAN*^{hi} h-MNPs) expressed *FCN1*, which has been associated with monocyte-like signatures[34], and distinguished them from cluster 1 (*S100A8*^{lo}*C1QA*^{lo} h-MNPs). Cluster 5 (*TREM2*^{hi}*APOC1*^{hi} h-MNPs) expressed *GPNMB* and *FABP5*, the latter of which is associated with lipid-rich macrophages[35,36]. There were too few cells in cluster 6 (h-cDCs) to further subcluster these cells into cDC1 (*CLEC9A*) and cDC2 (*CD1C*), and therefore all downstream analyses were performed at h-cDC lineage level. *S100A8*^{lo}*C1QA*^{lo} h-MNPs, *FCGR3A*^{hi}*LILRB2*^{hi} h-MNPs and h-cDCs demonstrated trends towards increased abundance in irMyocarditis tissue (Extended Data Fig. 7c–e and Supplementary Table 7). However, only the frequency of h-cDCs was correlated with serum troponin T (FDR = 0.089) (Fig. 4b and Supplementary Table 14).

We used microscopy to validate the presence of cDCs in irMyocarditis heart tissue and to assess their proximity to CD8 T cells. After

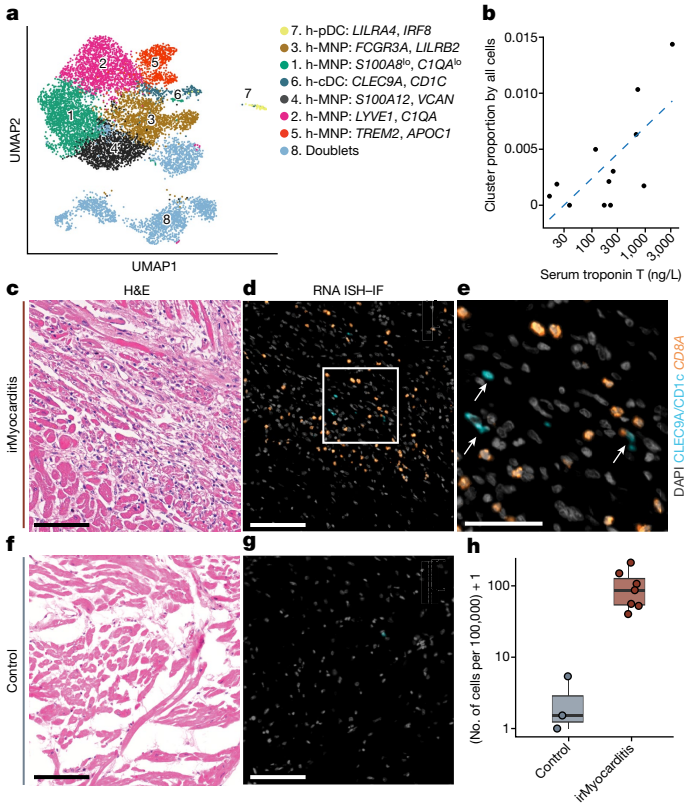

Fig. 4 | cDCs are enriched in irMyocarditis heart tissue and are associated with disease severity. a, UMAP embedding displaying eight subsets produced from the 9,824 MNPs in the heart tissue scRNA-seq dataset. **b**, The intracardiac frequency of h-cDCs (cluster 6; *y* axis) was plotted against serum troponin T levels (*x* axis) for irMyocarditis heart samples ($n = 12$). $P = 0.012$, FDR < 0.1, by linear regression. **c**–**e**, In situ visualization of cDCs (stained with pooled CLEC9A and CD1c antibodies (CLEC9A/CD1c)) in tissue and co-localization with CD8T cells (*CD8A*$^+$) cells. Representative image of irMyocarditis heart tissue stained with H&E (**c**) or by RNA ISH–IF (**d**,**e**). The white box in **d** identifies a field of interest shown at higher magnification in **e**, highlighting cDCs (white arrows). **f**,**g**, Representative section of control heart tissue from an ICI-treated patient stained with H&E (**f**) and by RNA ISH–IF (**g**). **h**, Box plot showing the intracardiac density of cDCs in irMyocarditis hearts ($n = 7$) versus control samples ($n = 3$). $P = 0.008$, FDR < 0.1, one-sided Mann–Whitney *U*-test. Median (line) and IQR are displayed, with whiskers encompassing no more than 1.5× IQR. Each dot represents one patient. Scale bars, 100 µm (**c**,**d**,**f**,**g**) or 50 µm (**e**).

detecting CD1c$^+$ cells by immunohistochemistry (Extended Data Fig. 7f), we performed multiplexed RNA in situ hybridization and immunofluorescence (ISH–IF) on ICI-treated control ($n = 3$) and irMyocarditis ($n = 7$) heart tissue from autopsy samples (Fig. 4c–h). Across whole slides, cDCs were increased in irMyocarditis samples (FDR = 0.033) (Supplementary Table 20). Areas of inflammation in irMyocarditis tissue sections had a 1.7-fold greater density of cDCs (FDR = 0.033) and CD8 T cells (FDR = 0.033) than non-inflamed areas (Extended Data Fig. 7g,h). cDCs were in closer proximity to *CD8A*-expressing cells in irMyocarditis cases (median distance of 748.2 µm) than in control samples (median distance of 4,686 µm) (Extended Data Fig. 7i). Collectively, these data suggest that cDCs are enriched in irMyocarditis hearts, particularly in regions of active inflammation.

Crucial genes and gene sets were upregulated across multiple heart MNP subsets in irMyocarditis (Extended Data Fig. 7j and Supplementary Tables 8 and 9). DEGs included those related to antigen presentation (*HLA-C*, *HLA-DQB2* and *PSMB9*), CXCR3 signalling (*CXCL9* and *CXCL10*; Extended Data Fig. 7k), cytokine signalling (*IL15*, *TNF* and *STAT1*) and ISGs (*GBP5* and *IFITM1*). GSEA indicated activation of transcriptional programs related to antigen processing, cell adhesion, interferon responses, allograft rejection and viral myocarditis.

Stromal cells as inflammatory mediators

We next subclustered the 65,409 non-immune cells, which produced 17 distinct subsets: eight endothelial, three pericyte, one fibroblast, one myofibroblast, one smooth muscle, one endocardial, one neural and one cardiomyocyte population (Extended Data Fig. 8a–e and Supplementary Tables 5 and 6). Three subsets were less abundant in irMyocarditis samples, whereas fibroblasts trended towards enrichment in irMyocarditis (Extended Data Fig. 8c,f,g and Supplementary Table 7). DGE analysis demonstrated marked transcriptional changes, whereby 654 specific genes were upregulated in at least one stromal cell subset (Extended Data Fig. 8h and Supplementary Table 9). Antigen presentation (*CD74* and *HLA-DPB1*), chemokine (*CXCL9*, *CXCL10* and *CXCL11*) and cytokine (*MDK* and *FLT3LG*) transcripts were all increased in several cellular subsets. These results implicate non-immune cells in the orchestration of cardiac immune responses in irMyocarditis[37,38].

Subclustering of the 6,701 cells in the fibroblast lineage produced a myofibroblast subset (cluster 2, expressing *ACTA2* and *ID4*) and five fibroblast subsets (Fig. 5a,b and Supplementary Tables 5 and 6). Two fibroblast subsets were distinguished by the expression of *EGR1*: *DCN*^{hi}*EGR1*^{lo} cluster 1 and *GPC3*^{hi}*EGR1*^{hi} cluster 3. *PCOLCE2*^{hi} *IGFBP6*^{hi} fibroblasts (cluster 4) expressed genes involved in extracellular matrix remodelling[18]. *POSTN*^{hi}*F2R*^{hi} fibroblasts (cluster 5) expressed TGFβ-responsive genes implicated in fibrosis[18,39]. *CXCL9*^{hi}*HLA-DRA*^{hi} fibroblasts (cluster 6) expressed proinflammatory chemokines (*CXCL9*, *CXCL10*, *CXCL11*, *CXCL16*, *CCL5* and *CCL19*), major histocompatibility complex class II machinery (*HLA-DRA*) and ISGs (*GBP4*) (Extended Data Fig. 9a). *DCN*^{hi}*EGR*^{lo} fibroblasts and *CXCL9*^{hi}*HDL-DRA*^{hi} fibroblasts trended towards enrichment in irMyocarditis tissue (Extended Data Fig. 9b and Supplementary Table 7), but only the abundance of *CXCL9*^{hi}*HLA-DRA*^{hi} fibroblasts was positively correlated with serum troponin T (FDR = 0.089) (Fig. 5c and Supplementary Table 14). DEGs associated with irMyocarditis in the fibroblast subsets included those involved in antigen presentation (*HLA-DRA* and *PSMB9*), cytokine signalling (*CXCL9* and *MDK*) and ISGs (*GBP1* and *GBP4*) (Fig. 5d and Supplementary Table 9). GSEA showed similar patterns, but additionally highlighted pathways associated with both dilated and hypertrophic cardiomyopathy (Supplementary Table 8). Genes and GSEA pathways associated with viral myocarditis, interferon responses and cytokine signalling were positively correlated with increasing serum troponin T levels (Fig. 5e, Extended Data Fig. 9c and Supplementary Tables 8 and 9).

ISH–IF validated the presence of cells expressing both fibroblast markers (*COL1A1* and *COL1A2*) and inflammatory cytokines (*CXCL9*, *CXCL10* and *CXCL11*) in proximity of *CD8A*-expressing cells and cDCs (Fig. 5f–l). These inflammatory fibroblasts were observed in irMyocarditis hearts but were absent from ICI-treated control samples (FDR = 0.074) (Fig. 5m and Supplementary Table 20). Notably, these inflammatory fibroblasts were detected only in active cases of irMyocarditis and not in the two cases of healing irMyocarditis (SIC_3 and SIC_175). Although cells similar to *CXCL9*^{hi}*HLA-DRA*^{hi} fibroblasts have not been described in previous human scRNA-seq studies of ischaemic or dilated cardiomyopathy[39], they share features of inflammatory fibroblasts found in active human autoimmune disorders involving other organs and in the context of cellular rejection of murine heart allografts[40,41]. These results indicate a coordinated immune response between immune and stromal cell subsets similar to other cardiac conditions[37,38] but not previously described for irMyocarditis.

Discussion

In this study, we presented an in-depth analysis of paired heart, blood and tumour in patients with irMyocarditis using systems immunology

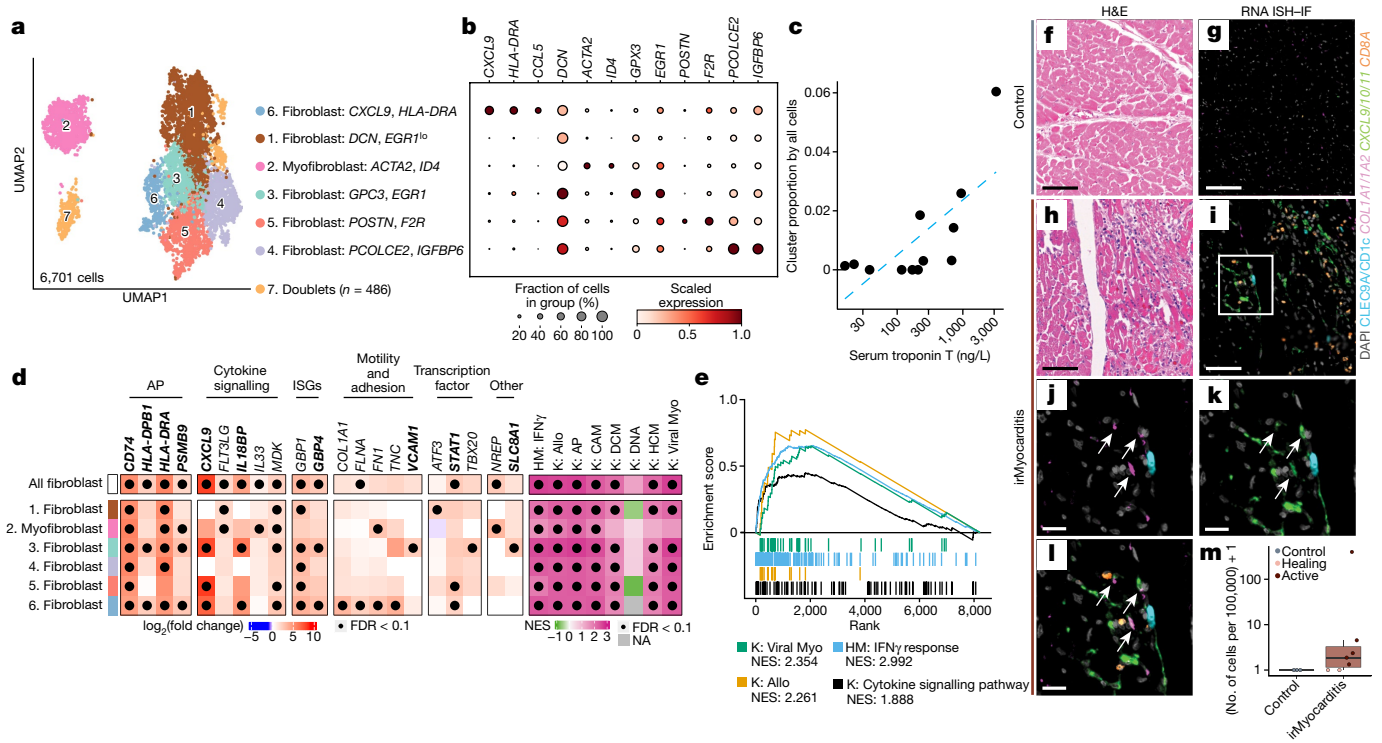

Fig. 5 | Inflammatory fibroblast enrichment in irMyocarditis. a, UMAP embedding displaying seven subsets from 6,701 fibroblasts and myofibroblasts in the heart tissue scRNA-seq dataset. **b**, Top marker genes for each fibroblast subset. Dot size represents the percentage of cells in the subset with non-zero expression of the indicated gene. Colour indicates scaled expression. **c**, Intracardiac frequency of *CXCL9*^{hi}*HLA-DRA*^{hi} fibroblasts (cluster 6; *y* axis) plotted against serum troponin T levels (*x* axis). $n = 12$, $P = 0.008$, FDR < 0.1 (linear regression). **d**, Left, heatmap showing selected DEGs between irMyocarditis and control samples across biological categories. Colour scale indicates $\log_2$(fold change). Black dots indicate FDR < 0.1 (Wald test). Right, select GSEA results, colour-coded by NES of the gene set in irMyocarditis cases. 'All fibroblast' represents a pseudo-bulk analysis of the five fibroblast subsets and exclude myofibroblasts. Bolded genes in the heatmap indicate leading edge genes for displayed GSEA pathways. **e**, Select GSEA pathways modelled by serum troponin T (adjusted empirical *P* value). **f**–**l**, In situ visualization of fibroblasts positive for *CXCL9*, *CXCL10* and *CXCL11* (*CXCL9/10/11*). **f**,**g**, Representative control heart tissue stained with H&E (**f**) or RNA ISH–IF (**g**). **h**–**l**, Representative irMyocarditis heart tissue stained with H&E (**h**) or by RNA ISH–IF (**i**–**l**). White box in **i** is shown at higher magnification in **j** and **l**, highlighting co-staining of DAPI, CLEC9A and CD1c (CLEC9A/CD1c) and *COL1A1* and *COL1A2* (*COL1A1/A2*; **j**); DAPI, CLEC9A/CD1c and *CXCL9/10/11* (**k**); and all stains (**l**). White arrows indicate cells co-staining for *COL1A1/A2* and *CXCL9/10/11*. **m**, Box plot of fibroblasts positive for *CXCL9/10/11* in irMyocarditis heart ($n = 7$) versus control tissue ($n = 3$), where each dot represents one patient. $P = 0.044$, FDR < 0.1, one-sided Mann–Whitney *U*-test. irMyocarditis samples are denoted active or healing. Median (line) and IQR are displayed, with whiskers encompassing no more than 1.5× the IQR. DCM, dilated cardiomyopathy; HCM, hypertrophic cardiomyopathy. Scale bars, 100 µm (**f**–**i**) or 20 µm (**j**–**l**).

approaches. Our key findings, summarized in Extended Data Fig. 9d, revealed new circulating markers of irMyocarditis, including decreased frequencies of blood pDCs, cDCs, B cells and plasma cells, and an increased frequency of blood MNPs. The correlations between serum troponin T levels and intracardiac frequencies of h-cDCs, cycling h-CD8 T cells and *CXCL9*^{hi}*HLA-DRA*^{hi} fibroblasts identify these cells as potentially pathogenic populations. Heart-expanded T cell clones disproportionately shared TCR sequences with circulating cycling b-CD8 T cells in fatal cases and were largely distinct from T cell clones enriched in tumour tissue. Collectively, our results support a pathophysiological model of irMyocarditis in which autoreactive cytotoxic CD8 T cells and antigen presenting cells are both recruited to and retained in the heart by stromal and immune cell signalling networks.

Our findings differ from published results that implicated shared tumour antigens[10] and α-myosin-reactive T cells in irMyocarditis pathology[16]. Interpatient and intertumoural heterogeneity as well as differences in methodology may partially contribute to this discrepancy. Our TCRβ repertoire analyses sought to account for potential bystander TCR clones[26] by normalizing heart and tumour repertoires to those found in normal tissues, which was not previously performed[10]. Additionally, our in vitro antigen screening assay included only the most expanded TCRs and did not fully recapitulate in vivo antigen processing. Thus, although we cannot exclude the possibility that lower abundance heart T cell clones or those that recognize tumour antigens may contribute to irMyocarditis, our findings suggested that the most expanded T cell clones in patients with irMyocarditis are directed against as-yet undetermined antigens and are distinct from those driving anti-tumour immunity. An important unanswered question is whether TCR specificity is deterministic towards irMyocarditis incidence or severity.

Our results help to contextualize irMyocarditis within the emerging literature describing non-cardiac irAEs. irAEs in barrier organs, such as the colon, may be driven by both resident and recruited immune cells[42,43], but irAEs in sterile organs such as the heart and joints are probably mediated by recruited immune cells[44]. Our results demonstrate the presence and enrichment of fibroblasts expressing CXCR3 ligands (*CXCL9*, *CXCL10* and *CXCL11*) in an irAE-affected organ and implicate this signalling axis in the pathogenesis of irMyocarditis[12,45]. These fibroblasts co-localized with cDCs, and although no tertiary lymphoid structures were observed, our data suggest that non-immune cells and cDCs may have a substantial role in irAE pathophysiology. CXCR3 signalling has been implicated in various irAEs[14,42,44,46,47], and disrupting this pathway has demonstrated benefits in models of heart failure, type 1 diabetes and myocarditis[28,48,49], but such disruption may also blunt antitumour responses[50]. Deciphering irAE biology across organ systems may also help explain why certain immunosuppressive agents are helpful in some irAEs but harmful in others[51,52].

Certain analyses were limited by the availability of matched blood, heart and tumour specimens. ICI-treated heart controls lacking any pathology remain challenging to obtain, and our heart scRNA-seq analyses included six patients not exposed to ICIs from a published heart atlas[18]. Although the anatomical locations and tissue processing protocols were similar, technical variation may have contributed to observed changes in cell population abundance and gene expression changes. Additionally, irMyocarditis is often characterized by regions of inflammation interspersed within normal-appearing myocardium[10,11,53,54]. Hence, sampling variation may have contributed to some of the heterogeneity seen across irMyocarditis samples analysed.

Additional research will be needed to identify drivers of irMyocarditis and optimal strategies to diagnose, risk-stratify and therapeutically manage affected patients while preserving antitumour responses. These efforts will ultimately help to maximize oncological benefits of ICIs while minimizing harm from irAEs.

Online content

Any methods, additional references, Nature Portfolio reporting summaries, source data, extended data, supplementary information, acknowledgements, peer review information; details of author contributions and competing interests; and statements of data and code availability are available at https://doi.org/10.1038/s41586-024-08105-5.

1. Haslam, A. & Prasad, V. Estimation of the percentage of US patients with cancer who are eligible for and respond to checkpoint inhibitor immunotherapy drugs. *JAMA Network Open* **2**, e192535 (2019).
2. Martins, F. et al. Adverse effects of immune-checkpoint inhibitors: epidemiology, management and surveillance. *Nat. Rev. Clin. Oncol.* **16**, 563–580 (2019).
3. Mahmood, S. S. et al. Myocarditis in patients treated with immune checkpoint inhibitors. *J. Am. Coll. Cardiol.* **71**, 1755–1764 (2018).
4. Herrmann, J. et al. Defining cardiovascular toxicities of cancer therapies: an International Cardio-Oncology Society (IC-OS) consensus statement. *Eur. Heart J.* **43**, 280–299 (2022).
5. Bonaca, M. P. et al. Myocarditis in the setting of cancer therapeutics: proposed case definitions for emerging clinical syndromes in cardio-oncology. *Circulation* **140**, 80–91 (2019).
6. Tawbi, H. A. et al. Relatlimab and nivolumab versus nivolumab in untreated advanced melanoma. *N. Engl. J. Med.* **386**, 24–34 (2022).
7. Wang, D. Y. et al. Fatal toxic effects associated with immune checkpoint inhibitors: a systematic review and meta-analysis. *JAMA Oncol.* **4**, 1721–1728 (2018).
8. Zhang, L. et al. Cardiotoxicity of immune checkpoint inhibitors. *Curr. Treat. Options Cardiovasc. Med.* **21**, 32 (2019).
9. Salem, J.-E. et al. Cardiovascular toxicities associated with immune checkpoint inhibitors: an observational, retrospective, pharmacovigilance study. *Lancet Oncol.* https://doi.org/10.1016/s1470-2045(18)30608-9 (2018).
10. Johnson, D. B. et al. Fulminant myocarditis with combination immune checkpoint blockade. *N. Engl. J. Med.* **375**, 1749–1755 (2016).
11. Champion, S. N. & Stone, J. R. Immune checkpoint inhibitor associated myocarditis occurs in both high-grade and low-grade forms. *Mod. Pathol.* **33**, 99–108 (2019). *2019 33:1*.
12. Ma, P. et al. Expansion of pathogenic cardiac macrophages in immune checkpoint inhibitor myocarditis. *Circulation* **149**, 48–66 (2024).
13. Siddiqui, B. A. et al. Molecular pathways and cellular subsets associated with adverse clinical outcomes in overlapping immune-related myocarditis and myositis. *Cancer Immunol. Res.* **12**, 964–987 (2024).
14. Finke, D. et al. Comparative transcriptomics of immune checkpoint inhibitor myocarditis identifies guanylate binding protein 5 and 6 dysregulation. *Cancers* **13**, 2498 (2021).
15. Zhu, H. et al. Identification of pathogenic immune cell subsets associated with checkpoint inhibitor-induced myocarditis. *Circulation* **146**, 316–335 (2022).
16. Axelrod, M. L. et al. T cells specific for α-myosin drive immunotherapy-related myocarditis. *Nature* **611**, 818–826 (2022).
17. Wei, S. C. et al. A genetic mouse model recapitulates immune checkpoint inhibitor-associated myocarditis and supports a mechanism-based therapeutic intervention. *Cancer Discov.* **11**, 614–625 (2021).
18. Litviňuková, M. et al. Cells of the adult human heart. *Nature* **588**, 466–472 (2020).
19. Liu, B., Zhang, Y., Wang, D., Hu, X. & Zhang, Z. Single-cell meta-analyses reveal responses of tumor-reactive CXCL13$^+$ T cells to immune-checkpoint blockade. *Nat. Cancer* **3**, 1123–1136 (2022).
20. van Eijs, M. J. M. et al. Toxicity-specific peripheral blood T and B cell dynamics in anti-PD-1 and combined immune checkpoint inhibition. *Cancer Immunol. Immunother.* **72**, 4049–4064 (2023).
21. Auger, J.-P. et al. Metabolic rewiring promotes anti-inflammatory effects of glucocorticoids. *Nature* **629**, 184–192 (2024).
22. Lehmann, L. H. et al. Cardiomuscular biomarkers in the diagnosis and prognostication of immune checkpoint inhibitor myocarditis. *Circulation* **148**, 473–486 (2023).
23. Stoeckius, M. et al. Simultaneous epitope and transcriptome measurement in single cells. *Nat. Methods* **14**, 865–868 (2017).
24. Herndler-Brandstetter, D. et al. KLRG1$^+$ effector CD8$^+$ T cells lose KLRG1, differentiate into all memory T cell lineages, and convey enhanced protective immunity. *Immunity* **48**, 716–729.e8 (2018).
25. Slack, R. J., Macdonald, S. J. F., Roper, J. A., Jenkins, R. G. & Hatley, R. J. D. Emerging therapeutic opportunities for integrin inhibitors. *Nat. Rev. Drug Discov.* **21**, 60–78 (2022).
26. Simoni, Y. et al. Bystander CD8$^+$ T cells are abundant and phenotypically distinct in human tumour infiltrates. *Nature* **557**, 575–579 (2018).
27. Zhang, J. et al. Compartmental analysis of T-cell clonal dynamics as a function of pathologic response to neoadjuvant PD-1 blockade in resectable non-small cell lung cancer. *Clin. Cancer Res.* **26**, 1327–1337 (2020).
28. Ngwenyama, N. et al. CXCR3 regulates CD4$^+$ T cell cardiotropism in pressure overload-induced cardiac dysfunction. *JCI Insight* **4**, e125527 (2019).
29. Lv, H. J. et al. Impaired thymic tolerance to α-myosin directs autoimmunity to the heart in mice and humans. *J. Clin. Invest.* **121**, 1561 (2011).
30. Błyszczuk, P. Myocarditis in humans and in experimental animal models. *Front. Cardiovasc. Med.* **6**, 64 (2019).
31. Kaya, Z., Katus, H. A. & Rose, N. R. Cardiac troponins and autoimmunity: their role in the pathogenesis of myocarditis and of heart failure. *Clin. Immunol.* **134**, 80–88 (2010).
32. Sansonetti, M., Waleczek, F. J. G., Jung, M., Thum, T. & Perbellini, F. Resident cardiac macrophages: crucial modulators of cardiac (patho)physiology. *Basic Res. Cardiol.* https://doi.org/10.1007/s00395-020-00836-6 (2020).
33. Dick, S. A. et al. Self-renewing resident cardiac macrophages limit adverse remodeling following myocardial infarction. *Nat. Immunol.* **20**, 29–39 (2019).
34. Dick, S. A. et al. Three tissue resident macrophage subsets coexist across organs with conserved origins and life cycles. *Sci. Immunol.* **7**, eabf7777 (2022).
35. Umbarawan, Y. et al. FABP5 is a sensitive marker for lipid-rich macrophages in the luminal side of atherosclerotic lesions. *Int. Heart J.* **62**, 666–676 (2021).
36. Lin, L.-Y. et al. Systems genetics approach to biomarker discovery: GPNMB and heart failure in mice and humans. *G3* **8**, 3499–3506 (2018).
37. Xuan, Y., Chen, C., Wen, Z. & Wang, D. W. The roles of cardiac fibroblasts and endothelial cells in myocarditis. *Front. Cardiovasc. Med.* **9**, 882027 (2022).
38. Alex, L. & Frangogiannis, N. G. Pericytes in the infarcted heart. *Vasc. Biol.* **1**, H23–H31 (2019).
39. Chaffin, M. et al. Single-nucleus profiling of human dilated and hypertrophic cardiomyopathy. *Nature* **608**, 174–180 (2022).
40. Korsunsky, I. et al. Cross-tissue, single-cell stromal atlas identifies shared pathological fibroblast phenotypes in four chronic inflammatory diseases. *Med* **3**, 481–518.e14 (2022).
41. Kong, D. et al. The dynamic cellular landscape of grafts with acute rejection after heart transplantation. *J. Heart Lung Transplant.* **42**, 160–172 (2023).
42. Luoma, A. M. et al. Molecular pathways of colon inflammation induced by cancer immunotherapy. *Cell* **182**, 655–671.e22 (2020).
43. Thomas, M. F. et al. Single-cell transcriptomic analyses reveal distinct immune cell contributions to epithelial barrier dysfunction in checkpoint inhibitor colitis. *Nat. Med.* **30**, 1349–1362 (2024).
44. Kim, S. T. et al. Distinct molecular and immune hallmarks of inflammatory arthritis induced by immune checkpoint inhibitors for cancer therapy. *Nat. Commun.* **13**, 1970 (2022).
45. Ji, C. et al. Myocarditis in cynomolgus monkeys following treatment with immune checkpoint inhibitors. *Clin. Cancer Res.* **25**, 4735–4748 (2019).
46. Boughdad, S. et al. Ga-DOTATOC PET/CT to detect immune checkpoint inhibitor-related myocarditis. *J. Immunother. Cancer* **9**, 3594 (2021).
47. Singh, S. et al. Tertiary lymphoid structure signatures are associated with immune checkpoint inhibitor related acute interstitial nephritis. *JCI Insight* https://doi.org/10.1172/jci.insight.165108 (2022).
48. Christen, U. et al. Combination treatment of a novel CXCR3 antagonist ACT-777991 with an anti-CD3 antibody synergistically increases persistent remission in experimental models of type 1 diabetes. *Clin. Exp. Immunol.* **214**, 131–143 (2023).
49. Huang, Y. V. et al. A novel therapeutic approach using CXCR3 blockade to treat immune checkpoint inhibitor-mediated myocarditis. Preprint at *bioRxiv* https://doi.org/10.1101/2024.01.30.576279 (2024).
50. Chow, M. T. et al. Intratumoral activity of the CXCR3 chemokine system is required for the efficacy of anti-PD-1 therapy. *Immunity* **50**, 1498–1512.e5 (2019).
51. Zou, F. et al. Efficacy and safety of vedolizumab and infliximab treatment for immune-mediated diarrhea and colitis in patients with cancer: a two-center observational study. *J. Immunother. Cancer* **9**, e003277 (2021).
52. Cautela, J. et al. Intensified immunosuppressive therapy in patients with immune checkpoint inhibitor-induced myocarditis. *J. Immunother. Cancer* **8**, e001887 (2020).
53. Palaskas, N., Lopez-Mattei, J., Durand, J. B., Iliescu, C. & Deswal, A. Immune checkpoint inhibitor myocarditis: pathophysiological characteristics, diagnosis, and treatment. *J. Am. Heart Assoc.* **9**, e013757 (2020).
54. Zhang, L. et al. Cardiovascular magnetic resonance in immune checkpoint inhibitor-associated myocarditis. *Eur. Heart J.* **41**, 1733–1743 (2020).

Methods

Study design, patient identification and sample selection of heart specimens for scRNA-seq

Heart tissue samples were collected at our institution through endomyocardial biopsy or autopsy of patients receiving ICI agents for the treatment of cancer. Informed consent was obtained from all patients or their appropriate representatives. This consent included consent to publish indirect patient identifiers, such as age, sex and patient-identified race. All research protocols were approved by the Dana-Farber/Harvard Cancer Center Institutional Review Boards (numbers 11-181 and 13-416). No statistical methods were used to predetermine sample size. Endomyocardial biopsy samples were collected in the catheterization laboratory as part of the clinical evaluation for suspected irMyocarditis, and a single tissue fragment (about 1–2 mm^3) primarily derived from the right side of the interventricular septum was collected for research. One patient (SIC_264) had a biopsy of the left ventricle for clinical reasons. Autopsy samples were obtained by an autopsy pathologist from the right ventricular free wall. Autopsy samples were obtained rapidly (within 6 h) following the death of patients receiving ICI agents with or without clinically suspected irMyocarditis. ICI-treated donors were classified as having irMyocarditis based on one of the following criteria: a histopathological diagnosis based on review of cardiac tissue by cardiac pathologists as part of routine clinical care ($n = 24$) or a diagnostic cardiac MRI (based on Lake Louise criteria[55]; $n = 4$). Control heart samples were obtained through two sources: (1) two samples (SIC_182 and SIC_333) were obtained at our institution from patients with cancer who received ICIs and underwent endomyocardial biopsies and/or autopsy with a clinical suspicion for irMyocarditis, but they ultimately did not have histopathological features of irMyocarditis; (2) six additional control samples were obtained from hearts that were offered but not selected for transplantation and were used to generate a scRNA-seq heart atlas, as previously described[18]; none of these patients were known to be on ICI therapy. To account for differences in cell proportions or gene expression that occurs in different regions of the heart[18,56], we only used samples from this control cohort that were obtained from the right ventricle septum or right ventricular free wall to match the anatomical location of samples collected at our institution. The heart atlas also included samples that were enriched for $CD45^+$ cells, which we included in our clustering and selected downstream analyses, as outlined in Fig. 1b.

Study design, patient identification and sample selection of heart and tumour specimens for bulk TCRβ-seq

Samples for bulk TCRβ-seq were identified from the autopsies of cases enrolled in our scRNA-seq cohort as well as additional patients who consented to our tissue banking protocols and were found to have histological evidence of irMyocarditis at the time of autopsy. Control heart tissue samples for bulk TCRβ-seq were identified from patients who were receiving an ICI, did not have evidence of irMyocarditis at autopsy and for whom archival tissue was available through our biobanking protocol. irMyocarditis cases without diffuse myocardial metastases ($n = 6$) were classified by a cardiac pathologist as active myocarditis ($n = 2$; SIC_17 and SIC_264), lymphocytic infiltrate without associated myocyte injury suggestive of irMyocarditis (borderline; $n = 1$; SIC_136, who also had a single macroscopic cardiac metastasis in another tissue block) or healing myocarditis ($n = 3$; SIC_3, SIC_175, and SIC_266) in accordance with the Dallas Criteria[57].

Study design, patient identification and sample selection of blood and serum specimens

Paired blood and serum were sought before the initiation of corticosteroids for the treatment of irMyocarditis in our tissue scRNA-seq cohort as well as additional patients who were diagnosed with irMyocarditis but did not have tissue data. Where available, blood samples were collected or accessed from collaborating biobanking efforts at the following clinically relevant time points: (1) before the start of ICI (pre-ICI time points); after the start of ICI but without clinical irMyocarditis (on-ICI); (2) at the time of clinical irMyocarditis diagnosis but before steroid treatment initiation (pre-steroid); (3) after steroid treatment initiation or subsequent therapies (collectively, post-steroid samples). Control serum samples were identified from biobanked specimens from patients receiving an ICI who presented to Massachusetts General Hospital (MGH) with concern for an irAE but ultimately were found to have alternative causes for their symptoms and did not develop irMyocarditis or any other irAE.

Additional control PBMC samples were identified through the MGH Melanoma Biobank (DFCI/HCC protocol number 11-181). Control samples were from individuals who had received at least two doses of an ICI regimen that contained a PD-1 inhibitor and had at least eight weeks of follow-up before the next therapy or death. Patients were included if they had no documented irAEs on that line of therapy. More than 300 clinical charts were reviewed. Samples collected within the first 100 days after starting therapy were prioritized to match the general timing of irMyocarditis onset, which is typically in the first three months of ICI therapy[53].

Clinical covariates

Clinical data were retrospectively obtained from electronic medical records, including patient demographics, cancer type, previous cancer therapies received, specific ICI agents used, method of irMyocarditis diagnosis, myocardial biopsy pathology grade, troponin T measurements, routine laboratory tests (NT-proBNP, erythrocyte sedimentation, C-reactive protein), echocardiographic parameters (left ventricular ejection fraction), electrocardiogram data (QRS duration) and concomitant irAEs. Peak troponin T was defined as the highest value during the index admission. All clinical metadata are provided in Supplementary Table 1.

Preparation of tissue samples for scRNA-seq

Tissue samples obtained by biopsy or autopsy were immediately placed in ice-cold HypoThermosol solution (BioLife Solutions) and kept on ice during transfer to the research facility. Tissue was then washed twice with cold PBS before being dissociated with a human tumour dissociation kit according to the manufacturer's instructions (Miltenyi Biotic), except that calcium chloride was added to the enzymatic cocktail to a final concentration of 1.25 mM. Biopsy samples were cut into ≤1 mm pieces with standard laboratory tissue dissection scissors. Tubes containing tissue fragments in the enzymatic cocktail were placed in a heated shaker at 37 °C with shaking at 750 r.p.m. for 25 min, with the machine placed on its side to prevent tissue fragments from settling. Following incubation, the reaction was quenched through the addition of 100 µl human serum. The mixture was further dissociated through manual trituration followed by filtration through a 70 µm mesh. Following centrifugation at 350*g* for 12 min, the supernatant was removed, and RBC lysis was performed for 2 min (ACK lysing buffer, Lonza). Following a wash step, cells were resuspended in phenol-free RPMI with 2% (v/v) human AB serum.

Owing to excessive debris, the following myocardial samples obtained from autopsy were sorted by FACS for live (DAPI), non-RBCs (CD235a) following tissue dissociation. These include the following samples: SIC_176, SIC_182_B, SIC_232 and SIC_264_B (B samples refer to the second of two samples when collected from the same patient). Tissue was prepared for cell sorting by first undergoing dissociation as described above. Following the resuspension of cells in sorting buffer (phenol-free RPMI with 2% (v/v) human AB serum), Fc receptors were blocked (Human TruStain FcX, BioLegend 422302), after which cells were incubated with CD235a-PE-Cy5 (BioLegend 306606) for 30 min. Following a wash, cells were resuspended in sorting buffer containing DAPI. Flow cytometric sorting was performed on a Sony MA900 cell

sorter (Cell Sorter software v.3.3.0) to collect live, singlet, CD235a$^-$ cells (Extended Data Fig. 10). Sorted cells were centrifuged and resuspended in sorting buffer before loading in a 10x Chromium chip.

PBMC CD45$^+$ enrichment, cell hashing and CITE-seq staining

Cryopreserved PMBC samples were used for CITE-seq data generation[23] (Supplementary Table 1). Cells were thawed at 37 °C, diluted with a 10× volume of RPMI with 10% heat-inactivated human AB serum (Sigma) and centrifuged at 300*g* for 7 min. Cells were resuspended in CITE-seq buffer (RPMI with 2.5% (v/v) human AB serum and 2 mM EDTA) and added to 96-well plates. Dead cells were removed with an Annexin-V-conjugated bead kit (Stemcell, 17899) and RBCs were removed with a glycophorin-A-based antibody kit (Stemcell, 01738). Modifications were made to the manufacturer's protocols for each to accommodate a sample volume of 150 µl. Cells were quantified with an automated cell counter (Bio-Rad, TC20), after which 2.5×10^5 cells were resuspended in CITE-seq buffer containing TruStain FcX blocker (BioLegend, 422302) and MojoSort CD45 Nanobeads (BioLegend, 480030). For batches for which hashtags were used for demultiplexing, hashtag antibodies (BioLegend) were added to samples followed by 30 min of incubation on ice and then washed 3 times with CITE-seq buffer using a magnet to retain CD45$^+$ cells. For each washing step, 1.4 ml of CITE-seq buffer was added to the sample, cells were resuspended followed by centrifugation at 300*g* for 7 min at 4 °C. Supernatant was then removed before starting the next washing step. For samples for which genetic demultiplexing was used, this hashtag staining step was omitted (Supplementary Tables 3 and 4). Live cells were counted using trypan blue, and 6–8 samples (each sample with 60,000 cells) were pooled together at equal concentrations. Pooled samples were filtered through 40 µm strainers, centrifuged and resuspended in CITE-seq buffer with TotalSeq-C antibody cocktail (BioLegend; Supplementary Table 12). Cells were incubated on ice for 30 min, followed by 3 washes with CITE-seq buffer and a final wash in the same buffer without EDTA (RPMI with 2.5% (v/v) human AB serum). Cells were resuspended in this buffer without EDTA, filtered a second time and counted.

scRNA-seq data generation

For heart samples, single-cell suspensions containing up to 12,000 cells (or all available cells when the total was <12,000) were loaded per channel on 10x Chromium chips. For some samples, two channels on the 10x Chromium chip were loaded to maximize cell recovery; downstream data from these multiple wells were later combined and considered as a single sample. For hashed PBMC samples, samples were diluted to a concentration of 1,200 cells per µl, and 50,000 cells were loaded per channel into a 10x Chromium chip. According to the manufacturer's instructions, cell–bead emulsions were generated and transferred to PCR tube strips, after which cDNA libraries were generated. Libraries from heart samples were generated using Chromium Single Cell 5′ v.1 kits (10x Genomics, PN-1000006), except for one sample (SIC_317), which was generated with a 5′ v.2 kit (10x Genomics, PN-1000263) (Supplementary Table 2). Hashed PBMC single-cell libraries were generated using a Chromium Single Cell 5′ kit (v.1.1, 10x Genomics, PN-1000020) together with the 5′ Feature Barcode library kit (10x Genomics, PN-1000080) (Supplementary Tables 3 and 4). TCR-enriched cDNA libraries were generated using a Chromium Single Cell V(D)J Enrichment kit (10x Genomics, PN-1000005). Library quality was assessed using an Agilent 2100 Bioanalyzer.

All heart sample gene expression libraries were sequenced on an Illumina NextSeq 500/550 instrument using the high output v.2.5 75 cycles kit with the following sequencing parameters: read 1 = 26; read 2 = 56; index 1 = 8; index 2 = 0. TCR-enriched libraries from heart tissue were sequenced on an Illumina NextSeq 500/550 instrument using the high output v.2.5 150 cycle kit with the following sequencing parameters: read 1 = 30, read 2 = 130, index 1 = 8, index 2 = 0. All hashed PBMC CITE-seq, feature barcode (ADT and HTO libraries) and TCR libraries were sequenced on an Illumina Novaseq instrument using S4 300 cycles flow with the following sequencing parameters: read 1 = 26; read 2 = 91; index 1 = 8; index 2 = 0.

scRNA-seq read alignment and quantification

Raw sequencing data were pre-processed using CellRanger (v.3.0.2, 10x Genomics) to demultiplex FASTQ reads, align reads to the human reference genome (GRCh38, v.3.0.0 from 10x Genomics) and count unique molecular identifiers (UMIs) to produce a cell × gene count matrix[58]. All count matrices were then aggregated using Pegasus (v.1.1.0, Python) with the aggregate_matrices function[59]. Low-quality droplets were filtered out of the matrix before proceeding with downstream analyses using the percentage of mitochondrial UMIs and number of unique genes detected as filters (heart tissue = <20% mitochondrial UMIs, >300 unique genes; PBMCs = <15% mitochondrial UMIs, >300 unique genes). The percentage of mitochondrial UMI was computed using 13 mitochondrial genes (*MT-ND6*, *MT-CO2*, *MT-CYB*, *MT-ND2*, *MT-ND5*, *MT-CO1*, *MT-ND3*, *MT-ND4*, *MT-ND1*, *MT-ATP6*, *MT-CO3*, *MT-ND4L* and *MT-ATP8*) using the qc_metrics function in Pegasus. The counts for each remaining cell in the matrix were then log-normalized by computing the log1p(counts per 100,000), which we refer to in the text and figures as log(CPM). Detailed quality control statistics for these datasets are compiled in Supplementary Tables 2 and 4.

Demultiplexing of PBMC data

For the PBMC data from patients who developed irMyocarditis, cells underwent cell hashing with TotalSeq-C hashing antibodies (see the section 'scRNA-seq data generation') and were demultiplexed using DemuxEM[60]. For the PBMC data from our control group of patients who lacked any irAEs, cells were pooled before loading the 10x Chromium instrument, and an aliquot of cells from each donor was lysed in Buffer TCL + 1% β-mercaptoethanol at a concentration of 1,000 cells per µl. Next, 25 µl of lysed cells per sample was used to generate low-input bulk RNA-seq using the SmartSeq2 protocol[61] to enable genetic demultiplexing. Bulk RNA-seq data were sequenced on a NextSeq 550 with the following parameters: read 1 = 38; read 2 = 38; index 1 = 8; index 2 = 8. In brief, VCF files were generated from the bulk RNA-seq data for each donor using CellSNP-lite (v.1.2.3)[62]. Next, the pooled scRNA-seq data were demultiplexed using Souporcell (v.2.5)[63], and the resulting VCF files for each predicted donor were matched to the VCF files from our bulk RNA-seq data using Vireo (v.0.5.8, Python)[64]. All donors from the group were able to be demultiplexed with confidence with the exception of two donors (donor_730 and donor_327) owing to poor recovery of variants from their bulk RNA-seq data. Therefore, these donors were included in our clustering solution but were not included in any donor-driven analyses (that is, DGE and differential abundance).

Basic clustering

All cells from all samples were utilized for clustering. First, 2,000 highly variable genes were selected using the highly_variable_features function in Pegasus and used as input for principal component analysis. To account for technical variability between donors, the resulting principal component scores were aligned using the Harmony algorithm[65]. The resulting principal components were used as input for Leiden clustering and UMAP algorithm (spread = 1, min-dist = 0.5).

The following canonical markers were used to distinguish broadly defined cell lineages: T and NK cells when assessed together (*CD3D* and *KLRB1*); CD8 T and NK cells (*CD3D*, *CD8A* and *KLRF1*) and CD4T cells (*CD3D*, *CD4* and *IL7R*) when assessed separately; cDCs (*HRA-DRA*, *CD1C* and *CLEC9A*); pDCs (*LILRA4* and *IL3RA*); other MNPs (*LYZ*, *CD14* and *CD68*); B/plasmablasts (*CD79A* and *MZB1*); endothelial cells (*VWF* and *CA4*); mural cells (*RGS* and *KCNJ8*); fibroblasts (*DCN* and *PDGFRA*); cardiomyocytes (*TNNI3* and *MB*); and neural cells (*PLP1* and *NRXN1*). The number of principal components used for each blood clustering

(CD4 T = 16; CD8 T/NK = 20; MNP = 24; B cells = 16; all cells = 30) and tissue clustering (T/NK = 24; MNP = 35; non-immune = 50) was decided using molecular cross-validation[66].

Marker gene identification and cell annotation

The marker genes defining each distinct cell subset from our global and lineage-specific subclustering analyses were determined by applying two complementary methods. First, we calculated the area under the receiver operating characteristic (AUROC) curve for the log(CPM) values of each gene as a predictor of cluster membership using the de_analysis function in Pegasus. Genes with an AUROC ≥ 0.75 were considered marker genes for a particular cell subset. Second, we created a pseudobulk count matrix[67] by summing the UMI counts across cells for each unique cluster–sample combination, creating a matrix of n genes × (n samples × n clusters). We performed one-versus-all (OVA) differential expression analyses for each cell subset using the Limma package (v.3.54.0, R)[68]. For each subset, we used the input model gene ~ in_clust, where in_clust is a factor with two levels indicating whether the sample was in or not in the subset being tested. A moderated t-test was used to calculate P values and compute a FDR using the Bejamini–Hochberg method. We identified marker genes that were significantly associated with a particular subset as having a FDR < 0.05 and a $\log_2$(fold change) > 0. The AUROC and OVA pseudobulk marker genes for all cell subsets are provided in Supplementary Tables 5 and 13. Marker genes for each cell subset were interrogated and investigated in the context of other published immune profiles to guide our cell subset annotations.

Abundance analysis

To identify the association between cell subset abundance and either patient group (irMyocarditis versus control) or time point (pre-steroid versus post-steroid), we used a mixed-effects association logistic regression model similar to a previously described method[69]. We used the glmer function from the lme4 package (v.1.1-31, R) to fit a logistic regression model for each cell subset. Each subset was modelled independently with a full model as follows:

$$\text{Cluster} \sim 1 + \text{comparison} + (1|\text{id})$$

where cluster is a binary indicator set to 1 when a cell belongs to the given cell subset or 0 otherwise, comparison is a factor with 2 levels that represented either the patient groups (irMyocarditis or control) or the time points (pre-steroid or post-steroid), and id is a factor indicating the donor. The notation (1|id) indicates that id is a random intercept. To determine significant associations, a null model of cluster ~ 1 + (1|id) was fit and a likelihood ratio test was used to compare the full and null models. A FDR was calculated using the Benjamini–Hochberg approach, and clusters with a FDR < 10% were considered significant.

As we were underpowered to investigate differences between fatal and non-fatal irMyocarditis in our scRNA-seq data, we sought to identify associations between cell subset frequencies and clinically relevant cardiac measurements, including serum troponin T levels, NT-proBNP, left ventricle ejection fraction, erythrocyte sedimentation rate, C-reactive protein and QRS duration. In addition, we aimed to understand how the length of time between corticosteroid initiation and post-corticosteroid sample collection altered cellular abundances.

For associations with clinical metrics, we limited our analysis to include only cell subsets that were differentially abundant in irMyocarditis cases versus control samples (unadjusted P value < 0.1) given we do not expect subsets that are unchanged in the presence of irMyocarditis to correlate with clinical metrics of cardiac injury. Similarly, for the modelling of gene expression by time between corticosteroid initiation and sample collection, we limited our analysis to only include cell subsets that were differentially abundant between pre-steroid and post-corticosteroid samples (unadjusted P value < 0.1). For every metric, we performed linear regression on each cell subset individually, using the model log(abundance + 1) ~ log(variable), where variable is the value of the clinical metric and abundance is the relative proportion of the subset in a given sample. All clinical metrics represented measurements closest to time of tissue sample collection, with cut-off values of no greater than ±2 days for troponin T measurements and no greater than ±7 days for all other measurements. For the analysis of time between corticosteroid initiation and sample collection, variable was the number of days.

To accurately measure the abundance of each cellular component of heart tissue, we used only unenriched samples (native fractions) and excluded the $CD45^+$-enriched samples from the published heart atlas[18]. In the case of SIC_182, control samples from a patient who underwent a biopsy (sample SIC_182_A) and then an autopsy (SIC_182_B) but did not have irMyocarditis and never received immunosuppression therapy, data from this patient's two samples were combined and treated as a single time point.

DGE analysis

Comparisons between irMyocarditis and control heart tissue were limited to samples collected before corticosteroid administration (pre-steroid) and included both native and $CD45^+$-enriched samples from the heart cell atlas to account for the paucity of immune cells in non-inflamed hearts[29] (Fig. 1b). To capture differences in PBMCs associated with irMyocarditis or control samples, we compared pre-steroid PBMC samples from irMyocarditis cases to control samples from patients who were treated with a checkpoint inhibitor but showed no symptoms of any irAEs. To understand the effects of corticosteroids on our PBMC dataset, we compared pre-steroid irMyocarditis samples to samples collected after corticosteroid administration (post-steroid). These DGE analyses (irMyocarditis case versus control, pre-steroid versus post-steroid) were performed on pseudobulk count matrices using the DESeq2 package (v. 1.38.2, R). The input model was gene ~ comparison, where comparison was a binary variable indicating that the sample either came from a patient with irMyocarditis or a patient without irMyocarditis or the time point for the corresponding sample (pre-steroid or post-steroid).

To identify gene expression associations with disease severity, we used DESeq2 with the input model gene ~ log(troponin), where troponin is an individual's serum troponin T level measured closest to the time of tissue sample collection (no greater than ±2 days).

To identify genes associated with the length of time between corticosteroid initiation and post-corticosteroid sample collection, we used DESeq2 with the input model gene ~ log(change in post-steroid troponin) + log(time from steroid start to post-steroid sample collection), where change in post-steroid troponin was the fold change between a donor's peak serum troponin T level and their serum troponin T level at the time of post-steroid sample collection. Time from steroid start to post-steroid sample collect was the number of days between corticosteroid initiation and post-corticosteroid sample collection. This model enabled us to find changes associated with the amount of time on corticosteroids while controlling for potential improvement in irMyocarditis.

Significant DEGs were identified using a Wald test (FDR < 0.1) (Supplementary Table 9). Select DEGs were visualized using ComplexHeatamp (v.2.14.0, R).

GSEA

GSEA was performed using the fgsea function from the fgsea package (v.1.18.0, R) with 10,000 permutations to test for independence. For both comparisons of irMyocarditis cases versus controls and associations with serum troponin T levels, the input gene rankings for each cell subset were based on decreasing Wald statistic values from differential expression analysis for which the gene with the highest Wald statistic (that is, associated with irMyocarditis or associated with

higher troponin) was ranked first and the gene with the lowest Wald statistic (that is, associated with control or associated with lower troponin) was ranked last. The input gene sets tested were derived from the KEGG and Hallmark pathways database and are compiled in Supplementary Table 8.

Secreted factors analysis

Peripheral blood was collected from patients with or without irMyocarditis in serum separator tubes. Following centrifugation for 10 min at 890*g*, serum was collected and stored at −80 °C. Aliquots of undiluted serum were analysed for the presence of 71 secreted factors through multiplex immunoassay (Human Cytokine Array/Chemokine Array 71-Plex panel, HD71, Eve Technologies). log +1-transformed values were compared using a two-sided *t*-test.

CITE-seq analysis

CITE-seq protein feature data were used to validate changes in cell population abundance between irMyocarditis cases ($n = 17$) and control samples ($n = 28$) that were observed using gene expression (GEX) scRNA-seq data. Cells with recovered CITE-seq information were first limited to non-doublet cells present in the blood GEX dataset through barcode matching. Cells were further filtered for those with at least a sum of 100 UMI counts across all CITE-seq features. This dataset was then normalized using a centred log-ratio transformation and gated by protein expression value. Eleven manually curated protein features representing key canonical immune cell lineage markers were used to define the following gating strategies that clearly delineated positive and negative populations: pDCs, $CD3^-CD19^-CD56^-HLA\text{-}DR^+CD123^+$; CD8 T cells, $CD19^-CD3^+CD8^+$; CD4 T cells, $CD19^-CD3^+CD4^+$; NK cells, $CD19^-CD3^-CD14^-CD56^+$; cDC2s, $CD3^-CD19^-CD56^-CD123^-CD11c^+CD1c^+$; B cells, $CD3^-CD19^+$; and MNPs, $CD3^-CD19^-CD56^-CD123^-CD1c^-CD94^-CD11c^+$.

As with the GEX abundance analysis, a mixed-effects logistic regression model of cluster ~ 1 + comparison + (1|id) using the glmer function from lme4 in R was used.

Tissue and bulk TCR data generation

Four autopsy cases were identified with available matched irMyocarditis, tumour and histologically normal tissue adjacent to tumour. This normal adjacent tissue was used as control tissue. Formalin-fixed, paraffin-embedded (FFPE) slides were stained by H&E and annotated by a cardiac pathologist to indicate regions of myocardial inflammation, tumour and normal parenchyma. Marked regions of interest were manually macroscopically dissected using a scalpel to scrape tissue from serial unstained slides into 1.5 ml Eppendorf tubes pre-filled with 1 ml xylene. Genomic DNA was extracted using instructions from an AllPrep DNA/RNA FFPE kit (Qiagen). TCRβ-seq of the CDR3 region was performed (immunoSEQ human T-cell receptor beta (hsTCRB), Adaptive Biotechnologies)[70]. We also profiled heart tissue from three patients with cancer receiving an ICI who consented to our collection protocol, underwent an autopsy and did not have evidence of irMyocarditis (heart controls) (Supplementary Table 1).

Comparison of irMyocarditis and tumour TCRβ repertoires

For comparisons between heart and tumour TCR repertoires, the frequencies, and not the absolute counts, of TCR clones were compared to account for differential recovery of TCRβ sequences from various tissues[71]. Expanded TCRβ sequences were defined as those accounting for >0.5% of all TCRβ sequences recovered from the tissue of interest (heart or tumour). These expanded sequences were then filtered to exclude bystander TCRβ sequences by performing a Fisher's exact test on each, comparing the proportion of the TCRβ sequence in adjacent normal tissue to that of the tissue of interest (heart or tumour). Sequences with a FDR < 5% were considered enriched in their given tissue site (heart or tumour).

TCRβ sequence diversity

Diversity curves that measured Hill's diversity metric across diversity orders 0–4 were created using the package alakazam (v.1.0.2, R) with the alphaDiversity function[72]. Hill's diversity metric was only calculated on samples with ≥100 total TCRβ sequences.

Examination of shared TCRβ clones in heart and blood

Heart and PBMC single-cell data were combined with bulk TCRβ-seq data generated from heart tissue from active (SIC_1 and, SIC_264) or borderline irMyocarditis (SIC_136). For bulk TCRβ-seq data, expanded TCRβ sequences were defined as those that represented >0.5% of the bulk repertoire and were found to have a read count ≥2. For single-cell TCRβ-seq data, expanded TCRβ sequences were those that represented >0.5% of the single-cell TCRβ-seq repertoire and were found in ≥2 cells. For patients with both bulk TCRβ-seq and single-cell TCRβ-seq data, these data were analysed together. Expanded heart TCRβ clones were then compared with TCRβ clones recovered from PBMC scRNA-seq data. First, PBMC subsets were investigated for their association with the presence of expanded TCRβ heart clones by fitting a logistic regression model using the glmer function from the lme4 package (v.1.1-31, R). Each subset was modelled independently with the full model cluster ~ 1 + myo_clone, where myo_clone is a binary variable where the value was 1 if the cell had an expanded irMyocarditis TCRβ and 0 if it did not. An alternative null model cluster ~ 1 was then fit and a likelihood ratio test was used to compare the full and null models. Cell subsets with a FDR < 5% were considered to be enriched for expanded irMyocarditis TCRβ sequences. Additionally, we calculated the proportion of the repertoire that was overlapping with expanded heart TCRβ in each cellular subset for each donor and compared the proportions for each cluster. log + 1 transformed proportions for each cluster were compared between fatal and non-fatal cases using a two-sided *t*-test in R.

GLIPH

To discern TCR motifs, GLIPH2 was run on the TCRβ sequences derived from each donor individually[73,74] using the built-in naive CD8 TCR repertoire as a reference. The resulting GLIPH groups were then limited to those that had ≥3 unique TCRβ sequences. The TCRβ sequences from each GLIPH group were used to calculate the proportion that they represented in each tissue repertoire (irMyocarditis, tumour or control). GLIPH groups for which the proportion of the member TCRβ sequences represented >0.5% of the irMyocarditis and/or tumour tissue repertoires were considered expanded GLIPH groups.

TCR identification and antigen screening

A total of 52 TCRs were selected for antigen screening based on whether they met any of the following criteria: (1) containing a TCRβ that was enriched in the heart compared with adjacent normal control tissue from our bulk TCRβ-seq analysis ($n = 7$); (2) enriched in heart and tumour when compared with adjacent normal control tissue ($n = 2$); (3) expanded in the heart and found in the cycling b-CD8 subset of cells from our scRNA-seq PBMC data ($n = 7$); (4) expanded in the heart and found in our blood CD4 subclustering ($n = 4$); or comprising >1% of the captured bulk or single-cell TCR-seq repertoire from the heart ($n = 32$) (Supplementary Table 18).

V-D-J rearrangement of TCRα and TCRβ chains were identified from scRNA-seq or bulk TCRβ-seq data. For the latter TCRs, TCRβ chains were tracked in matched single-cell TCR-seq data in patient-matched blood and tissue data, and paired α-chains were deducted through analysis of single-cell TCR-seq. In cases for which a single TCRβ had multiple corresponding TCRα chains, both were tested separately. Classification of the 52 clonotypes were based on CD4 or CD8 based on scRNA-seq based clustering of the cells that transcribed that TCR; based on such distinction, the downstream analysis was performed on $CD4^+$ or $CD8^+$ transduced T cells, respectively. TCRs were reconstructed and

expressed in T cells from healthy donors, as previously described[75]. An additional TCR that was reported to recognize a 9-amino-acid peptide sequence in the α-myosin protein (RINATLETK) when displayed on an HLA-A*03:01 tetramer was also reconstructed for use as a positive control TCR (Myo-TCR)[16]. Background reactivity was assessed on T cells transduced with irrelevant TCRs isolated from unrelated patients[76]; untransduced T cells were tested in parallel as additional negative controls.

The full-length TCR α-chain and β-chain, separated by a Furin SGSG P2A linker, were synthesized in the TCRβ/TCRα orientation (Integrated DNA Technologies) and cloned into a lentiviral vector under the control of the pEF1a promoter using Gibson assembly (New England Biolabs). For generation of TCRs, full-length TCRα V-J regions were fused to optimized mouse TCRα constant chain, and the TCRβ V-D-J regions to optimized mouse TCRβ constant chain to allow preferential pairing of the introduced TCR chains, enhanced TCR surface expression and functionality[77,78].

Donor T cells enriched from PBMCs using a Pan-T cell selection kit (Miltenyi) were activated with anti-CD3/CD28 Dynabeads (Thermo Fisher Scientific) in the presence of 5 ng ml^{-1} IL-7 and IL-15 (Peprotech). Activated cells were transduced with a lentiviral vector encoding the TCRB–TCRA chains for 3 subsequent days. In brief, lentiviral particles were generated by transient transfection of the lentiviral packaging Lenti-X 293T cells (Takahara) with the TCR-encoding plasmids and packaging plasmids (VSVg and PSPAX2)[75] using Transit LT-1 (Mirus). Lentiviral supernatant was collected on days 1, 2 and 3 after transfection and used to transduce activated T cells. On day 2, transduction efficiency was increased by performing spinoculation of the virus at 2,000 r.p.m., 37 °C for 2 h in presence of polybrene (8 μg ml^{-1}, Sigma), and cells were cultured on viral supernatant for 3 days. At 6 days after activation, the beads were removed from culture, and cells were expanded in medium enriched with IL-7 and IL-15. Transduction efficiency was determined by flow cytometric analysis using an anti-mTCRB antibody (PE, clone H57-597, eBioscience, 12-5961-82, dilution 1:50). Transduced T cells were used at 14 days after transduction for TCR reactivity tests.

We utilized screening through upregulation of CD137 expression to determine the reactivity of reconstructed TCRs[75]. In brief, TCR-transduced T cell lines were washed, resuspended in PBS at 1×10^6 cells per ml and labelled with a combination of three dyes (Cell Trace CFSE, Far Red or Violet Proliferation Kits, Life Technologies). Up to 4 dilutions of Cell-trace Violet, 3 dilutions of Cell-trace Far Red or CFSE were created and then mixed, resulting in up to 36 colour combinations. After incubation at 37 °C for 20 min, T cells were washed twice, resuspended in complete medium and divided in pools. As internal controls, each pool contained a population of mock-transduced lymphocytes, a population of T cells transduced with an irrelevant TCR and a population of T cells expressing the Myo-TCR[16]. Next, 2.5×10^5 TCR-transduced T cells were put in contact with an equal number of patient-derived APCs pulsed with selected peptide pools (described below).

Epstein–Barr virus-immortalized lymphoblastoid B cell lines (EBV-LCLs) served as APCs, which were generated for five patients (SIC_48, SIC_171, SIC_232, SIC_258 and SIC_264). Additionally, for three patients (SIC_17, SIC_175 and SIC_317) for whom autologous EBV-LCL lines were not available, we screened 17 CD8 TCRs using single-HLA matching EBV-LCLs or monoallelic HLA class I lines[79] covering 6 out of 6 (SIC_17) or 5 out of 6 (SIC_175, SIC_317) patients' HLA class I alleles. APCs were pulsed with the following controls: DMSO (vehicle), or 10^7 pg ml^{-1} of RINATLETK peptide (positive control), Ova class I peptide (SIINFEKL; negative control), Ova class I peptide (ISQAVHAAHAEINEAGR; negative control) or CEF peptides (JPT, PM-CEF-S-1; negative control). The test conditions comprised custom crude peptide pools designed to cover the full-length α-myosin (encoded by *MYH6*), troponin I (encoded by *TNNI3*) and troponin T (encoded by *TNNT2*) proteins. Peptide sequences were up to 20-amino-acids long and tiled to achieve a 5-amino-acid overlap, similar to previous reports identifying α-myosin-reactive TCRs[16]. Overall, 6–8 test crude peptides were combined into a pool (Genscript; Supplementary Table 19).

After overnight incubation, TCR reactivity was measured through detection of CD137 surface expression (PE, clone 4B4-1, BioLegend, 309804, dilution 1:50) on CD8$^+$ (BV785, clone RPA-T8, BioLegend, 301046, dilution 1:100) or CD8$^-$ (CD4$^+$) TCR-transduced (mTCRB$^+$, PE-Cy7, clone H57-597, eBioscience, 25-5961-82, dilution 1:50) T cells using a Fortessa flow cytometer (BD Biosciences). Data were analysed using FlowJo software (v.10.8.2, BD Biosciences). For CD8 TCRs, CD137 upregulation was evaluated from the CD8$^+$ gate (Extended Data Fig. 6g), and for CD4 TCRs, CD137 upregulation was evaluated from a CD8$^-$ gate. Background CD137 reactivity, measured in the presence of target cells pulsed with DMSO, was subtracted. Data from the positive control Myo-TCR represent the results of that TCR tested against EBV-LCLs from a donor who has the HLA-A*03:01 allele.

IHC and H&E staining

FFPE tissue sections from seven hearts from patients with irMyocarditis and three hearts from ICI-treated patients without irMyocarditis were stained using a Leica Bond RX automated stainer. Anti-CD1c-OTI2F4 monoclonal antibody (Abcam, ab156708) were labelled with DAB chromogen (Leica Bond Polymer Refine Detection DS9800) using an EDTA-based pH 9 epitope retrieval condition and 20 μg ml^{-1} antibody concentration. FFPE tissue sections from irMyocarditis cases and heart control samples were manually stained with H&E.

Image acquisition of IHC and H&E images

Whole slide images of stained slides were acquired at ×40 (0.13 μm pixel^{-1}) resolution using a MoticEasyScan Infinity digital pathology scanner.

ISH–IF tissue staining

FFPE tissue sections from seven irMyocarditis cases and three heart control samples were stained using a Leica Bond RX automated stainer. The staining panel was developed using RNAscope ISH probes (Advanced Cell Diagnostics) with Opal fluorophores (Akoya Biosciences). The panel consisted of six RNA probes (Hs-COL1A-pool, Hs-CXCL9, Hs-CXCL10, Hs-CXCL11, Hs-FLT3LG and Hs-CD8A) and two antibodies targeting dendritic cells (anti-CD1c-OTI2F4 (Abcam, ab156708) and anti-CLEC9A (EPR22324) (Abcam, ab223188)). Hs-COL1A-pool consisted of probes for *COL1A1* and *COL1A2*. The three CXC chemokine probes were pooled into a single fluorophore channel. The two antibodies were also pooled into a single fluorophore channel. Tyramide signal amplification was used to boost fluorophore signals (Opal 690, Opal 520, Opal 620, Opal 480 and Opal 780). Opal fluorophore concentrations were optimized to balance signal intensity across all channels. DAPI was used as a nuclear counterstain. *FLT3LG* was expressed diffusely, and we were unable to discern a clear signal for downstream analysis.

ISH–IF image acquisition

Whole slide images were acquired on an Akoya PhenoImager HT multi-spectral slide scanner at ×20 (0.5 μm pixel^{-1}) resolution. Exposures were set for each image individually to avoid pixel saturation or underexposure. Akoya inForm software was used to spectrally separate signals from each fluorophore and to mitigate the effect of native tissue autofluorescence. The spectral library used to unmix the raw images was created using the synthetic Opal spectra and autofluorescence spectra from unstained human heart tissue. Unmixed tiles produced by inForm were stitched to reproduce a whole-slide pyramidal TIF using Indica Labs HALO software.

Image analysis

Quantitative image analysis was performed using the HALO image analysis platform (v.3.6.4134.137, Indica Labs). Images were manually annotated for regions to analyse. For all samples, the whole image was analysed excluding manually annotated areas of debris, tissue folds and

large vessels. For the irMyocarditis cases, additional targeted analysis was performed on regions of inflamed and non-inflamed heart tissue that were annotated based on pathologist review of serial section H&E slides.

Cell segmentation and phenotyping were performed within annotated tissue regions using the HALO FISH-IF (v.2.2.5) and AI (v.3.6.4134) modules. Nuclear detection and cell segmentation were performed using the default AI nuclear segmentation algorithm based on the DAPI channel. Cells were phenotyped as CD1c/CLEC9A$^+$ based on signal intensity of the antibody channel within the nuclear and cytoplasmic compartments. RNA–ISH positivity was based on signal intensity and dot size within a cell, with brighter and larger dots having more weight. Cell phenotypes were also defined using multiple marker criteria (positive for *COL1A1*, *COL1A2*, *CXCL9*, *CXCL10* and *CXCL11*). The positivity thresholds were manually validated for each sample for cell phenotyping quality. Summary tables containing cell phenotype information for each region of analysis (whole slide, inflamed regions, non-inflamed regions) were exported for further analysis across all samples. HALO Nearest Neighbour Spatial analysis was performed on the phenotyped cells to determine the average distance from each CD1c/CLEC9A$^+$ to the nearest *CD8A*$^+$ cell. For comparisons of cell proportions between irMyocarditis versus control samples, a one-sided Mann-Whitney *U*-test was used given our data did not have a normal distribution (potentially due to the low number of samples). For our paired analysis between inflamed and non-inflamed tissue, we used a one-sided paired *t*-test.

Reporting summary

Further information on research design is available in the Nature Portfolio Reporting Summary linked to this article.

Data availability

scRNA-seq count matrices from this study and related data as well as TCR-seq data have been deposited into the Gene Expression Omnibus database (under accession GSE228597), and raw human sequencing data are available in the controlled access repository dbGaP (https://www.ncbi.nlm.nih.gov/gap; accession phs003413.v1.p1). Public Heart Atlas data[18] utilized as heart control samples in our study are accessible from the Human Cell Atlas Data Coordination Platform with accession number ERP123138. Reads from scRNA-seq experiments were aligned to the human reference genome (GRCh38, v.3.0.0 from 10x Genomics).

Code availability

Source code for data analysis is available from GitHub (https://github.com/villani-lab/myocarditis) and has been archived to Zenodo (https://zenodo.org/doi/10.5281/zenodo.11519192)[80]. A full list of software packages and versions included in the analyses is included in Supplementary Table 21. A user-friendly portal[81] is available to browse the single-cell data generated in this article at the Villani Laboratory website (https://villani.mgh.harvard.edu/myocarditis).

55. Friedrich, M. G. et al. Cardiovascular magnetic resonance in myocarditis: a JACC white paper. *J. Am. Coll. Cardiol.* **53**, 1475–1487 (2009).
56. Tucker, N. R. et al. Transcriptional and cellular diversity of the human heart. *Circulation* **142**, 466–482 (2020).
57. Aretz, H. T. et al. Myocarditis. A histopathologic definition and classification. *Am. J. Cardiovasc. Pathol.* **1**, 3–14 (1987).
58. Zheng, G. X. Y. et al. Massively parallel digital transcriptional profiling of single cells. *Nat. Commun.* **8**, 14049 (2017).
59. Li, B. et al. Cumulus provides cloud-based data analysis for large-scale single-cell and single-nucleus RNA-seq. *Nat. Methods* **17**, 793–798 (2020).
60. Gaublomme, J. T. et al. Nuclei multiplexing with barcoded antibodies for single-nucleus genomics. *Nat. Commun.* **10**, 2907 (2019).
61. Villani, A. C. et al. Single-cell RNA-seq reveals new types of human blood dendritic cells, monocytes, and progenitors. *Science* **356**, eaah4573 (2017).
62. Huang, X. & Huang, Y. Cellsnp-lite: an efficient tool for genotyping single cells. *Bioinformatics* **37**, 4569–4571 (2021).
63. Heaton, H. et al. Souporcell: robust clustering of single-cell RNA-seq data by genotype without reference genotypes. *Nat. Methods* **17**, 615–620 (2020).
64. Huang, Y., McCarthy, D. J. & Stegle, O. Vireo: Bayesian demultiplexing of pooled single-cell RNA-seq data without genotype reference. *Genome Biol.* **20**, 273 (2019).
65. Korsunsky, I. et al. Fast, sensitive and accurate integration of single-cell data with Harmony. *Nat. Methods* **16**, 1289–1296 (2019).
66. Batson, J., Royer, L. & Webber, J. Molecular cross-validation for single-cell RNA-seq. Preprint at *bioRxiv* https://doi.org/10.1101/786269 (2019).
67. Lun, A. T. L., Bach, K. & Marioni, J. C. Pooling across cells to normalize single-cell RNA sequencing data with many zero counts. *Genome Biol.* **17**, 75 (2016).
68. Ritchie, M. E. et al. limma powers differential expression analyses for RNA-sequencing and microarray studies. *Nucleic Acids Res.* **43**, e47 (2015).
69. Fonseka, C. Y. et al. Mixed-effects association of single cells identifies an expanded effectorCD4$^+$ T cell subset in rheumatoid arthritis. *Sci. Transl. Med.* **463**, eaaq0305 (2018).
70. Sherwood, A. M. et al. Deep sequencing of the human TCRγ and TCRβ repertoires suggests that TCRβ rearranges after αβ and γδ T cell commitment. *Sci. Transl. Med.* **3**, 90ra61 (2011).
71. Cottrell, T. et al. Evaluating T-cell cross-reactivity between tumors and immune-related adverse events with TCR sequencing: pitfalls in interpretations of functional relevance. *J. Immunother. Cancer* **9**, e002642 (2021).
72. Gupta, N. T. et al. Change-O: a toolkit for analyzing large-scale B cell immunoglobulin repertoire sequencing data. *Bioinformatics* **31**, 3356–3358 (2015).
73. Glanville, J. et al. Identifying specificity groups in the T cell receptor repertoire. *Nature* **547**, 94–98 (2017).
74. Huang, H., Wang, C., Rubelt, F., Scriba, T. J. & Davis, M. M. Analyzing the *Mycobacterium tuberculosis* immune response by T-cell receptor clustering with GLIPH2 and genome-wide antigen screening. *Nat. Biotechnol.* **38**, 1194–1202 (2020).
75. Oliveira, G. et al. Phenotype, specificity and avidity of antitumour CD8$^+$ T cells in melanoma. *Nature* **596**, 119–125 (2021).
76. Keskin, D. B. et al. Neoantigen vaccine generates intratumoral T cell responses in phase Ib glioblastoma trial. *Nature* **565**, 234–239 (2019).
77. Cohen, C. J. et al. Enhanced antitumor activity of T cells engineered to express T-cell receptors with a second disulfide bond. *Cancer Res.* **67**, 3898–3903 (2007).
78. Haga-Friedman, A., Horovitz-Fried, M. & Cohen, C. J. Incorporation of transmembrane hydrophobic mutations in the TCR enhance its surface expression and T cell functional avidity. *J. Immunol.* **188**, 5538–5546 (2012).
79. Abelin, J. G. et al. Mass spectrometry profiling of HLA-associated peptidomes in mono-allelic cells enables more accurate epitope prediction. *Immunity* **46**, 315–326 (2017).
80. nealpsmith, swemeshy & ikernin. villani-lab/myocarditis: Publication code release (v1.0.0). *Zenodo* https://doi.org/10.5281/zenodo.11519193 (2024).
81. Slowikowski, K. cellguide: Navigate single-cell RNA-seq datasets in your web browser (v0.01). *Zenodo* https://doi.org/10.5281/zenodo.8144195 (2023).

Acknowledgements We are grateful to all donors and their families; staff at the Mass General Cancer Center, Ellison 16 staff and staff at the cardiac catheterization laboratory and the Severe Immunotherapy Complications Service for their collaboration and support; staff at the Teichmann Laboratory for facilitating access to the Human Heart Cell Atlas data and their guidance in navigating this dataset[18]. S.M.B. was supported by a National Institutes of Health T32 Award (2T32CA071345-21A1) and a SITC-Mallinckrodt Pharmaceuticals Adverse Events in Cancer Immunotherapy Clinical Fellowship. D.A.Z. was supported by a National Institutes of Health T32 Award T32HL007208 and K24HL150238-02. L.Z. was supported by the Spanish Society of Medical Oncology (SEOM) grant for a 2-year translational project at the MGH Cancer Center. K.S. was supported by a NIAID grant T32AR007258. P.S. is supported by the National Institutes of Health K08 Award (NHLBI K08 HL157725) and American Heart Association Career Development Award. M.M.-K. was in part supported by a grant from the National Institutes of Health (R01CA240317). G.O. was supported by the Claudia Adams Barr Program for Innovative Cancer Research and by DF/HCC Kidney Cancer SPORE P50 CA101942. M.F.T. is supported by the National Institutes of Health K08 Award (1K08DK127246-01A1) and was supported by a National Institutes of Health T32 Award (T32DK007191). G.M.B. is supported by an Adelson Foundation award. T.G.N is supported by a gift from A. Curt Greer and P. Kohlberg and from C. and P. Kazilionis, the Michael and Kathryn Park Endowed Chair in Cardiology, a Hassenfeld Scholar Award, and has additional grant funding from the National Institutes of Health/National Heart, Lung, and Blood Institute (R01HL137562, K24HL150238 and R01HL130539). This work was made possible by support from the National Institute of Health Director's New Innovator Award (DP2CA247831 to A.-C.V.), the Massachusetts General Hospital Transformative Scholar in Medicine Award (to A.-C.V.), the Damon Runyon-Rachleff Innovation Award (to A.-C.V.), The Melanoma Research Alliance Young Investigator Award (https://doi.org/10.48050/pc.gr.143739 to A.-C.V.), the MGH Howard M. Goodman Fellowship (to A.-C.V.), the Arthur, Sandra, and Sarah Irving Fund for Gastrointestinal Immuno-Oncology (to A.-C.V.), the Kraft Foundation Award (to. K.L.R. and A.-C.V.), and by the support of an anonymous donor (to. K.L.R. and A.-C.V.).

Author contributions S.M.B., D.A.Z., M.F.T., K.L.R., T.G.N. and A.-C.V. conceived and led the study. S.M.B., D.A.Z., M.F.T. and A.-C.V. led the experimental design. S.M.B., D.A.Z., M.F.T. and P.S. carried out experiments (with assistance from N.S., S.M., A.T., K.M., J.T., B.Y.A. and J.B.). N.P.S., I.J.K., S.R., K.S. and M.N. designed and performed computational analyses, visualization and data portals. S.M.B., D.A.Z., Y.S., K.H.X. and L.T.N. designed and performed the microscopy experiments. S.M.B., D.A.Z., N.P.S., C.J.W. and G.O. designed and performed the antigen screening experiments. S.M.B., D.A.Z., L.Z., M.W., P.C., C.J.P., D.M., A.L., W.A.M., T.S., M.J., J.F.G., D.J., M.M.-K., R.J.S., G.M.B., J.R.S., T.G.N. and K.L.R. provided clinical expertise, coordinated and performed sample acquisition and/or established research protocols. M.M-K. and J.R.S. provided histopathology expertise. J.C. performed endomyocardial biopsies. A.-C.V. managed and supervised the study. A.-C.V., T.G.N. and K.L.R. provided funding for this work. S.M.B., D.A.Z., N.P.S., I.J.K., S.R. and A.-C.V. wrote the manuscript, with input from all authors.

Competing interests S.M.B.: consultant to Two River Consulting and Third Rock Ventures; and equity in Candid Therapeutics, Kronos Bio, 76Bio and Allogene Therapeutics. D.A.Z.: consultant to Bristol Myers Squibb, Freeline Therapeutics and Intrinsic Imaging; and research funding from Abbott Laboratories. N.P.S.: consultant to Hera Biotech. L.Z.: consultant to Bristol Myers Squibb and Merck. J.F.G.: consultant to Amgen, Arcus Biosciences, AI Proteins, AstraZeneca, Beigene, Blueprint Medicines, Bristol Myers Squibb, Genentech/Roche, EMD Serono, InterVenn Biosciences, Gilead Sciences, iTeos Therapeutics, Jounce Therapeutics, Karyopharm Therapeutics, Lilly, Loxo, Merus, Mirati Therapeutics, Pfizer, Sanofi, Silverback Therapeutics, Merck, Moderna Therapeutics, Mariana Oncology and Takeda; honorarium from Merck, Pfizer, Novartis, Pfizer and Takeda; research funding from Adaptimmune, Alexo Therapeutics, Array BioPharma, AstraZeneca, Blueprint Medicines, Bristol Myers Squibb, Genentech, Jounce Therapeutics, Merck, Moderna Therapeutics, Novartis and Tesaro; has an immediate family member who is an employee with stock and other ownership interests in Ironwood Pharmaceuticals; and equity in AI Proteins. C.J.W.: equity in BionTech; research funding from Pharmacyclics; and is on the scientific advisory board of Repertoire, Adventris and Aethon Therapeutics. D.J.: grants and personal fees from Novartis, Genentech, Syros and Eisai; personal fees from Vibliome, PIC Therapeutics, Mapkure and Relay Therapeutics; and grants from Pfizer, Amgen, InventisBio, Arvinas, Takeda, Blueprint Medicines, AstraZeneca, Ribon Therapeutics and Infinity that are outside the submitted work. M.M.-K.: consultant to AstraZeneca, Pfizer, Repare, Boehringer Ingelheim, Sanofi, AbbVie and Daiichi-Sankyo; and royalties from Elsevier. G.O.: consultant to Bicycle Therapeutics. R.J.S.: consultant to Bristol Myers Squibb, Merck, Pfizer, Marengo Therapeutics, Novartis, Eisai, Iovance, OncoSec and AstraZeneca; and research funding from Merck. G.M.B.: sponsored research agreements through her institution with Olink Proteomics, Teiko Bio, InterVenn Biosciences and Palleon Pharmaceuticals; is on advisory boards for Iovance, Merck, Nektar Therapeutics, Novartis and Ankyra Therapeutics; is a consultant for Merck, InterVenn Biosciences, Iovance and Ankyra Therapeutics; and has equity in Ankyra Therapeutics. T.G.N.: consultant to Bristol Myers Squibb, Genentech, CRC Oncology, Roche, Sanofi and Parexel Imaging Pharmaceuticals; and grant funding from Astra Zeneca, Bristol Myers Squibb related to the cardiac effects of ICIs. K.L.R.: on the advisory board to SAGA Diagnostics; speaker's fees from CMEOutfitters and Medscape; and research funding from Bristol Myers Squibb. A.-C.V.: consultant to Bristol Myers Squibb; and financial interest in 10x Genomics. 10x Genomics designs and manufactures gene sequencing technology for use in research, and such technology is being used in this research; these interests were reviewed by the Massachusetts General Hospital and Mass General Brigham in accordance with their institutional policies. All other authors (I.J.K., S.R., J.C., N.S., S.M., M.W., A.T., Y.S., K.H.X., J.B., P.S., K.S., J.T., K.M., B.Y.A., M.N., C.J.P., D.M., M.J., P.C., A.L., W.A.M., T.S., L.T.N., J.R.S. and M.F.T.) declare no competing interests.

Additional information

Supplementary information The online version contains supplementary material available at https://doi.org/10.1038/s41586-024-08105-5.

Correspondence and requests for materials should be addressed to Alexandra-Chloé Villani.

Peer review information *Nature* thanks the anonymous reviewers for their contribution to the peer review of this work. Peer reviewer reports are available.

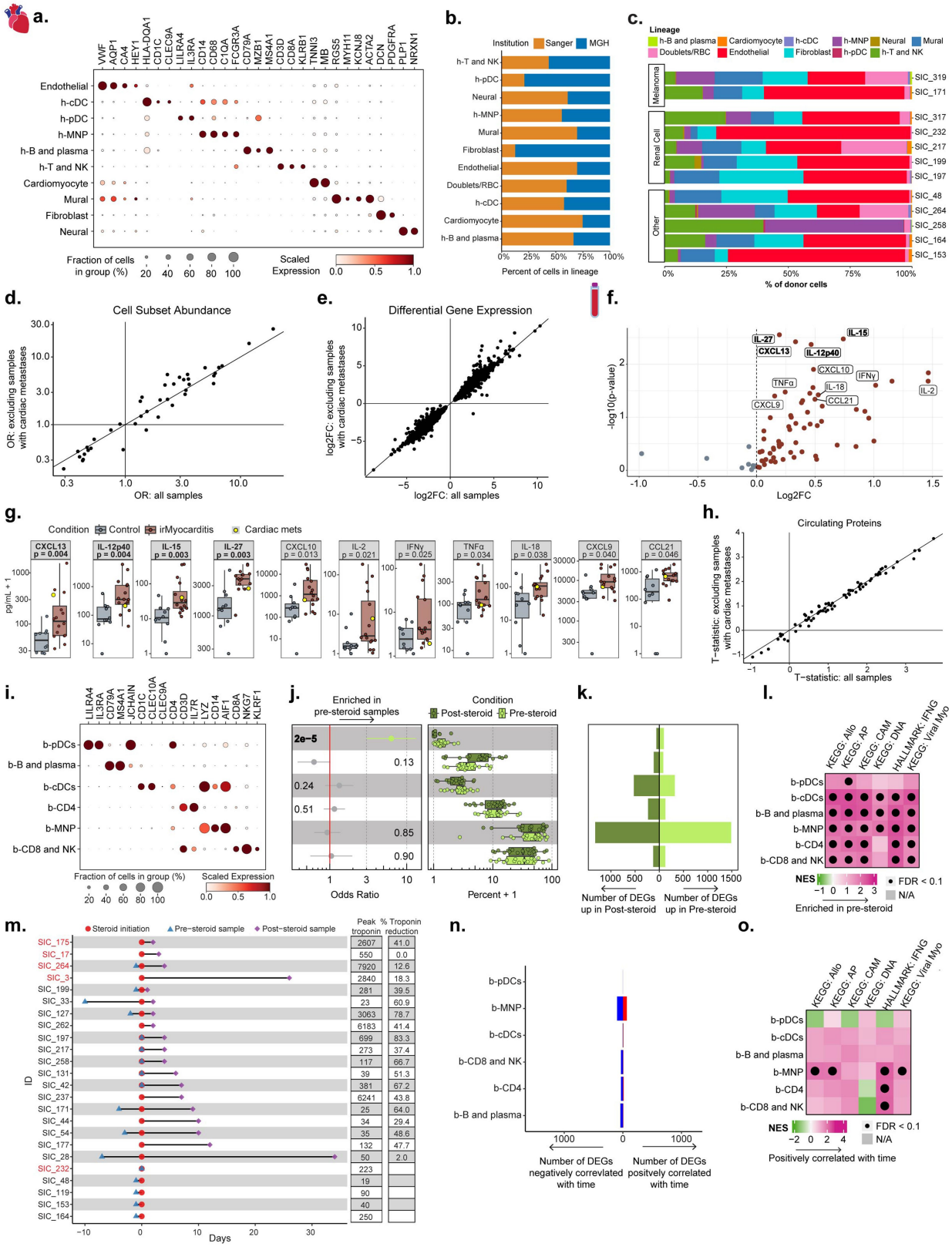

Extended Data Fig. 1 | See next page for caption.

Extended Data Fig. 1 | Cell lineages in heart and blood defined by scRNA-seq. a, Dot plot showing top marker genes for each lineage in the heart. Dot size represents the percent of cells in the lineage with non-zero expression of a given gene. Colour indicates scaled expression across lineages. **b**, Stacked bar plots showing the composition of major cell lineages, coloured by data source ("MGH" refers to data generated in this study; "Sanger" refers to public heart atlas data)[29]. **c**, Stacked bar plot showing the lineage composition per patient, grouped by the histology of the primary malignancy. **d**, Differential abundance of cell subsets in scRNA-seq data from the heart, comparing irMyocarditis cases to controls. Each point represents a cell subset. The x-axis represents the odds ratio (OR) in all cases and controls, and the y-axis represents the OR in an analysis that excluded cases (SIC_171 and SIC_232) and a control (SIC_182) with evidence of cardiac metastases. **e**, Differentially expressed genes in scRNA-seq data from the heart, comparing irMyocarditis cases to controls. Each point represents a gene contrasted in each cluster. The x-axis represents the log2 fold change (log2FC) in all cases and controls, and the y-axis represents the log2FC in an analysis that excluded samples with evidence of cardiac metastases. **f**, A volcano plot depicting 71 cytokines and chemokines measured in serum from irMyocarditis and control patients, where each point represents a protein. The x-axis represents log2FC between irMyocarditis (n = 16) and control samples (n = 10), and the y-axis represents −log10(*P* value) of the comparison. Proteins are coloured based on enrichment in irMyocarditis cases (red, right side) and controls (blue, left side). Select proteins with an unadjusted $p < 0.05$ are labeled, and those with FDR < 0.1 are in bold (two-sided t-test). **g**, Box plots showing serum concentrations of selected cytokines and chemokines in irMyocarditis cases (n = 16, red) and controls (n = 10, blue) (two-sided t-test). Data points from a patient with evidence of regressed cardiac metastases (SIC_171) are highlighted in yellow. **h**, Circulating protein analysis, comparing irMyocarditis cases to controls where each point represents a circulating protein. The x-axis represents the t-statistic in all cases and controls, and the y-axis represents the t-statistic in an analysis that excluded the sample with evidence of cardiac metastases (SIC_171). **i**, Dot plot showing top marker genes for each lineage in the blood. Dot size represents the percent of cells in the lineage with non-zero expression of a given gene. Colour indicates scaled expression across lineages. **j**, Abundance analysis comparing PBMC samples from irMyocarditis cases prior to the initiation of corticosteroids ("pre-steroid," n = 17, light green) to samples from irMyocarditis patients shortly after the initiation of high-dose corticosteroids ("post-steroid," n = 19, dark green). Left: dots represent logistic regression odds-ratios. Error bars represent 95% confidence intervals. Unadjusted two-sided likelihood-ratio test *P* values for each subset are shown. Colour and bolded *P* value indicates FDR < 0.1. Right: individual-level data showing the frequency of the indicated lineages; each dot represents a patient. **k**, the number of DEGs for each cell lineage when comparing pre-steroid (right, light green) to post-steroid samples (left, dark green). **l**, GSEA of select gene sets by heart cell lineages, colour-coded by NES of differential gene expression of irMyocarditis pre-steroid samples compared to post-steroid samples. **m**, Left: timelines of blood collections for irMyocarditis patients included in the pre- and post-steroid analysis (n = 24). The length of the lines represents the relative time interval between the pre- and post-steroid samples and the time of steroid initiation. Right: peak troponin (ng/L) and percentage troponin reduction from peak at the time of post-steroid blood collection are shown. Fatal cases are shown in red, and cases are ordered by fatal status followed by interval between steroid initiation and post-steroid sample collection. Full patient metadata is available in Supplementary Table 1. **n**, The number of DEGs positively (red, right) and inversely (blue, left) correlated with time from steroid initiation in post-steroid samples are shown. **o**, GSEA of select gene sets when modeled by time from steroid initiation. For **g** and **j**, box plots display the median (line) and IQR, with whiskers no more than 1.5x IQR, and each dot represents one patient **Related to** Fig. 1. Abbreviations: Allo, allograft rejection; AP, antigen presentation; CAM, cell adhesion molecules; DNA, DNA synthesis; IFNG, interferon-γ signalling; KEGG, Kyoto Encyclopedia of Genes and Genomes NES, normalized enrichment score; Viral Myo, viral myocarditis.

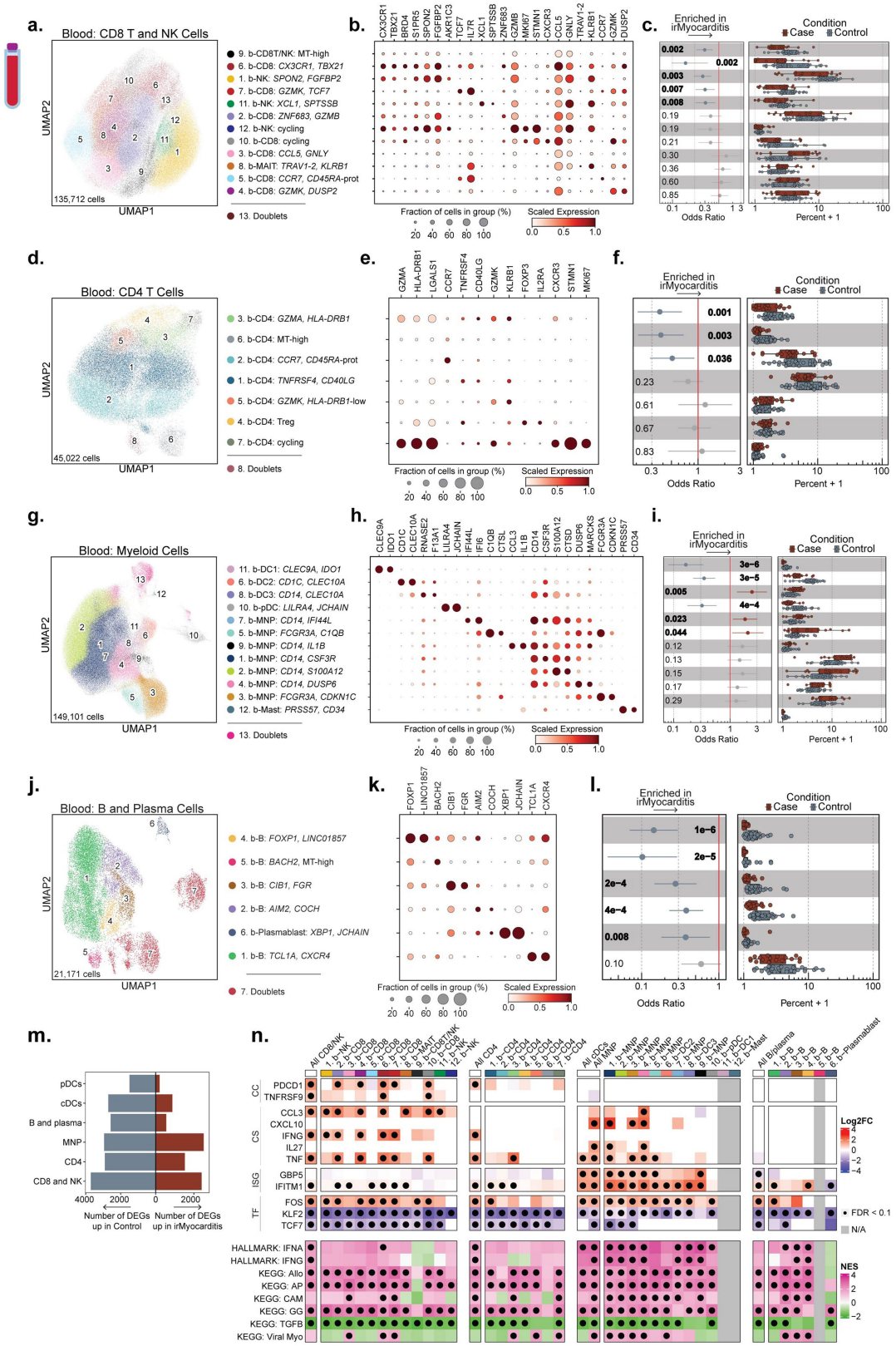

Extended Data Fig. 2 | See next page for caption.

Extended Data Fig. 2 | PBMC cell subsets and transcriptional changes associated with irMyocarditis onset. a, **b**, **c**, 135,712 circulating CD8T and NK cells are (**a**) displayed on a UMAP embedding with (**b**) a dot plot to show top marker genes for each subset and (**c**) case versus control abundance analysis. **d**, **e**, **f**, 45,022 circulating CD4T cells are (**d**) displayed on a UMAP embedding with (**e**) a dot plot of top marker genes and (**f**) case versus control abundance analysis. **g**, **h**, **i**, 149,101 circulating cDC, pDC, and MNP cells are (**g**) displayed on a UMAP embedding with (**h**) a dot plot of top marker genes and (**i**) case versus control abundance analysis. **j**, **k**, **l**, 21,171 circulating B and plasmablast cells (**j**) displayed on a UMAP embedding with (**k**) a dot plot showing selected marker genes for each subset and (**l**) case versus control abundance analysis. **m**, The number of DEGs (FDR < 0.1, Wald test) for each cell lineage when comparing pre-steroid irMyocarditis samples (n = 17, red, right) to ICI-treated controls (n = 28, blue, left). **n**, Heatmap showing selected differentially expressed genes (irMyocarditis versus control) and gene sets across each PBMC cell subset and lineage, grouped by biological themes. Colour scale indicates log2FC difference between irMyocarditis cases and controls for DEG analysis and NES for GSEA. Black dots indicate FDR < 0.1 (Wald test). In **a**, **d**, **g**, and **j**, UMAP pseudocolouring corresponds to the cell subsets labeled on the right. In **b**, **e**, **h**, and **k**, dot plots show top marker genes for each cell subset. Dot size represents the percent of cells in the subset with non-zero expression of a given gene. Colour indicates scaled expression across subsets. For **c**, **f**, **i**, and **l**, cell subset differential abundance analysis comparing pre-steroid samples from irMyocarditis cases at the pre-steroid timepoint (n = 17, red) to ICI-treated controls (n = 28, blue). Left panels: dots represent logistic regression odds-ratios. Error bars represent 95% confidence intervals. Unadjusted two-sided likelihood-ratio test *P* values for each subset are shown. Colour and bolded *P* value indicates FDR < 0.1. Right panels: box plots display the median (line) and IQR, with whiskers no more than 1.5x IQR. Each dot represents one patient. Abbreviations: Allo, allograft rejection; AP, antigen presentation; CAM, cell adhesion molecules; CC, co-inhibition or co-stimulation; CS; cytokine signalling; GG, glycolysis and gluconeogenesis; IFNA, interferon-α signalling; IFNG, interferon-γ signalling; ISG; interferon-stimulated genes; KEGG, Kyoto Encyclopedia of Genes and Genomes; NES, normalized enrichment score; TF, transcription factors; TGFB; TGF-β signalling; Viral Myo, viral myocarditis. **Related to** Fig. 1.

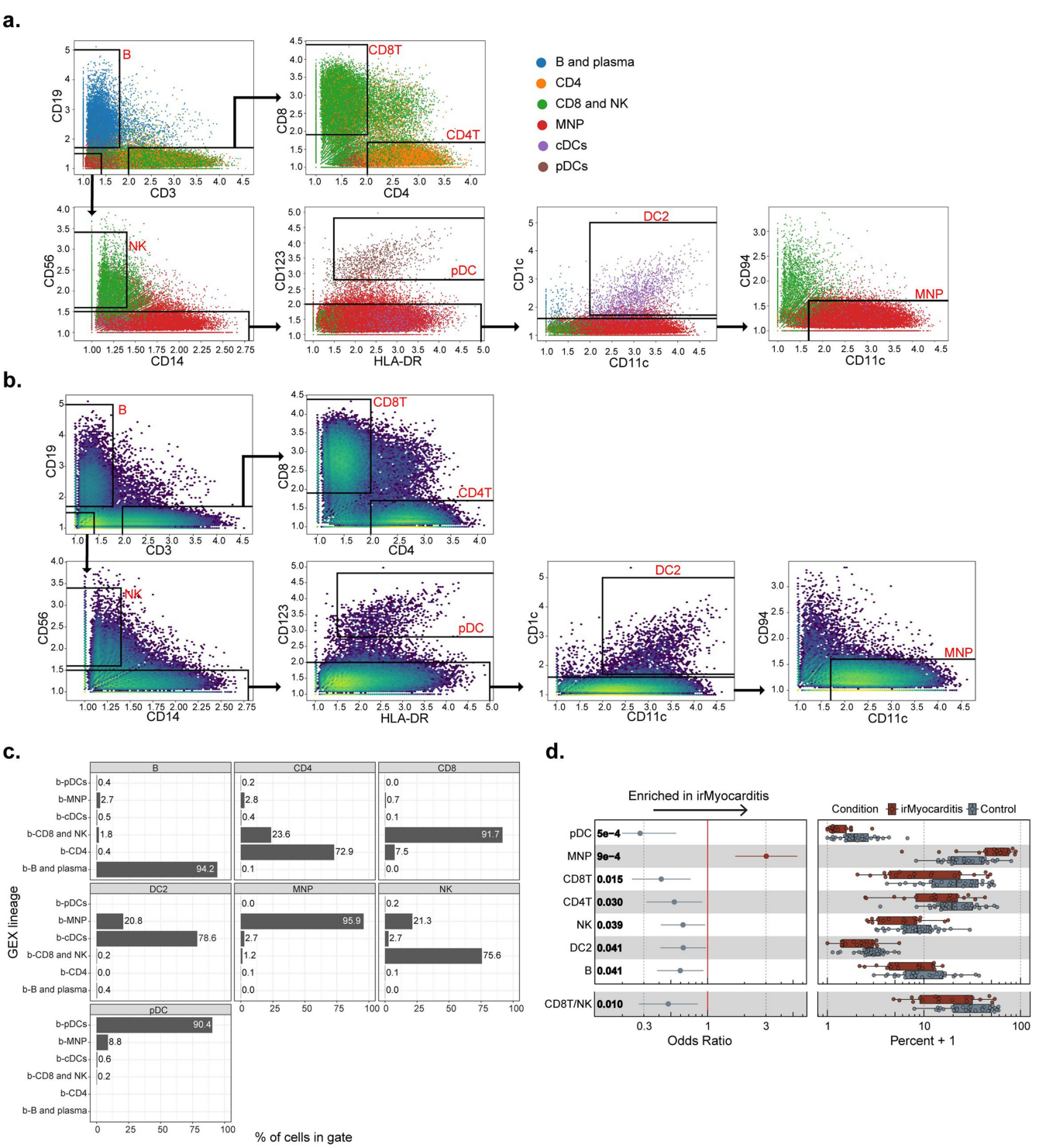

Extended Data Fig. 3 | Blood CITE-Seq surface protein analysis. a, **b**, Scatter plots showing transformed counts of the listed proteins in our CITE-Seq data. Boxes and arrows indicate the gating strategy used to define the populations labeled in red and analyzed in panels **c** and **d**. The same data are shown pseudocoloured by the lineage assigned to those cells by (**a**) scRNA-seq and (**b**) as density plots. **c**, Bar plots showing the percent of the cells in each indicated CITE-Seq-defined lineage that were assigned to each scRNA-seq-defined blood lineage (rows). **d**, Abundance analysis comparing the frequencies of CITE-seq defined populations from pre-steroid irMyocarditis cases (n = 17, red) to ICI-treated controls (n = 28, blue). Left: dots represent logistic regression odds-ratios. Error bars represent 95% confidence intervals. Unadjusted two-sided likelihood-ratio test *P* values for each population is shown. Colour and bolded *P* value indicates FDR < 0.1. Right: box plots display the median (line) and IQR, with whiskers no more than 1.5x IQR. Each dot represents one patient. Composition is reported as the percent of all PBMCs from a patient in each subset. The last row, "CD8/NK" is the sum of the "CD8T" and "NK" gates, included to mirror the scRNA-seq lineage level clustering solution. **Related to** Fig. 1.

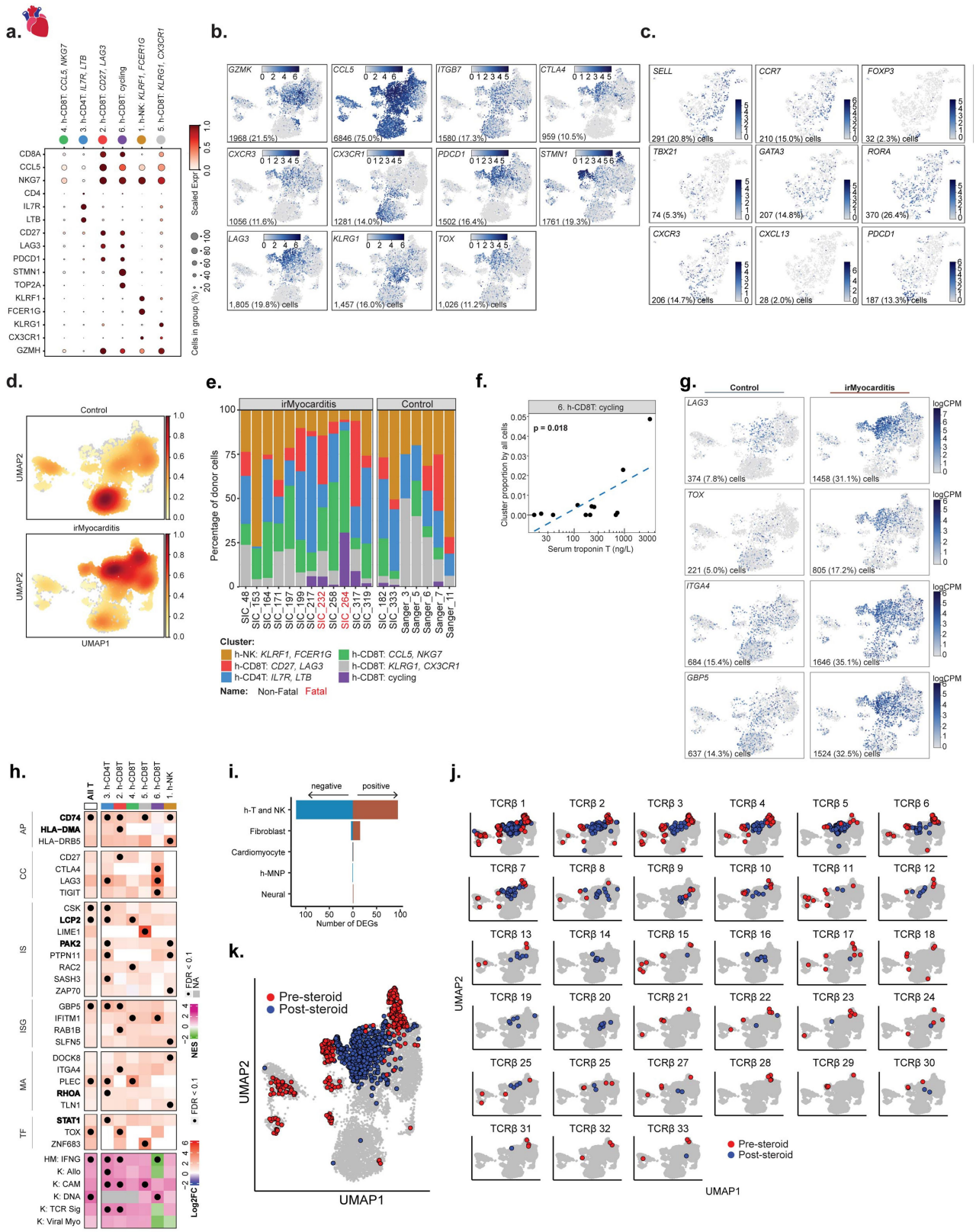

Extended Data Fig. 4 | See next page for caption.

Extended Data Fig. 4 | Lymphoid cells in irMyocarditis tissue. a, Selected marker genes for each T/NK cell subset. Dot size represents the percent of cells in the subset with non-zero expression of a given gene. Colour indicates scaled expression. **b**, Feature plots using colour to indicate gene expression (logCPM) levels of the indicated genes projected onto the T/NK UMAP embedding. Cell numbers and percentages represent gene expression across all heart T and NK cells. **c**, Feature plots using colour to indicate gene expression (logCPM) levels of the indicated genes projected onto the heart h-CD4T subset. Cell numbers and percentages represent gene expression in this subset only. **d**, UMAP embedding of cell density displaying the relative proportion of cells from irMyocarditis cases (n = 4,686) and controls (n = 4,448). **e**, Stacked bar plots showing the per-subset cellular composition per donor of each pre-steroid or unenriched control sample. Red patient labels denote samples from patients with fatal irMyocarditis. **f**, Plot showing the intracardiac frequency of h-CD8T^{cycling} cells (y-axis) versus serum troponin T level (x-axis) for irMyocarditis samples (n = 12). Linear regression p = 0.018, FDR < 0.1. **g**, Feature plots using colour to indicate gene expression (logCPM) levels of the indicated genes expressed by control (left) or irMyocarditis samples (right), projected onto the heart T/NK UMAP embedding. Cell numbers and percentages represent gene expression across T/NK cells in control or irMyocarditis samples. **h**, Top: heatmap showing selected DEGs across T/NK subsets from irMyocarditis versus control heart samples, grouped by biological categories. Colour scale indicates log2FC. Black dots indicate FDR < 0.1 (Wald test). Bottom: select GSEA results, colour-coded by NES of the gene set in irMyocarditis cases versus controls. "All T" row depicts pseudo-bulk DGE analysis of pooled T-cell subsets (subsets 2–6) that excluded NK cells. Bolded genes in the heatmap indicate leading edge genes in ≥1 GSEA gene set in ≥4 subsets. **i**, Bar graph showing the number of DEGs per lineage when gene expression was modeled against serum troponin T level, showing positively correlated (right, red) and negatively correlated (left, blue) genes. Only lineages with at least one troponin T-associated DEG are displayed. **j**, **k**, The 33 expanded TCR-β sequences (> 0.5% of TCR-β repertoire) from patient SIC_264 in T/NK UMAP space, colour coded by whether the cell was found prior to ("pre-steroid", red) or after ("post-steroid", blue) administration of corticosteroids and second-line immunosuppression. Data shown by (**j**) TCR-β clone and (**k**) in aggregate of all clones. Abbreviations: Allo, allograft rejection; AP, antigen presentation; CAM, cell adhesion molecules; CC, co-inhibition or co-stimulation; DNA, DNA synthesis; HM, Hallmark; IFNG, interferon-γ signalling; IS, immunoreceptor signalling; ISG, interferon-stimulated genes; K, Kyoto Encyclopedia of Genes and Genomes; MA, motility and adhesion; NES, normalized enrichment score; TCR Sig, TCR signalling; TF, transcription factors; Viral Myo, viral myocarditis. **Related to** Fig. 2.

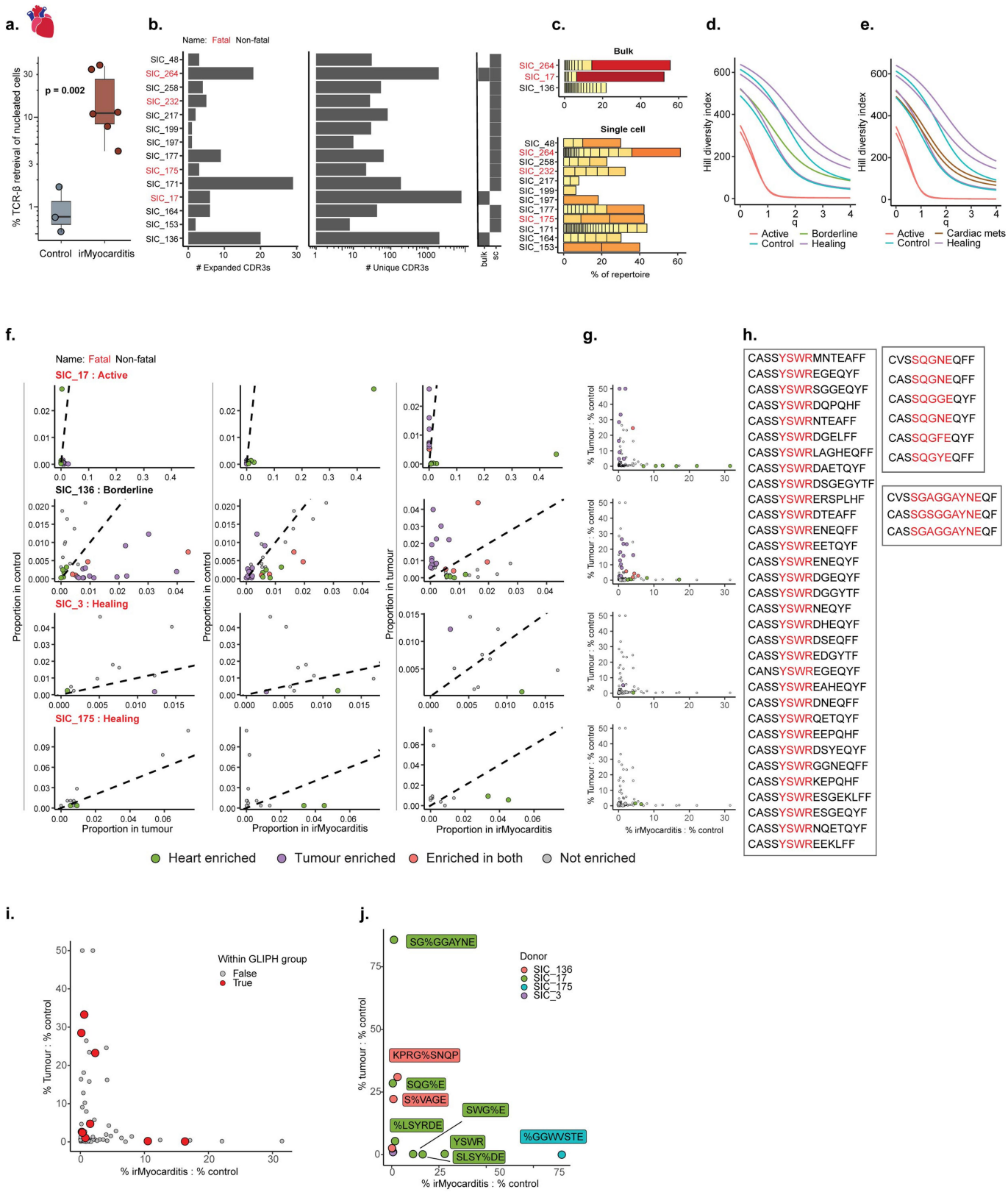

Extended Data Fig. 5 | See next page for caption.

Extended Data Fig. 5 | Expanded T-cell receptor β (TCR-β) sequences in irMyocarditis tissue and tumour. a, A box plot showing the relative proportion of cells that recovered a TCR-β CDR3 sequence from marked areas of irMyocarditis (n = 6, red) and control (n = 3, blue) tissue; p = 0.002 by two-sided t-test (via Adaptive Biotechnologies). Median and IRQ are shown, with whiskers no more than 1.5x IQR. Each dot represents one patient. **b**, Expanded TCR-β CDR3 (left) and total unique TCR-β CDR3 sequences (right) recovered on a per patient basis from both scRNA-seq and bulk TCR-β sequencing. **c**, Expanded TCR-β CDR3 from bulk sequencing (top) and scRNA-seq data (bottom) from irMyocarditis patients with matched blood samples. Donors with "healing" irMyocarditis were excluded. **d**, **e**, Smoothed Hill's diversity index curves at diversity orders 0–4 for the TCR-β repertoires of irMyocarditis tissues (**d**) without diffuse metastases, coloured by histologic appearance at the time of autopsy, and (**e**) with an additional case with diffuse cardiac metastases (SIC_232) coloured by histologic appearance at the time of autopsy and by the presence of cardiac metastases (SIC_232 and SIC_136). **f**, Within each tissue type in each patient ("control", "tumour", or "irMyocarditis"), the frequency of each TCR-β clone is plotted on a per-patient basis and labeled by the pathological designation of the macroscopically dissected regions (SIC_17: Active; SIC_136: Borderline; SIC_3: Healing; SIC_175: Healing). Each point represents a TCR-β clone. For the left and middle columns, the y-axis represents the proportion of a given TCR-β clone in the patient's control tissue repertoire, and the x-axis represents the proportion of the TCR-β clone in their (left column) tumour TCR-β repertoire or (middle column) irMyocarditis TCR-β repertoire. Right column: proportion of TCR-β clone in the tumour is shown on the y-axis and the proportion of that clone in irMyocarditis is shown on the x-axis. Points are pseudocoloured to represent a TCR-β clone that was expanded (> 0.5% of the heart or tumour repertoire) and enriched (Fisher's exact test FDR < 5% compared to control) in heart (green), tumour (purple), both tissues (red), or neither tissue (grey). **g**, Each TCR-β clone enriched in heart or tumour relative to controls (FDR < 0.05, Fisher's exact test) is plotted according to its proportion (among all TCR-β clones in the respective tissue) in heart (x-axis) and tumour tissue (y-axis), normalized by its proportion in control tissue. Each plot shows the enriched TCR-β clones within each donor projected onto the aggregate data across all donors (Fig. 3b, c). **h**, TCR-β CDR3 amino acid sequences for select GLIPH groups. Highlighted in red are the predicted enriched motifs. **i**, The same data as shown in **g**, with colour indicating if the corresponding TCR-β was (red; "true") or was not (grey; "false") found in a GLIPH group. **j**, The frequency of each expanded GLIPH group in heart and tumour tissue was calculated and then normalized by dividing by the frequency of that same GLIPH group in control tissue. Normalized GLIPH group frequencies for heart (x-axis) and tumour (y-axis) are plotted. Colour indicates the donor from which each GLIPH group was found, and the label shows the associated amino acid motif of the GLIPH group. Throughout the Figure, red patient labels denote cases of fatal irMyocarditis. **Related to** Fig. 3.

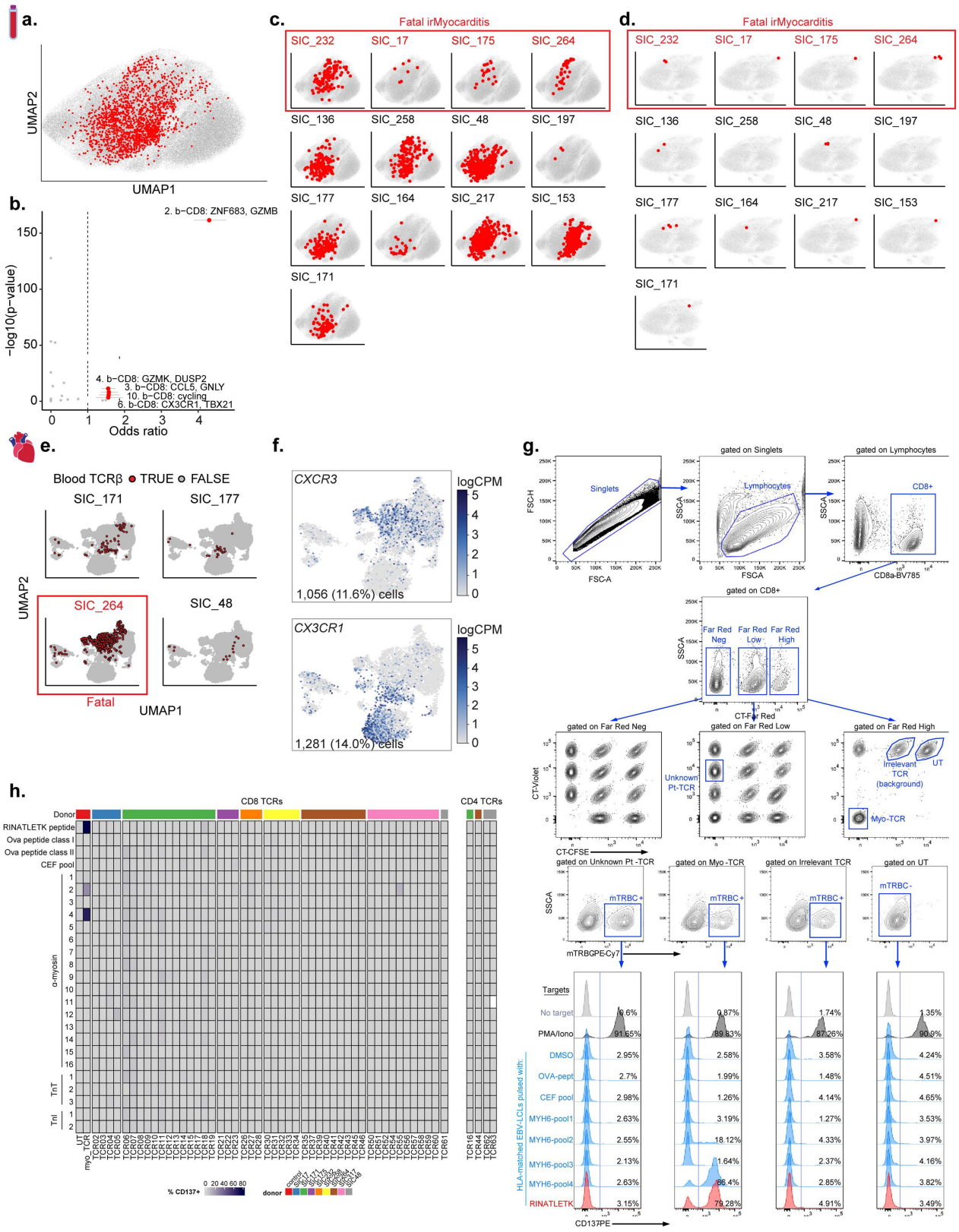

Extended Data Fig. 6 | See next page for caption.

Extended Data Fig. 6 | TCR clonotype sharing and antigen recognition screen. a, Blood CD8T/NK UMAP highlighting circulating cells (in red) that express a TCR-β sequence found to be expanded in irMyocarditis hearts (combined scRNA-seq and bulk TCR-β sequencing data). **b**, A volcano plot showing the results of a logistic regression model investigating the likelihood of a cell in a given CD8T/NK cell subset from the blood containing a TCR-β CDR3 sequence that was expanded in heart tissue (n = 13). Points represent odds ratios for each cell subset. Red points denote cell subsets with statistically significant sharing (FDR < 0.05, two-sided likelihood-ratio test). Error bars represent 95% confidence intervals. **c**,**d**, Cells in blood for which the same TCR-β was expanded in paired irMyocarditis heart and blood sample from the same patient are shown in red projected on the (**c**) CD8T/NK blood UMAP embedding and (**d**) CD4T blood UMAP embedding. Each patient with paired heart and blood samples is shown. **e**, UMAP of heart T and NK cells highlighting cells that express expanded TCR-β CDR3 sequences that were found in CD8T/NK blood cells on a per-patient basis. **f**, Feature plots using colour to indicate gene expression (logCPM) levels of the indicated genes projected onto the heart T/NK UMAP embedding. Cell numbers and percentages represent gene expression across all heart T and NK cells. **g**, The flow cytometry gating strategy for the CD137 expression assay is shown. Lymphocytes are analyzed as either $CD8^+$ or $CD8^-$ (to assess for TCRs isolated from CD8 or CD4T cells, respectively) and then gated on intensity of Far Red, CT-Violet, or CT-CFSE staining; each combination of stains represents a unique TCR. Each TCR is then gated on $mTRBC^+$ to identify cells expressing the transduced TCR construct. Each row of histograms represents a condition of Epstein-Barr virus-immortalized lymphoblastoid cell lines (EBV-LCLs), which served as antigen presenting cells, pulsed with target peptides/peptide pools, and CD137 expression is shown. PMA/Iono serves as a positive control; "DMSO," "Ova peptide," and "CEF" represents negative controls; RINATLETK is an α-myosin peptide known to be recognized by the positive control TCR ("Myo-TCR")[16]; α-myosin pool 4 contains a 20-aa peptide with the RINATLETK sequence; and all other pools are considered test peptide pools. Irrelevant TCRs are TCRs from an unrelated donor[76] and serve as negative controls along with untransduced (UT) T cells. **h**, A heatmap showing the background subtracted CD137 expression of each TCR and peptide/peptide pool combination. Each column represents a unique TCR, colour coded by patient and then grouped by CD8 and CD4 TCRs. Each row represents peptides or peptide pools tested; these include the controls and pools covering the full length of the α-myosin, troponin I (TnI), and troponin T (TnT) proteins. α-myosin pool 11 could not be evaluated for TCR63 and is shown as empty space on the heatmap. In **c**, **d**, and **e**, red patient labels denote cases of fatal irMyocarditis. Abbreviations: CEF, Cytomegalovirus, Epstein-Barr virus, and influenza virus; EVB-LCLs, Epstein-Barr virus-immortalized lymphoblastoid cell lines; HLA, human leukocyte antigens; PMA/Iono, Phorbol 12-myristate 13-acetate/ionomycin; mTRBC, murine T-cell receptor β chain; TCR, T-cell receptor; TnI, troponin I; TnT, troponin T; UT, untransduced. **Related to** Fig. 3.

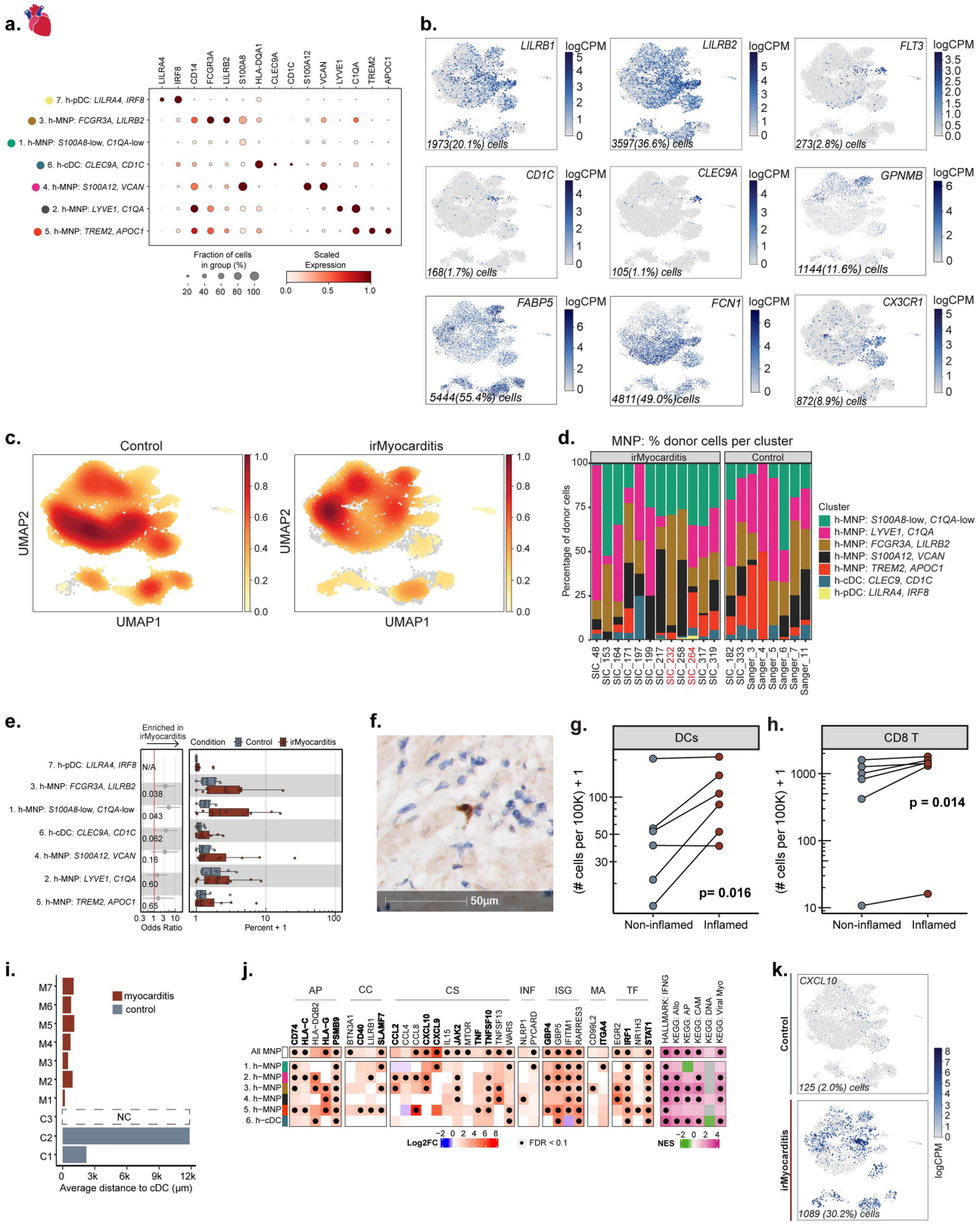

Extended Data Fig. 7 | See next page for caption.

Extended Data Fig. 7 | MNP populations in heart and blood. a, Selected marker genes for each MNP subset. Dot size represents the percent of cells in the subset with non-zero expression of a given gene. Colour indicates scaled expression. **b**, Feature plots using colour to indicate gene expression (logCPM) levels of the indicated genes projected onto the heart MNP UMAP embedding. Cell numbers and percentages represent gene expression across all heart MNP cells. **c**, Embedding of cell density plot displaying the relative proportion of cells from irMyocarditis cases (n = 3,606) and controls (n = 6,218). **d**, Stacked bar chart depicting the relative contributions of cells in each MNP subset (coloured coded on the right) on a per donor basis from each pre-steroid irMyocarditis or unenriched control sample. **e**, Abundance analysis comparing intramyocardial frequencies of cell populations from pre-steroid irMyocarditis cases (n = 12, red) versus control (n = 8, blue). Left: dots represent logistic regression odds-ratios. Error bars represent 95% confidence intervals. Unadjusted two-sided likelihood-ratio test *P* values for each subset are shown. Statistics for h-pDC$^{LILRA4, IRF8}$ are not included due to extremely low recovery from this cell subset. Right: box plots display the median (line) and IQR, with whiskers no more than 1.5x IQR. Each dot represents one patient. **f**, Representative image following immunohistochemical staining of irMyocarditis heart tissue section (n = 6) for CD1c (brown) and hematoxylin nuclear counterstaining (blue). **g**, **h**, Comparison of (**g**) cDCs (CLEC9A/CD1c^{+}) and (**h**) CD8T cell density as measured by immunofluorescence staining in non-inflamed regions (left column) and inflamed regions (right column) of irMyocarditis heart sections (n = 6); one-sided t-test *P* values are shown. **i**, Bar graph showing average distance from each cDC to the nearest CD8 T cell (per section), with each row representing an individual case (red) or control (blue); the control slide labeled "NC" (no cells) had neither *CD8A*+ nor CLEC9A/CD1c+ cells detected. **j**, Heatmap showing select DEGs and GSEA pathways for irMyocarditis versus control heart tissue grouped by biological themes. The "All MNP" row depicts DEG results from pooling MNP subsets 1–5. Colour scale indicates log2FC between irMyocarditis cases and controls and NES for GSEA. Black dots indicate FDR < 0.1 (Wald test). Genes in bold were a part of the leading edges genes of the displayed GSEA pathways. **k**, UMAP Feature plots using colour to indicate gene expression (logCPM) levels of *CXCL10* expressed by control (top) or irMyocarditis samples (bottom). Cell numbers and percentages represent expression across control or irMyocarditis MNP cells. Abbreviations: Allo, allograft rejection; AP, antigen presentation; CAM, cell adhesion molecules; CC, co-inhibition or co-stimulation; CS, cytokine signalling; DNA, DNA synthesis; IFNG, interferon-γ signalling; INF, inflammasome; ISG, interferon-stimulated genes; KEGG, Kyoto Encyclopedia of Genes and Genomes; MA, motility and adhesion; NES, normalized enrichment score; TF, transcription factors; Viral Myo, viral myocarditis. **Related to** Fig. 4.

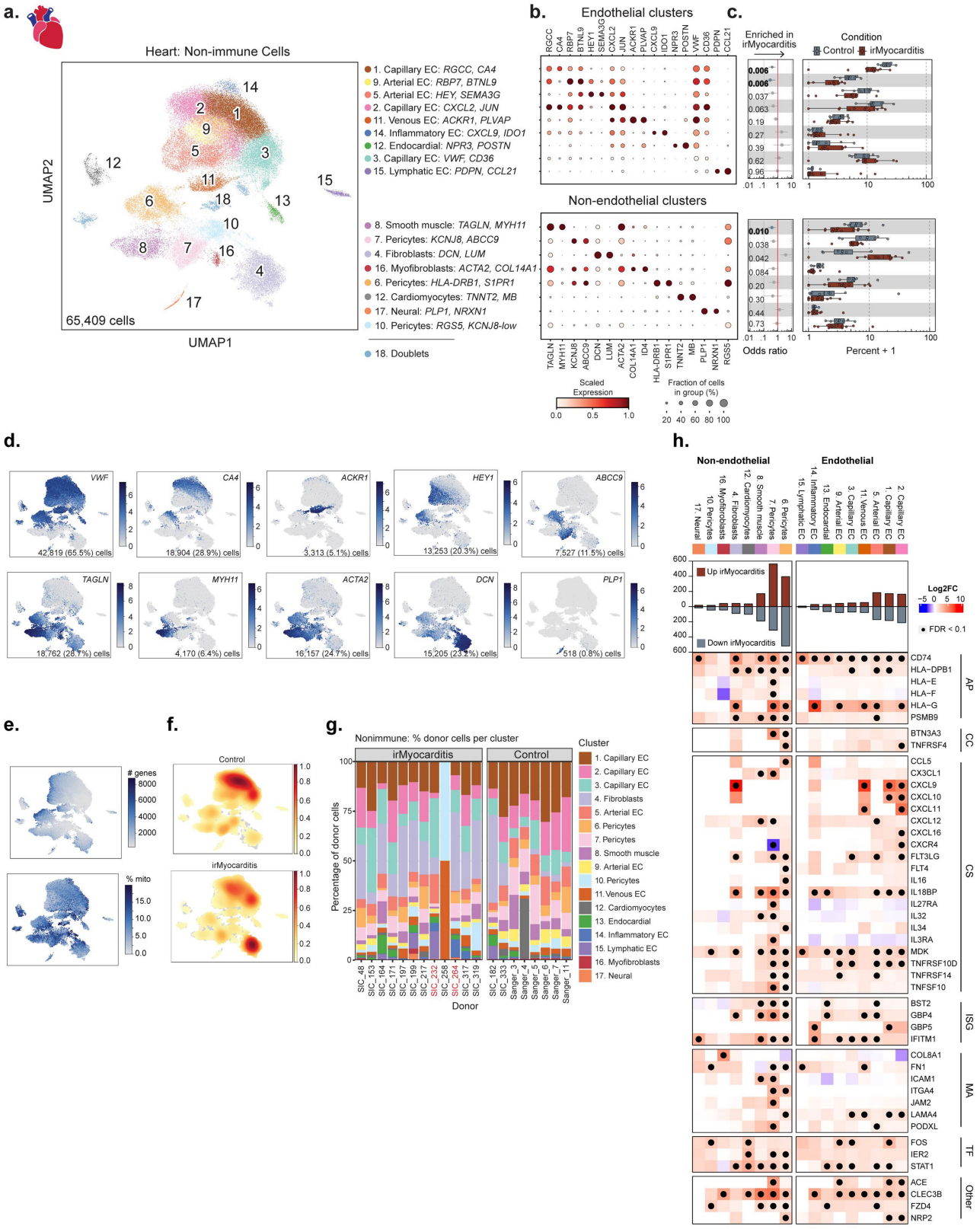

Extended Data Fig. 8 | See next page for caption.

Extended Data Fig. 8 | Non-immune populations in irMyocarditis heart tissue. a, UMAP embedding of 65,409 non-immune cells isolated from the heart, segregated by endothelial cells (top) and non-endothelial cells (bottom), and coloured by the 18 defined cell subsets labeled on the right. **b**, Dot plot showing top marker genes for each non-immune subset. Dot size represents the percent of cells in the subset with non-zero expression of a given gene. Colour indicates scaled expression across subsets. **c**, Abundance analysis comparing intramyocardial frequencies of cell populations from pre-steroid irMyocarditis heart samples (n = 12, red) versus controls (n = 8, blue). Left: dots represent logistic regression odds-ratios. Error bars represent 95% confidence intervals. Unadjusted two-sided likelihood-ratio test *P* values for each subset are shown. Colour and bolded *P* value indicates FDR < 0.1 Right: box plots display the median (line) and IQR, with whiskers no more than 1.5x IQR. Each dot represents one patient. **d**, Feature plots using colour to indicate marker gene expression (logCPM) levels of the indicated genes projected onto the heart non-immune UMAP embedding. Cell numbers and percentages represent gene expression across all heart non-immune cells. **e**, Feature plots showing (top panel) the number of genes expressed by each cell and (bottom panel) percent mitochondrial UMIs on the UMAP of non-immune cells derived from heart scRNA-seq data. **f**, Embedding of cell density plot displaying the relative proportion of cells from irMyocarditis cases (n = 20,439) and controls (n = 44,970). **g**, Stacked bar chart depicting the relative contributions of cells in each non-immune cell subset (colour coded to the right) from each pre-corticosteroid irMyocarditis or unenriched control sample. **h**, Top: the number of DEGs for each cell subset when comparing irMyocarditis cases (up, red) to control (down, blue). Bottom: heatmap showing select DEGs for irMyocarditis versus control heart tissue grouped by biological themes. Colour scale indicates log2FC difference between irMyocarditis cases and controls. Black dots indicate FDR < 0.1 (Wald test). Abbreviations: AP, antigen presentation; CC, co-inhibition or co-stimulation; CS, cytokine signalling; ISG, interferon-stimulated genes; MA, motility and adhesion; TF, transcription factors. **Related to** Fig. 5.

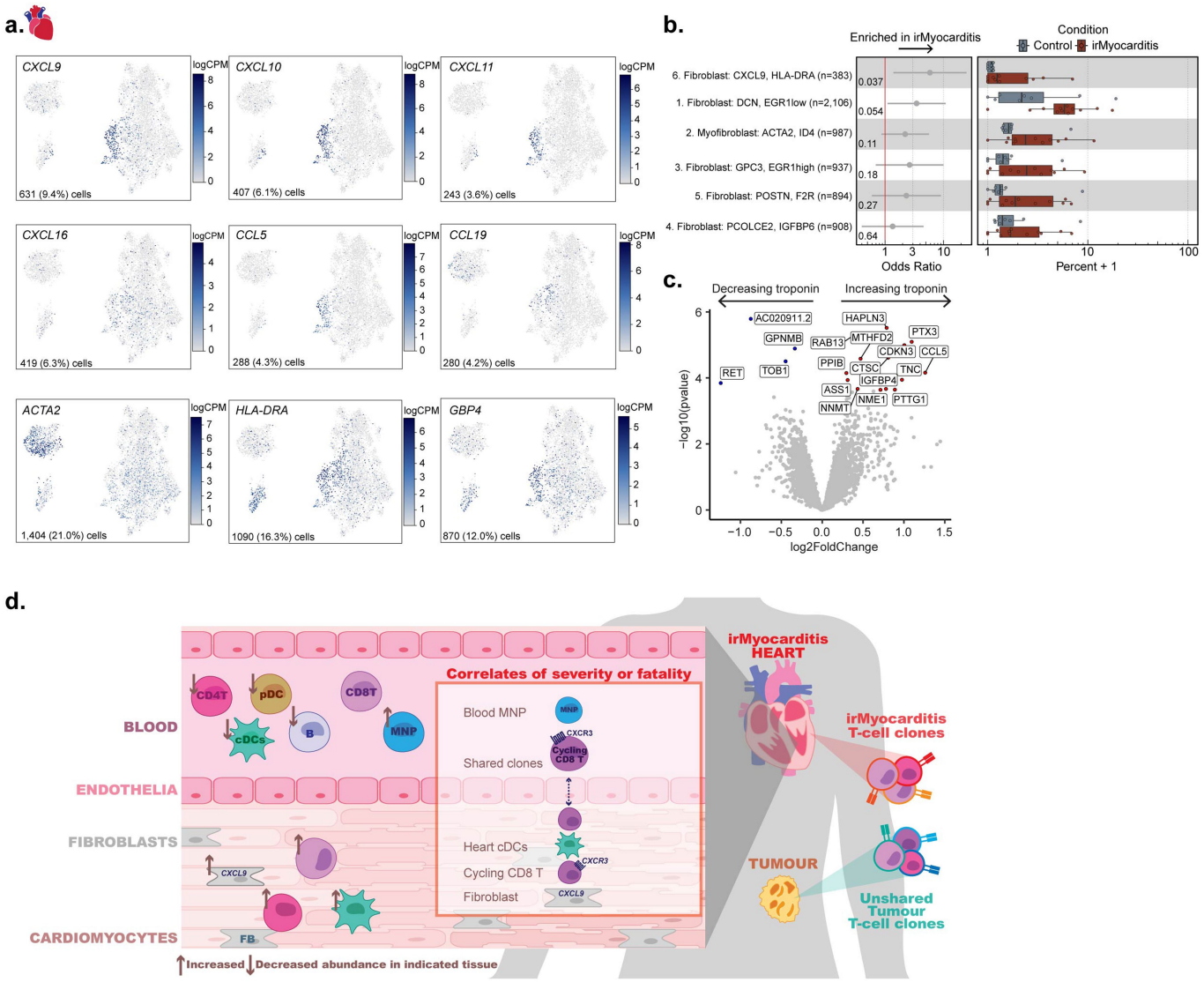

Extended Data Fig. 9 | Cardiac fibroblasts in irMyocarditis and graphical abstract summarizing key findings. a, Feature plots using colour to indicate marker gene expression (logCPM) levels of the indicated genes projected onto the heart fibroblast UMAP embedding. Cell numbers and percentages represent gene expression across all heart fibroblast and myofibroblast cells. **b**, Abundance analysis comparing intramyocardial frequencies of cell populations from pre-steroid irMyocarditis heart samples (n = 12, red) versus controls (n = 8, blue). Left: dots represent logistic regression odds-ratios. Error bars represent 95% confidence intervals. Unadjusted two-sided likelihood-ratio test *P* values for each subset are shown. Right: box plots display the median (line) and IQR, with whiskers no more than 1.5x IQR. Each dot represents one patient. **c**, Volcano plot of the genes within the fibroblast lineage modeled by serum troponin T, with select genes highlighted. Coloured points represent FDR < 0.1 (two-sided Wald test). **d**, Summary of key findings. Clusters whose abundances correlated with serum troponin T levels were considered correlates of disease severity. Abbreviations: FB, fibroblast. **Related to** Fig. 5.

a.

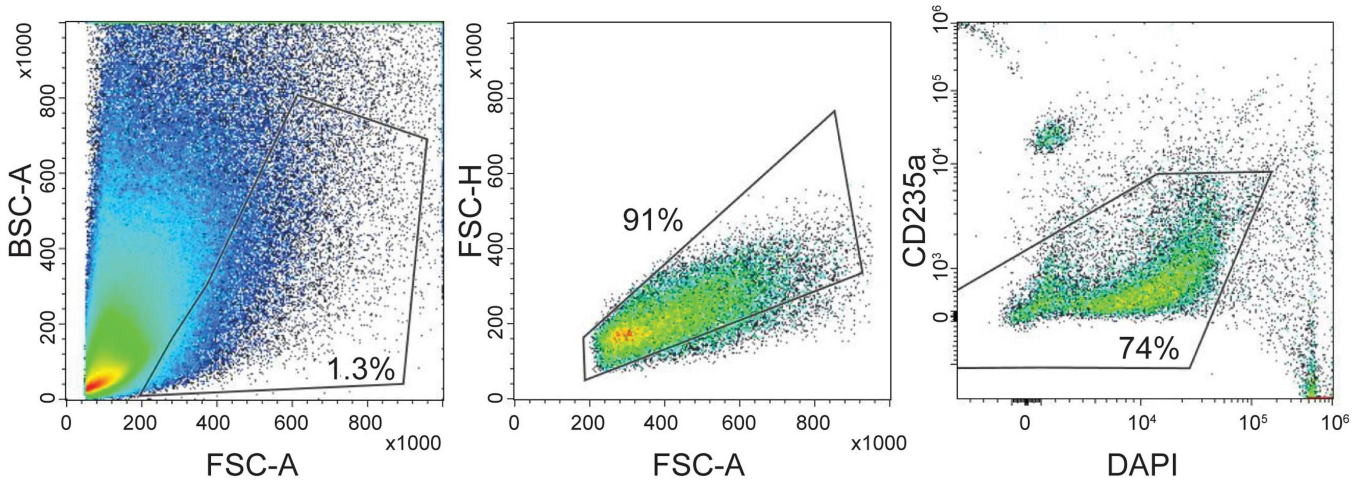

Extended Data Fig. 10 | Flow QC. a, Pseudocolour plots showing the applied sequential gating strategy to sort live cells for downstream scRNA-seq profiling from a representative myocardial sample. Numbers indicate the percentage within the indicated gate. DAPI$^-$CD235a$^-$ cells were collected for downstream analysis. Abbreviations: BSC-A, back scatter-area; FSC-A, forward scatter-area; FSC-H; forward scatter-height; DAPI, 4′,6-diamidino-2-phenylindole. **Related to all Figures; Methods**.

nature portfolio

Corresponding author(s): Alexandra-Chloe Villani

Last updated by author(s): Jun 11, 2024

Reporting Summary

Nature Portfolio wishes to improve the reproducibility of the work that we publish. This form provides structure for consistency and transparency in reporting. For further information on Nature Portfolio policies, see our Editorial Policies and the Editorial Policy Checklist.

Statistics

For all statistical analyses, confirm that the following items are present in the figure legend, table legend, main text, or Methods section.

n/a	Confirmed	
☐	☒	The exact sample size (*n*) for each experimental group/condition, given as a discrete number and unit of measurement
☐	☒	A statement on whether measurements were taken from distinct samples or whether the same sample was measured repeatedly
☐	☒	The statistical test(s) used AND whether they are one- or two-sided *Only common tests should be described solely by name; describe more complex techniques in the Methods section.*
☐	☒	A description of all covariates tested
☐	☒	A description of any assumptions or corrections, such as tests of normality and adjustment for multiple comparisons
☐	☒	A full description of the statistical parameters including central tendency (e.g. means) or other basic estimates (e.g. regression coefficient) AND variation (e.g. standard deviation) or associated estimates of uncertainty (e.g. confidence intervals)
☐	☒	For null hypothesis testing, the test statistic (e.g. *F*, *t*, *r*) with confidence intervals, effect sizes, degrees of freedom and *P* value noted *Give P values as exact values whenever suitable.*
☒	☐	For Bayesian analysis, information on the choice of priors and Markov chain Monte Carlo settings
☒	☐	For hierarchical and complex designs, identification of the appropriate level for tests and full reporting of outcomes
☐	☒	Estimates of effect sizes (e.g. Cohen's *d*, Pearson's *r*), indicating how they were calculated

Our web collection on statistics for biologists contains articles on many of the points above.

Software and code

Policy information about availability of computer code

Data collection	Microscopy images were collected using the HALO Image Analysis Platform (Indica Labs) and used the HALO FISH-IF (v2.2.5) and AI (v3.6.4134). Flow cytometric data was collected on a Sony MA900 Cell Sorter or a Fortessa flow cytometer (BD Biosciences).For base calling, we used Illumina software for the NextSeq and NovaSeq instrument.
Data analysis	Source code for data analysis is available on GitHub (https://github.com/villani-lab/myocarditis). A full list of software packages and versions included in the analyses is included in Supplementary Table 22 and listed below (package_name, loaded_version, language) adjustText 0.7.3 python aniso8601 9.0.1 python anndata 0.7.4 python annoy 1.17.0 python asciitree 0.3.3 python attrs 19.3.0 python backcall 0.1.0 python beautifulsoup4 4.11.1 python bleach 3.1.4 python boto3 1.7.84 python botocore 1.10.84 python cached-property 1.5.2 python cellbrowser 1.0.0 python

CellPhoneDB 2.1.7 python
certifi 2022.12.7 python
cffi 1.14.3 python
chardet 3.0.4 python
click 6.7 python
cmake 3.18.4.post1 python
colorama 0.4.3 python
cryptography 3.1 python
cycler 0.10.0 python
Cython 0.29.16 python
dataclasses 0.6 python
decorator 4.4.2 python
defusedxml 0.6.0 python
demuxEM 0.1.5 python
Distance 0.1.3 python
docopt 0.6.2 python
docutils 0.16 python
entrypoints 0.3 python
fasteners 0.15 python
fbpca 1 python
filelock 3.8.0 python
Flask 1.0.4 python
Flask-RESTful 0.3.9 python
Flask-Testing 0.7.1 python
forceatlas2-python 1 python
future 0.18.2 python
gdown 4.5.1 python
geosketch 0.3 python
get-version 2.1 python
gprofiler-official 1.0.0 python
h5py 2.10.0 python
harmony-pytorch 0.1.4 python
harmonypy 0.0.9 python
hdbscan 0.8.26 python
hnswlib 0.4.0 python
idna 2.1 python
imageio 2.9.0 python
importlib-metadata 5.1.0 python
iniconfig 1.1.1 python
intervaltree 2.1.0 python
ipykernel 5.2.0 python
ipython 7.13.0 python
ipython-genutils 0.2.0 python
ipywidgets 7.5.1 python
itsdangerous 2.0.1 python
jedi 0.16.0 python
jeepney 0.4.3 python
Jinja2 3.1.2 python
jmespath 0.10.0 python
joblib 0.17.0 python
json5 0.9.4 python
jsonschema 3.2.0 python
jupyter 1.0.0 python
jupyter-client 6.1.2 python
jupyter-console 6.1.0 python
jupyter-core 4.6.3 python
jupyterlab 2.0.1 python
jupyterlab-server 1.0.7 python
keyring 21.4.0 python
kiwisolver 1.3.1 python
legacy-api-wrap 1.2 python
leidenalg 0.8.3 python
lightgbm 3.1.0 python
llvmlite 0.34.0 python
logomaker 0.8 python
loompy 3.0.6 python
louvain 0.7.0 python
MarkupSafe 2.1.1 python
matplotlib 3.3.3 python
matplotlib-inline 0.1.6 python
matplotlib-venn 0.11.6 python
mistune 0.8.4 python
mkl-fft 1.3.0 python
mkl-random 1.1.1 python
mkl-service 2.3.0 python
monotonic 1.5 python

MulticoreTSNE-modified 0.1.post2 python
multipledispatch 0.6.0 python
natsort 7.0.1 python
nbconvert 5.6.1 python
nbformat 5.0.4 python
networkx 2.5 python
notebook 6.0.3 python
numba 0.51.2 python
numcodecs 0.7.2 python
numexpr 2.7.1 python
numpy 1.19.2 python
numpy-groupies 0.9.13 python
packaging 20.4 python
pandas 1.1.4 python
pandas-flavor 0.2.0 python
pandocfilters 1.4.2 python
parso 0.6.2 python
patsy 0.5.1 python
pegasus 0.1.3 python
pegasusio 0.2.7 python
pegasuspy 1.1.0 python
pexpect 4.8.0 python
pickleshare 0.7.5 python
pika 0.12.0 python
Pillow 8.0.1 python
pip 20.2.4 python
pkginfo 1.5.0.1 python
pluggy 0.13.1 python
prometheus-client 0.7.1 python
prompt-toolkit 3.0.5 python
ptyprocess 0.6.0 python
py 1.10.0 python
pyarrow 2.0.0 python
pybind11 2.6.1 python
pycparser 2.2 python
Pygments 2.6.1 python
pyjanitor 0.20.13 python
pynndescent 0.5.8 python
pyparsing 2.4.7 python
pyrsistent 0.16.0 python
PySocks 1.7.1 python
pytest 6.2.1 python
python-dateutil 2.8.1 python
python-igraph 0.8.3 python
pytz 2019.3 python
PyWavelets 1.1.1 python
PyYAML 5.1.2 python
pyzmq 19.0.0 python
qtconsole 4.7.2 python
QtPy 1.9.0 python
readme-renderer 26 python
requests 2.25.0 python
requests-toolbelt 0.9.1 python
rfc3986 1.4.0 python
rpy2 3.0.5 python
s3transfer 0.1.13 python
scanorama 1.7 python
scanpy 1.6.0 python
scikit-image 0.17.2 python
scikit-learn 0.22 python
scikit-misc 0.1.3 python
scipy 1.7.2 python
scrublet 0.2.1 python
seaborn 0.11.0 python
SecretStorage 3.1.2 python
semantic-version 2.8.5 python
Send2Trash 1.5.0 python
setuptools 50.3.0 python
setuptools-rust 0.12.1 python
setuptools-scm 5.0.1 python
simplegeneric 0.8.1 python
sinfo 0.3.1 python
six 1.15.0 python
sklearn 0 python
sortedcontainers 2.3.0 python
soupsieve 2.3.2.post1 python

SQLAlchemy 1.3.24 python
statsmodels 0.12.1 python
stdlib-list 0.8.0 python
tables 3.6.1 python
terminado 0.8.3 python
testpath 0.4.4 python
texttable 1.6.3 python
threadpoolctl 2.1.0 python
tifffile 2020.11.18 python
toml 0.10.2 python
torch 1.7.0 python
tornado 6.0.4 python
tqdm 4.32.2 python
traitlets 4.3.3 python
twine 3.2.0 python
typing-extensions 3.7.4.3 python
tzlocal 2.1 python
umap-learn 0.4.6 python
urllib3 1.26.2 python
wcwidth 0.1.9 python
webencodings 0.5.1 python
Werkzeug 2.0.1 python
wheel 0.35.1 python
widgetsnbextension 3.5.1 python
xarray 0.17.0 python
xlrd 1.2.0 python
XlsxWriter 1.3.7 python
zarr 2.5.0 python
zipp 3.1.0 python
ggrepel 0.9.2 R
ggpubr 0.5.0 R
reticulate 1.27 R
DESeq2 1.38.2 R
SummarizedExperiment 1.28.0 R
Biobase 2.58.0 R
MatrixGenerics 1.10.0 R
matrixStats 0.63.0 R
GenomicRanges 1.50.2 R
GenomeInfoDb 1.34.7 R
IRanges 2.32.0 R
S4Vectors 0.36.1 R
BiocGenerics 0.44.0 R
magrittr 2.0.3 R
alakazam 1.0.2 R
scattermore 0.8 R
knitr 1.41 R
ggstance 0.3.6 R
lme4 1.1-31 R
patchwork 1.1.2 R
ggbeeswarm 0.7.1 R
ggforestplot 0.1.0 R
glue 1.6.2 R
Matrix 1.5-1 R
circlize 0.4.15 R
ComplexHeatmap 2.14.0 R
RColorBrewer 1.1-3 R
parameters 0.20.2 R
rlang 1.0.6 R
rmarkdown 2.19 R
forcats 0.5.2 R
stringr 1.5.0 R
dplyr 1.0.10 R
purrr 1.0.1 R
readr 2.1.3 R
tidyr 1.2.1 R
tibble 3.1.8 R
ggplot2 3.4.0 R
tidyverse 1.3.2 R
readxl 1.4.1 R
backports 1.4.1 R
igraph 1.3.5 R
lazyeval 0.2.2 R
splines 4.2.2 R
BiocParallel 1.32.5 R
digest 0.6.31 R
foreach 1.5.2 R

htmltools 0.5.4 R
fansi 1.0.3 R
memoise 2.0.1 R
googlesheets4 1.0.1 R
cluster 2.1.4 R
doParallel 1.0.17 R
tzdb 0.3.0 R
Biostrings 2.66.0 R
annotate 1.76.0 R
modelr 0.1.10 R
timechange 0.1.1 R
prettyunits 1.1.1 R
colorspace 2.0-3 R
blob 1.2.3 R
rvest 1.0.3 R
haven 2.5.1 R
xfun 0.36 R
crayon 1.5.2 R
RCurl 1.98-1.9 R
jsonlite 1.8.4 R
survival 3.5-3 R
iterators 1.0.14 R
ape 5.6-2 R
gtable 0.3.1 R
gargle 1.2.1 R
zlibbioc 1.44.0 R
XVector 0.38.0 R
seqinr 4.2-23 R
GetoptLong 1.0.5 R
DelayedArray 0.24.0 R
car 3.1-1 R
shape 1.4.6 R
abind 1.4-5 R
scales 1.2.1 R
DBI 1.1.3 R
rstatix 0.7.1 R
Rcpp 1.0.8 R
xtable 1.8-4 R
progress 1.2.2 R
clue 0.3-63 R
bit 4.0.5 R
datawizard 0.6.5 R
httr 1.4.4 R
ellipsis 0.3.2 R
pkgconfig 2.0.3 R
XML 3.99-0.13 R
dbplyr 2.2.1 R
locfit 1.5-9.7 R
utf8 1.2.2 R
tidyselect 1.2.0 R
AnnotationDbi 1.60.0 R
munsell 0.5.0 R
cellranger 1.1.0 R
tools 4.2.2 R
cachem 1.0.6 R
cli 3.5.0 R
generics 0.1.3 R
RSQLite 2.2.20 R
ade4 1.7-20 R
broom 1.0.2 R
evaluate 0.19 R
fastmap 1.1.0 R
bit64 4.0.5 R
fs 1.5.2 R
KEGGREST 1.38.0 R
nlme 3.1-162 R
xml2 1.3.3 R
compiler 4.2.2 R
beeswarm 0.4.0 R
png 0.1-8 R
ggsignif 0.6.4 R
reprex 2.0.2 R
geneplotter 1.76.0 R
stringi 1.7.8 R
lattice 0.20-45 R
nloptr 2.0.3 R

vctrs 0.5.1 R
pillar 1.8.1 R
lifecycle 1.0.3 R
GlobalOptions 0.1.2 R
bitops 1.0-7 R
insight 0.19.0 R
R6 2.5.1 R
vipor 0.4.5 R
codetools 0.2-19 R
boot 1.3-28 R
MASS 7.3-58.2 R
assertthat 0.2.1 R
rjson 0.2.21 R
withr 2.5.0 R
GenomeInfoDbData 1.2.9 R
bayestestR 0.13.0 R
parallel 4.2.2 R
hms 1.1.2 R
minqa 1.2.5 R
carData 3.0-5 R
googledrive 2.0.0 R
lubridate 1.9.0 R
limma 3.54.0 R

For manuscripts utilizing custom algorithms or software that are central to the research but not yet described in published literature, software must be made available to editors and reviewers. We strongly encourage code deposition in a community repository (e.g. GitHub). See the Nature Portfolio guidelines for submitting code & software for further information.

Data

Policy information about availability of data

All manuscripts must include a data availability statement. This statement should provide the following information, where applicable:

- Accession codes, unique identifiers, or web links for publicly available datasets
- A description of any restrictions on data availability
- For clinical datasets or third party data, please ensure that the statement adheres to our policy

scRNA-seq count matrices and related data as well as TCR sequencing data is deposited in the GEO database (under accession #GSE228597), and raw human sequencing data is available in the controlled access repository dbGaP (https://www.ncbi.nlm.nih.gov/gap/; accession phs003413.v1.p1).

Research involving human participants, their data, or biological material

Policy information about studies with human participants or human data. See also policy information about sex, gender (identity/presentation), and sexual orientation and race, ethnicity and racism.

Reporting on sex and gender	Sex and gender were not considered as part of study design, as biological specimens from eligible study participants who provided informed consent were obtained and utilized regardless of their gender and/or sex. The biological sex of included participants was recorded as is presented in Figure 1a and Supplementary Tables 1; participant genders were not recorded. Informed consent was obtained for individual-level data. Sex was considered as a covariate in blood-based analyses.
Reporting on race, ethnicity, or other socially relevant groupings	Race, ethnicity, and other socially relevant groupings were not reported in our manuscript.
Population characteristics	Age, sex, cancer type, cancer therapy, and other patient characteristics were recorded and are presented in Supplemental Tables 1.
Recruitment	Participants with cancer deemed to meet study inclusion and exclusion criteria were approached by authorized staff and asked if they would like to participate in a research study. No patient-facing materials were used to aid recruitment, thereby reducing the possibility of self-selection bias.
Ethics oversight	The study protocols were approved by Dana-Farber/Harvard Cancer Center Institutional Review Boards (protocols 11-181 and 13-416).

Note that full information on the approval of the study protocol must also be provided in the manuscript.

Field-specific reporting

Please select the one below that is the best fit for your research. If you are not sure, read the appropriate sections before making your selection.

☒ Life sciences ☐ Behavioural & social sciences ☐ Ecological, evolutionary & environmental sciences

For a reference copy of the document with all sections, see nature.com/documents/nr-reporting-summary-flat.pdf

Life sciences study design

All studies must disclose on these points even when the disclosure is negative.

Sample size	No sample size calculation was performed. Rather, sample sizes were determined based on all available biological samples collected during our recruitment period spanning October 2017 through July 2022. To look for additional control blood samples, we reviewed >300 patient charts to identify those that met our criteria for controls but did not have a prospective sample size.
Data exclusions	There were no data exclusions.
Replication	Due to the limited quantity of our human samples, and in particular human heart biopsy samples, none of the experiments were able to be replicated. However, we used orthogonal experimental approaches to validate our findings.
Randomization	Patients were not randomized. Patients were determined to have irMyocarditis based on either histological or characteristic magnetic resonance imaging (MRI) findings that were used to clinically confirm a diagnosis of irMyocardits. Different comparator groups are utilized throughout the study, and were either ICI-treated patients without evidence of irMyocarditis (heart and blood data) or patients who were not treated with ICIs (published heart data only).
Blinding	The status of irMyocarditis cases vs controls was blinded at the time of collection for most of the heart samples, as samples were processed immediately, and a diagnosis by a clinical pathologist would not occur until after the data was generated.

Reporting for specific materials, systems and methods

We require information from authors about some types of materials, experimental systems and methods used in many studies. Here, indicate whether each material, system or method listed is relevant to your study. If you are not sure if a list item applies to your research, read the appropriate section before selecting a response.

Materials & experimental systems

n/a	Involved in the study
☐	☒ Antibodies
☒	☐ Eukaryotic cell lines
☒	☐ Palaeontology and archaeology
☒	☐ Animals and other organisms
☒	☐ Clinical data
☒	☐ Dual use research of concern
☒	☐ Plants

Methods

n/a	Involved in the study
☒	☐ ChIP-seq
☐	☒ Flow cytometry
☒	☐ MRI-based neuroimaging

Antibodies

Antibodies used	Antibody used for cell sorting by flow cytometry: anti-CD235a-PE-Cy5 (Biolegend 306606), CD137-PE (Biolegend, 309804), CD8-BV785 (Biolegend, 301046), mTCRB-PE-Cy7, (eBioscience, 25-5961-82) Antibody used for immunofluorescence anti-CD1c-OTI2F4 mAb (Abcam ab156708). CLEC9A-EPR22324] (Abcam ab223188)
Validation	Flow cytometry antibodies were validated by the manufactuer. Antibodies used for microscopy were tested on tonsil as positive control tissue.

Plants

Seed stocks	*Report on the source of all seed stocks or other plant material used. If applicable, state the seed stock centre and catalogue number. If plant specimens were collected from the field, describe the collection location, date and sampling procedures.*
Novel plant genotypes	*Describe the methods by which all novel plant genotypes were produced. This includes those generated by transgenic approaches, gene editing, chemical/radiation-based mutagenesis and hybridization. For transgenic lines, describe the transformation method, the number of independent lines analyzed and the generation upon which experiments were performed. For gene-edited lines, describe the editor used, the endogenous sequence targeted for editing, the targeting guide RNA sequence (if applicable) and how the editor was applied.*
Authentication	*Describe any authentication procedures for each seed stock used or novel genotype generated. Describe any experiments used to assess the effect of a mutation and, where applicable, how potential secondary effects (e.g. second site T-DNA insertions, mosiacism, off-target gene editing) were examined.*

Flow Cytometry

Plots

Confirm that:

☒ The axis labels state the marker and fluorochrome used (e.g. CD4-FITC).

☒ The axis scales are clearly visible. Include numbers along axes only for bottom left plot of group (a 'group' is an analysis of identical markers).

☒ All plots are contour plots with outliers or pseudocolor plots.

☒ A numerical value for number of cells or percentage (with statistics) is provided.

Methodology

Sample preparation	For scRNA-seq Tissue samples obtained by biopsy or autopsy were immediately placed in ice-cold HypoThermosol solution (BioLife Solutions, Bothell, WA) and kept on ice during transfer to the research facility. Tissue was then washed twice with cold phosphate buffered saline. Tissue was then dissociated using the human tumor dissociation kit according to the manufacturer's instructions (Miltenyi Biotic, Bergisch Gladbach, Germany) with modification such that calcium chloride was added to the enzymatic cocktail to a final concentration of 1.25 mM. Tubes containing tissue fragments in the enzymatic cocktail were placed in a heated shaker at 37° C with shaking at 750 RPM for 25 minutes with the machine placed on its side to prevent tissue fragments from settling. Following incubation, the reaction was quenched through the addition of 100 µl human serum. The mixture was further dissociated through manual trituration followed by filtration through 70 µm mesh. Following centrifugation at 350 x g for 12 minutes, the supernatant was removed and RBC lysis was performed (ACK lysing buffer, Lonza, Basel, Switzerland). Following a wash step, cells were resuspended in phenol-free RPMI with 2% (v/v) human AB serum. Fc receptors were blocked (Human TruStain FcX, Biolegend 422302), after which cells were incubated with CD235a-PE-Cy5 (Biolegend 306606) for 30 minutes. Following a wash, cells were resuspended in sort buffer containing DAPI. For Antigen Screening Assays After an overnight incubation, TCR reactivity was measured trough detection of CD137 surface expression (PE, clone 4B4-1, Biolegend, catalog # 309804, dilution 1:50) on CD8+ (BV785, clone RPA-T8, Biolegend, catalog # 301046, dilution 1:100) or CD8- (CD4+) TCR- transduced (mTCRB+, PE-Cy7, clone H57-597, eBioscience, catalog # 25-5961-82, dilution 1:50) T cells using a Fortessa flow cytometer (BD Biosciences). Data were analyzed using Flowjo software (v10.8.2, BD Biosciences). For CD8 TCRs, CD137 upregulation was evaluated from the CD8+ gate (Extended Data Figure 6a), and for CD4 TCRs, CD137 upregulation was evaluated from a CD8- gate. Background CD137 reactivity, measured in the presence of target cells pulsed with DMSO, was subtracted.
Instrument	Sony MA900 Cell Sorter; Fortessa flow cytometer (BD Biosciences).
Software	Cell Sorter Software version 3.3.0; Flowjo software v10.8.2 (BD Biosciences)
Cell population abundance	The abundance and purity of the sorted cells were not assessed as sorting was used only as a means to isolate live cells.
Gating strategy	A side scatter (called back-scatter on Sony instrument) x forward scatter gate was first used to include all cells and exclude debris and aggregates of larger and smaller sizes. A singlet gate was then applied using FSC-A x FSC-H. Finally, a gate on DAPI-negative, CD235a-negative cells was applied. Live cells depleted for red blood cells within this fraction were collected and processed for downstream single-cell RNA sequencing.

☒ Tick this box to confirm that a figure exemplifying the gating strategy is provided in the Supplementary Information.